

Master's Thesis

Mass Sensitivity of the QCD Phase Structure

-

Massenabhängigkeit des QCD Phasendiagramms

von

Simon Resch

1. August 2016

Betreuer:

PD Dr. Bernd-Jochen Schaefer

Contents

1	Introduction	1
1.1	Notations and Conventions	4
2	Functional Methods	7
2.1	The Generating Functional	7
2.2	The Effective Action	8
2.3	The Effective Potential	9
3	Quantum Chromodynamics	11
3.1	QCD as a Non-Abelian Gauge Theory	12
3.2	Symmetries of QCD	14
3.3	Spontaneous Breaking of Chiral Symmetry	16
3.4	Anomalous Breaking of $U(1)_A$	17
4	The Functional Renormalization Group	19
4.1	The Wetterich Equation	19
5	The Chiral Phase Transition of QCD	27
5.1	Effective Action for Low Energy QCD	27
5.2	Deriving the Flow Equation	32
5.3	Flow Equation for 2+1 Flavor	36
5.4	Flow Equation for the $SU(2)_L \otimes SU(2)_R$ Model	38
6	Numerical Results	41
6.1	Finite Temperature	41
6.2	The Scalar-Pseudoscalar Meson Spectrum	43
6.3	Pressure Density	44
6.4	Finite μ and the Phase Diagram	46
6.5	The Light Chiral Limit	49
6.6	The Chiral Critical Line	50
7	Numerical Implementation	57
7.1	Two Dimensional Grid	57
7.2	Bilocal Expansion	59
8	Summary and Outlook	63
A	Effective Potential in Mean Field Approximation	67
B	Meson Mass Matrix	69
B.1	Meson Masses in FRG	69

B.2 Meson Masses in Mean Field Approximation	71
C Parameter Fixing	73
D Determining the Chiral Critical Line	75
Bibliography	79

Short range particle interactions are mainly governed by three fundamental forces: the electromagnetic, weak and strong force. Their unified description as quantum field theories based on gauge invariance makes up the Standard Model of particle physics. It successfully explains a wide range of experimental results and allows for astoundingly accurate predictions of various phenomena.

In this thesis we will focus solely on the strong force which is described by the quantum field theory named *quantum chromodynamics* (QCD). Its building blocks are the fermionic *quark* fields and their interaction is governed by *gluon* fields—the gauge bosons of QCD. Most notably, the proposition of quarks has provided a classification scheme for the multitude of particles discovered in the 1950s and goes back to the quark model by Gell-Mann and Zweig from 1964 [1, 2]. It entails that quarks form bound states called *hadrons*. This model was first challenged with the discovery of the Δ^{++} baryon which consists of three quarks with parallel spin. This seemed to violate the Pauli principle and for this reason a new quantum number was proposed—the so called *color charge*. At that time *quantum electrodynamics* (QED), the gauge theory describing electromagnetic interactions, was already enjoying great success and so QCD was also constructed upon the principle of gauge invariance with the underlying gauge group $SU(N_c)$, where N_c is the number of color charges and $N_c = 3$ is realized in nature.

One of the curious properties of QCD is the fact that no states have been detected so far that carry color charge. This phenomenon is known as *confinement* and implies that no free quarks may be directly measured. Another defining feature of QCD is *asymptotic freedom*, discovered by Gross, Wilczek and Politzer in 1973 [3, 4]. Quarks and gluons are asymptotically free in a sense that the strong interaction becomes weak at high energies. It is therefore believed that quarks and gluons form a so called *quark-gluon plasma* at high temperatures and densities [5] for example present in the early universe. An interesting question is then how this fundamentally different state of QCD is connected to low energy QCD where quarks are bound to hadrons. It is natural to assume that a phase transition between both states of QCD occurs at certain temperatures and densities. In fact, various model studies suggest that QCD exhibits a rich phase structure with the possibility for a critical end point (CEP) [6]. An idealized picture of the current knowledge about the QCD phase diagram is shown in Fig. 1.1.

Theoretical investigations of QCD basically predict two distinct transitions at high temperature and densities: Deconfinement of quark matter and restoration of chiral symmetry. Both transitions seem to be connected, however, the exact nature of their interplay is still under discussion. In this thesis we will focus exclusively on the chiral phase transition. Various other phases of QCD, for example a color superconducting phase at very high densities, have been conjectured [8, 9].

On the technical side QCD has proven to be an exceptionally hard theory to solve. This is in part due to the running of the strong coupling. Standard perturbative approaches give access to the high energy limit of QCD, however, for small energies the strong coupling grows and therefore an expansion in this parameter is bound to break down. Low energy theoretical studies of QCD rely on model calculations and non-perturbative methods. One such method that has gained a lot of traction in recent years is lattice gauge theory. On a discrete set of

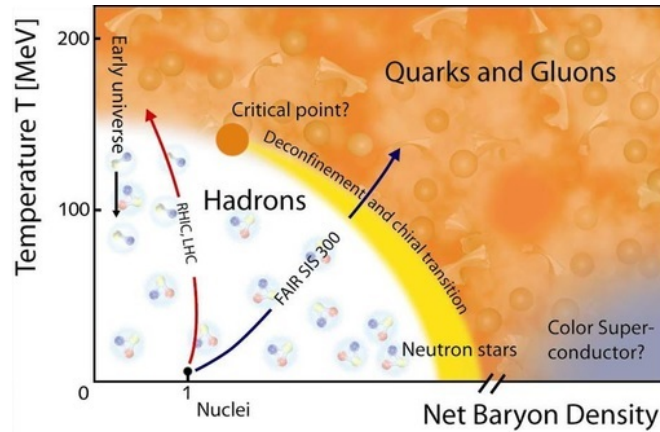


Figure 1.1: Schematic overview of the QCD phase diagram [7].

space-time points, called the lattice, the QCD path integral is calculated directly using Monte Carlo methods. This has given first reliable results for various aspects of QCD such as the critical temperature and the crossover nature of the chiral transition at vanishing chemical potential [10–12]. However, the famous sign problem of lattice gauge theory hinders its application to finite chemical potential. Different methods to circumvent this problem are currently under active research [13, 14]. Furthermore, the inclusion of fermions on the lattice is computationally expensive and this is especially true for the chiral limit which can only be reached by extrapolation to vanishing quark masses.

Other non-perturbative methods that have been successfully applied to QCD include *Dyson-Schwinger equations* (DSE) and the *functional renormalization group* (FRG). Both are based on the path integral formulation of quantum field theory and they are both intrinsically exact functional equations. However, for any non trivial system truncations have to be made which spoil this exactness. Crucially, within these methods, one can develop truncation schemes which do not expand in the coupling strength and therefore can be applied to low energy QCD. Furthermore, finite chemical potential can be implemented without encountering the sign problem.

In this thesis we use the FRG framework to investigate the chiral phase transition of 2+1 flavor QCD. It is known that the correlation length ζ diverges at the critical point and consequently fluctuations on all length scales become relevant. Within the FRG formulation this is handled by implementing Wilson’s *renormalization group* idea of successively integrating fluctuations on an infinitesimal momentum shell. This makes the FRG a suitable tool for the study of critical phenomena, see e.g. [15]. In this thesis we will show how the $U(N_f)_L \otimes U(N_f)_R$ quark-meson model follows from a low energy treatment of QCD and then focus on a 2+1 flavor formulation thereof. This procedure is systematically improvable and can be related to perturbative QCD by a technique called dynamical hadronization [16–18].

The 2 flavor phase diagram has already been extensively studied within the FRG framework, see e.g. [19, 20]. Restoration of chiral symmetry is commonly studied within effective quark-meson type models. These models are then often augmented by the *Polyakov loop* which incorporates gluon degrees of freedom in form of an effective gluon potential [21, 22]. This makes it possible to investigate the deconfinement transition of QCD in a rudimentary fashion. Only recently have these considerations been extended to 2+1 flavor [23–26].

Various investigations have found that the nature of the chiral phase transition is heavily dependent on the quark masses. General renormalization group arguments predict a first-order phase transition of 3 flavor QCD in the chiral limit [27]. It is still not entirely settled how this statement relates to the physical point¹ where lattice results reliably determine the chiral

¹Where quarks have a finite current mass.

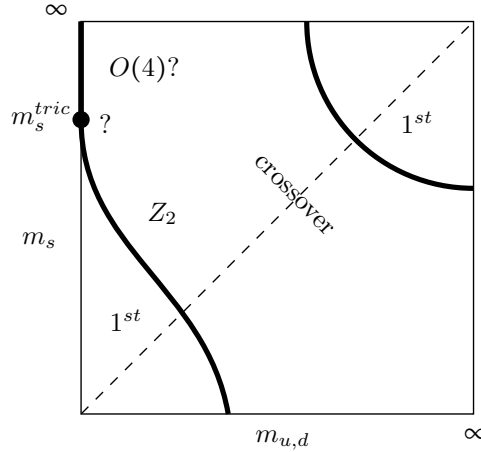


Figure 1.2: Sketch of the order of the chiral phase transition in dependence of quark masses at zero chemical potential [13].

phase transition to be a smooth crossover [10–12]. The order of the chiral phase transition in dependence of quark masses is visualized in the so called *Columbia plot*. An idealized picture of the current knowledge of the Columbia plot at vanishing chemical potential is shown in Fig. 1.2. A second-order line (*chiral critical line*) separates the first-order region around the chiral limit and the crossover region comprising the physical point. This second-order line has been determined by lattice calculations to fall under the Ising (Z_2) universality class [28, 29]. Lattice calculations have to this date not been conclusive in the *light chiral limit* where the two lightest quarks (up and down) are massless [30, 31]. One possibility is the existence of a tricritical point where the Ising (Z_2) second-order line hits the m_s axis. About this tricritical point a second-order line is expected to follow along the m_s axis into the 2 flavor limit at $m_s = \infty$. In this scenario the universality class of the second-order line along the m_s axis is likely to be dictated by 2 flavor QCD. One possibility is the universality class $O(4)$ as seen in $SU(2)_L \otimes SU(2)_R$ models.

An entirely different picture is seen for example in a mean field investigation [32]. There a wide first-order region has been found that connects the chiral limit to the 2 flavor axis. On the other hand, a similar investigation in Hartree approximation predicts a small first-order region around the chiral limit with a tricritical point at the m_s axis [33]. Fluctuations are expected to further modify the structure of the critical line and this will be the main topic of this work. We include meson and quark fluctuations within the FRG framework and determine the dependence of the chiral phase transition on pion and kaon masses.

The mass sensitivity of the chiral phase transition is also highly relevant for the search of a CEP in the QCD phase diagram. This becomes evident by extending the Columbia plot into the μ axis. The chiral critical line then turns into a critical surface and its curvature ultimately determines if a CEP exists for physical quark masses. The standard scenario involves a positive curvature of the critical surface at $\mu = 0$ so that the first-order region expands for increasing μ which would place the physical point in the first-order region at some finite μ . The contrary scenario suggests a negative curvature and would lead to a vanishing first-order region at some μ . Recent lattice simulations using the imaginary chemical potential method favor the non-existence of a tricritical point on the m_s axis and predict a shrinking first-order region at finite μ [13, 34].

Another aspect of QCD that plays a crucial role in the chiral phase transition of QCD is the anomalous breaking of $U(1)_A$ symmetry. It is the reason why the η' meson is not a light pseudo Goldstone boson [35, 36]. As shown by 't Hooft the anomaly is caused by instantons and it can be effectively understood as a $2N_f$ quark interaction mixing quarks of different flavor [37]. The resulting determinant in flavor space breaks $U(1)_A$ symmetry and can be formulated in terms

of meson fields via a bosonization procedure [38, 39]. Previous investigations have shown that the order of the chiral phase transition is crucially dependent on the state of the anomaly at the critical temperature [32, 33].

This thesis is structured as follows: We start by collecting some basic facts about the functional approach to quantum field theory. Then we briefly discuss properties of QCD and focus on its symmetries as they will play an integral role for the construction of our truncation. After the basic ideas of the functional renormalization group are introduced in Sec. 4, the truncation is motivated which we use to study the chiral phase transition of QCD. We then derive the Wetterich flow for the $U(N_f)_L \otimes U(N_f)_R$ truncation and discuss the 2+1 and 2 flavor realizations thereof which we solve numerically. We present and discuss our findings in Sec. 6. Finally, we give some details above the numerical setup and present a novel approach to solve FRG flow equations in Sec. 7.

1.1 Notations and Conventions

Throughout this thesis we will be working in Euclidean space-time. The transition from Minkowski space-time to Euclidean space-time is performed by a Wick rotation of the time coordinate $t \rightarrow -ix^0$ and results in the 4-vector product

$$x^2 = t^2 - |\mathbf{x}|^2 \rightarrow -(x^0)^2 - |\mathbf{x}|^2 = -|x_E|^2. \quad (1.1)$$

We will omit the subscript E from now on and all quantities are to be understood as evaluated in Euclidean space-time.

For the frequently occurring space and momentum integrals we use the shorthand notation

$$\text{space: } \int_x \equiv \int d^4x, \quad \text{momentum: } \int_{\star p} \equiv \int \frac{d^4p}{(2\pi)^4}, \quad (1.2)$$

where we add a star to identify the momentum integrals.

We implement finite temperature in the standard fashion and use the notation

$$\int_x f(x) \rightarrow \int_0^{1/T} d\tau \int d^3\mathbf{x} f(\tau, \mathbf{x}), \quad \int_{\star p} f(p) \rightarrow T \sum_{n=-\infty}^{\infty} \int \frac{d^3p}{(2\pi)^3} f(\omega_n, \mathbf{p}), \quad (1.3)$$

where for bosons $\omega_n = 2n\pi T$ and for fermions $\omega_n = (2n+1)\pi T$ are the respective Matsubara frequencies.

In sections 2.1 and 4 we make use of a compactified notation put forward in [40]. Fields of arbitrary type are collected in a *super-field* Φ . For example if we have fields with spin 0, $\frac{1}{2}$, 1 the super-field might read $\Phi = (\phi, \psi, \bar{\psi}, A)^T$ where ψ and $\bar{\psi}$ are Grassmann valued. We denote all substructure of the super-field by a general *multi-index* with bold typesetting $\Phi_{\mathbf{a}}$. Dependent on the specific field the multi-index may comprise indices for space-time, Lorentz, color, flavor and so on. It is understood that the individual field types generally have different internal indices.

Raising and lowering of the general multi-index is done by the *generalized metric* γ^{ab}

$$\Phi^{\mathbf{a}} = \gamma^{\mathbf{ab}} \Phi_{\mathbf{b}}. \quad (1.4)$$

It is the direct sum of all internal metrics and includes a non-trivial *field space metric* if fermionic fields are comprised in Φ . For the above specified super-field the field space metric reads

$$\gamma^{ab} = \begin{pmatrix} 1 & 0 & 0 & 0 \\ 0 & 0 & 1 & 0 \\ 0 & -1 & 0 & 0 \\ 0 & 0 & 0 & 1 \end{pmatrix} \quad (1.5)$$

so that the contraction of Φ with itself reads $\Phi^a \Phi_a = \int_x (\phi^2 + 2\bar{\psi}\psi + A^2)$ where contraction over remaining internal indices is implied. We define the source term corresponding to Φ as $J^a = (J_\phi, J_\psi, -J_{\bar{\psi}}, J_A)$ so that the usual contraction with Φ_a is given by

$$J^a \Phi_a = \int_x (J_\phi \phi + J_\psi \psi + \bar{\psi} J_{\bar{\psi}} + J_A A). \quad (1.6)$$

Finally we mention one identity of the field space metric which will be used later on

$$\gamma^a_b = (-1)^{ab} \delta^a_b, \quad (-1)^{ab} = \begin{cases} -1 & \mathbf{a} \text{ and } \mathbf{b} \text{ fermionic} \\ 1 & \text{otherwise} \end{cases} \quad (1.7)$$

The true power of this notation is only realized when one is dealing with composite fields. However, here we simply use it to simultaneously deal with fermions and bosons.

Two

Functional Methods

Historically quantum field theory was first developed using the canonical quantization formalism which has a somewhat intuitive connection to quantum mechanics. It involves a generalization of the canonical commutation relations to quantum field operators and thus generates creation and annihilation operators akin to second quantization formalism in many body theory. There is however another approach, the so called path integral approach which has proven to be invaluable to quantum field theory and has been widely used since the 1950s. It is equivalent to the canonical quantization formalism and is based on the action principle of classical mechanics. In this thesis we will also benefit from the close resemblance of the path integral formalism to statistical mechanics.

2.1 The Generating Functional

We want to calculate n -point correlation functions which are given as the vacuum expectation value (VEV) of the time ordered product of n fields and can be written as

$$\langle T\Phi_{a_1} \dots \Phi_{a_n} \rangle = \frac{\int \mathcal{D}\Phi \Phi_{a_1} \dots \Phi_{a_n} e^{-S[\Phi]}}{\int \mathcal{D}\Phi e^{-S[\Phi]}}. \quad (2.1)$$

Here $S[\Phi] = \int_x \mathcal{L}(\Phi(x))$ is the action in Euclidean space-time. The path integral $\int \mathcal{D}\Phi$ is a deceptively simple notation for a summation over all continuously infinite field configurations $\Phi(x)$ and can only be analytically evaluated for special cases i.e. the Gaussian integral in field space.

A more elegant way to compute correlation functions is given through the *generating functional*

$$Z[J] = \int \mathcal{D}\Phi \exp[-S[\Phi] + J^a \Phi_a] \quad (2.2)$$

where J is a so called source term resembling external sources in classical equations of motion. We define the generating functional in Euclidean space-time because the connection to statistical mechanics becomes apparent in this formulation. The direct analogue of the generating functional is the partition function which is given as the sum over all possible states weighted with a Boltzmann factor. This close correspondence enables us to apply our knowledge of statistical mechanics to quantum field theory and vice versa.

Using the generating functional we can compute the desired correlation functions but we first have to define the functional derivative which is the functional generalization of standard differentiation. In our multi-index notation we have

$$\frac{\delta}{\delta J^a} J^b \Phi_b = \Phi_a. \quad (2.3)$$

The usual rules for differentiation apply when differentiating composite functionals. With this it is easy to see that each differentiation of $Z[J]$ with respect to J^a gives a factor of Φ_a in the integrand. Subsequently setting the source term to zero we recover Eq. (2.1)

$$\langle T\Phi_{a_1} \dots \Phi_{a_n} \rangle = \frac{1}{Z[0]} \left. \frac{\delta^n Z[J]}{\delta\Phi_{a_n} \dots \delta\Phi_{a_1}} \right|_{J=0}. \quad (2.4)$$

2.2 The Effective Action

In classical field theory the vacuum expectation value of a field is given as the stationary point of the action. In quantum field theory the classical expectation value receives corrections due to quantum fluctuations similar to thermal fluctuations in a statistical system. Fortunately, it is possible to construct a functional that gives the true expectation value including fluctuations at its stationary point. This construction is analogous to a Legendre transformation from the free energy to the Gibbs free energy which upon minimization gives the expectation value including thermal fluctuations. We call the QFT analogue the *quantum effective action* (or simply *effective action*) and it is defined by

$$\Gamma[\Phi_J] = J^a \Phi_{J_a} - W[J] \quad (2.5)$$

with $W[J]$ the quantum field theory analogue of the free energy. $W[J]$ is given as the sum of all connected vacuum-vacuum diagrams in the presence of a source J . Since $Z[J]$ is the sum of every possible vacuum-vacuum diagram we can write it as a sum over connected diagrams

$$Z[J] = \sum_N \frac{1}{N!} W[J]^N = e^{W[J]} \quad (2.6)$$

where the $N!$ factor cancels out permutations.

The effective action is a functional of the classical expectation value in the presence of a source J which is given by differentiating $W[J]$ with respect to the source

$$\frac{\delta W[J]}{\delta J^a} = \langle \Phi_a \rangle_J \equiv \Phi_{J_a}. \quad (2.7)$$

This equality can be formally inverted to give $J[\Phi_J]$ which is needed for the Legendre transformation to be well defined. We can verify that the effective action satisfies the quantum equation of motion

$$\begin{aligned} \frac{\delta \Gamma[\Phi_J]}{\delta \Phi_{J_a}} &= \frac{\delta J^b}{\delta \Phi_{J_a}} \Phi_{J_b} + J^a - \frac{\delta W[J]}{\delta \Phi_{J_a}} \\ &= \frac{\delta J^b}{\delta \Phi_{J_a}} \frac{\delta W[J]}{\delta J^b} + J^a - \frac{\delta J^b}{\delta \Phi_{J_a}} \frac{\delta W[J]}{\delta J^b} \\ &= J^a \end{aligned} \quad (2.8)$$

where we have used Eq. (2.7) between the first and second line.

The effective action has a few noteworthy properties: One can show that $\Gamma[\Phi_J]$ is the sum of all *one-particle-irreducible* vacuum-vacuum diagrams which are diagrams that can not be disconnected by cutting a single line. Also, it is possible to calculate $W[J]$ as the sum of *tree* graphs if instead of the classical action $S[\Phi]$ the effective action is used. This implies that all loop corrections are included in the vertices calculated with the effective action, hence its name. Furthermore, because of its definition as a Legendre transformation $\Gamma[\Phi_J]$ is a convex functional. This property will be of special interest for the later discussion.

2.3 The Effective Potential

In many cases the vacuum state is expected to be invariant under translations and Lorentz transformations. In such cases the solutions to (2.8) become constants so that all functional character is lost and the equation of motion becomes a standard partial differential equation. For a vanishing source term we have

$$\frac{\partial}{\partial \Phi} \Gamma(\Phi) = 0. \quad (2.9)$$

Since no kinetic terms contribute to the effective action for constant fields one writes

$$\Gamma[\Phi]|_{\Phi=const} = \Gamma(\Phi) = \int_x \mathcal{U}(\Phi) = V_d \mathcal{U}(\Phi) \quad (2.10)$$

where V_d is the d -dimensional volume and $\mathcal{U}(\Phi)$ the so called *effective potential*. This is also the first term in a derivative expansion of the effective action as we will see later.

Already a lot of information is stored in the effective potential. For example the true ground state including quantum fluctuations can be extracted by minimizing the potential. This means that e.g. symmetry breaking can be intuitively understood through the effective potential.

We conclude with a further analogy to statistical mechanics. If we include a chemical potential in the action $S[\Phi] \rightarrow S[\Phi] + \mu \mathcal{N}$ and evaluate the corresponding generating functional for a vanishing source term we recover a form reminiscent of the grand canonical partition function

$$Z_{GC} = \text{Tr} e^{-\beta(H - \mu \mathcal{N})}. \quad (2.11)$$

In this case the effective action $\Gamma[\Phi_{J=0}] = -\ln Z[J=0]$ corresponds to the *grand potential* $\Omega = -\frac{1}{\beta} \ln Z$ and therefore \mathcal{U} can be understood as the *grand potential density* Ω/V .

Three

Quantum Chromodynamics

Quantum Chromodynamics (QCD) is the quantum field theory describing the strong force. Its building blocks consist of quarks and gluons where the latter are understood as the mediating particles of the strong force - the gauge bosons of QCD. Quarks carry so called color charge and this gives rise to the gauge group $SU(N_c = 3)$ upon which QCD is constructed, as we will see shortly. Additionally, quarks come in 6 *flavors* with widely different masses (see. Tab. 3.1). Because the up, down and strange quarks are much lighter than the remaining three they are often called the *light quarks* and for this thesis we will only consider their dynamics.

Asymptotic Freedom and Running of the Strong Coupling. At different energy and length scales the strength of the strong coupling changes. This is generally true for interacting field theories requiring renormalization and can be intuitively understood as a combination of screening and/or anti-screening effects at various length scales. The change of couplings is measured in so called beta-functions and in QCD it reads to one loop order

$$\beta_1(\alpha_s) = k \partial_k \alpha_s = \frac{\alpha_s^2}{6\pi} (2 N_f - 11 N_c) \quad (3.1)$$

where $\alpha_s = \frac{g_s^2}{4\pi}$ is the QCD analogue of the fine structure constant of QED. For $N_c = 3$ and $N_f < \frac{33}{2}$ the beta function is negative which is known as *asymptotic freedom* [3, 4]. It entails that the strong coupling vanishes in the high energy limit and becomes strong in the IR. In Fig. 3.1 α_s is shown as a function of the energy scale Q . The rise of the strong coupling at low energies leads to a breakdown of standard perturbation theory so that non-perturbative methods have to be developed to fully understand all aspects of QCD.

Color Confinement. Another curious property of QCD is the absence of colored states in the hadron spectrum. This property is called *confinement*, however, there is to this date no agreed upon definition connected with this term. Consequently, it is not a mathematically proven property of QCD. One possible way to express color confinement is with the statement

flavor	el. charge [e]	current mass
up	2/3	2.3 MeV
down	-1/3	4.8 MeV
strange	2/3	95 MeV
charm	-1/3	1.275 GeV
top	2/3	173.21 GeV
bottom	-1/3	4.66 GeV

Table 3.1: Electrical charge and current mass of each quark flavor. Masses taken from [41].

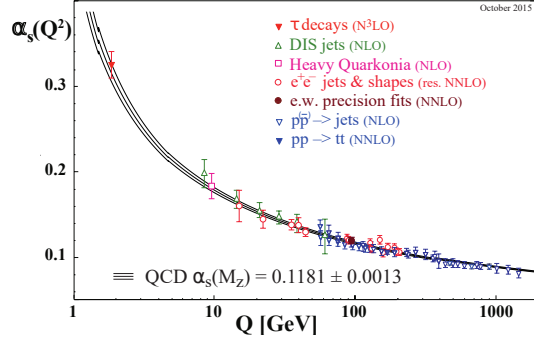


Figure 3.1: Summary of measurements of α_s as a function of the energy scale Q [41].

that all measurable particles must be color singlets. This statement has so far been confirmed by experimental data and it is also one of the first results of lattice QCD simulations.

In the limit of heavy quarks confinement manifests in a linearly rising potential between quarks and antiquarks

$$\lim_{r \rightarrow \infty} U^{q\bar{q}}(r) = \sigma r. \quad (3.2)$$

Here r is the distance between a quark and antiquark and σ is the string tension. Consequently, an infinite amount of energy is required to separate a quark-antiquark pair. This can never be achieved since it only takes a finite amount of energy to create a new pair from the vacuum. The original quark-antiquark pair therefore breaks up into two pairs before it can be separated.

3.1 QCD as a Non-Abelian Gauge Theory

The three field theories contained in the standard model are built upon the principle of gauge invariance. For QCD the gauge group is $SU(N_c)$. Therefore, quarks q and antiquarks \bar{q} transform in the fundamental representation of $SU(N_c)$

$$q(x) \rightarrow U(x)q(x), \quad \bar{q}(x) \rightarrow \bar{q}(x)U^\dagger(x). \quad (3.3)$$

An infinitesimal gauge transformation can be written as

$$U(x) = \mathbb{1} - i\omega^a(x)T^a + \mathcal{O}(\omega^2) \quad (3.4)$$

with $N_c^2 - 1$ generating matrices T^a for $a = 1, \dots, N_c^2 - 1$ which are Hermitian and traceless. Note that the gauge transformation is local¹ which generally breaks gauge invariance of standard derivative terms such as $\bar{q}\not{\partial}q$. This fault can be cured by introducing the covariant derivative

$$\partial_\mu \longrightarrow D_\mu = \mathbb{1}\partial_\mu - ig_s A_\mu = \mathbb{1}\partial_\mu - ig_s A_\mu^a T^a \quad (3.5)$$

where g_s is the strong coupling and A_μ^a the gauge fields decomposed in the basis of $SU(N_c)$. The gauge fields of QCD are commonly referred to as gluons. They are spin one particles and carry *color charge* denoted by the superscript a which is the QCD analogue of the electric charge. Using this substitution the kinetic term $\bar{\psi}\not{\partial}\psi$ becomes gauge invariant.

¹The transformation is dependent on space-time.

The newly found gauge fields also require a kinetic term to describe their dynamics and this is typically included through the field strength tensor

$$F_{\mu\nu}(x) = \frac{i}{g_s} [D_\mu, D_\nu] = \partial_\mu A_\nu - \partial_\nu A_\mu - ig_s [A_\mu, A_\nu] \quad (3.6)$$

which is itself not gauge invariant but transforms with

$$F_{\mu\nu}(x) \longrightarrow U(x) F_{\mu\nu}(x) U^\dagger(x). \quad (3.7)$$

The term $\frac{1}{2} \text{Tr}(F_{\mu\nu} F_{\mu\nu})$, however, is gauge invariant and turns out to be the only renormalizable quantity which also respects CT symmetry. This means that we have found our kinetic term for the gauge field so that the total Lagrangian reads

$$S_{\text{QCD}}[\bar{q}, q, A_\mu] = \int_x \mathcal{L}(\bar{q}, q, A_\mu) = \int_x \left[\bar{q} (\not{D} + M_q) q + \frac{1}{2} \text{Tr}(F_{\mu\nu} F_{\mu\nu}) \right]. \quad (3.8)$$

A gluon mass term $A_\mu A_\mu$ is not gauge invariant. Therefore, it is not present in the QCD Lagrangian and we conclude that gluons are massless particles.

An important feature of QCD is its non-Abelian nature. By expanding the field strength tensor as $F_{\mu\nu} = F_{\mu\nu}^a T^a$ we find

$$F_{\mu\nu}^a = \partial_\mu A_\nu^a - \partial_\nu A_\mu^a + g_s f^{abc} A_\mu^b A_\nu^c \quad (3.9)$$

where f^{abc} are the structure constants of $SU(N_c)$ defined by $[T^a, T^b] = i f^{abc} T^c$. Since for $SU(N_c = 3)$ the structure constants do not vanish² there are contributions with three and four gluon fields in $\frac{1}{2} \text{Tr}(F_{\mu\nu} F_{\mu\nu})$. This implies that there is gluon self interaction already at the classical level which is an important distinction to QED where photon-photon interactions are only possible through fluctuations.

QCD and the path integral formalism. Now that we have established the classical action of QCD the next step towards a solution of QCD in perturbation theory would be to derive Feynman rules. Applying canonical quantization turns out to be extremely tedious for non-Abelian theories [42]. Turning to the path integral formalism we encounter another problem: In a gauge theory physically equivalent states are connected by a gauge transformation. This fact leads to an overcounting in the path integral since it is a summation over *all* field configurations many of which (infinitely many) correspond to the same physical state. As shown by Faddeev and Popov [43] it is possible to cure this infinite overcounting by imposing a gauge fixing condition $\mathcal{F}^a(A_\mu) = 0$ in the path integral. Further complications arise due to the complex topological structure of *gauge orbits*³ so that gauge fixing can at best be achieved locally. This is known as *Gribov ambiguity* [44].

Incorporating the gauge fixing condition into the path integral the change in the measure introduces the *Faddeev-Popov determinant*. It can be rewritten in terms of so called *ghost* fields $c(x)$, $\bar{c}(x)$. They are complex scalar fields but due to their Grassmann valued nature they anti-commute which violates the spin-statistics theorem. Therefore, ghost fields are considered non-physical and they only appear as virtual particles in Feynman diagrams.

With the specific gauge condition $\mathcal{F}^a(A_\mu) = \partial_\mu A_\mu^a$ the action for gauge fixed QCD reads [45]

$$S_{\text{QCD}}^{\text{gf}}[\bar{q}, q, \bar{c}, c, A_\mu] = \int_x \left[\bar{q} (\not{D} + M_q) q + \frac{1}{2} \text{Tr}(F_{\mu\nu} F_{\mu\nu}) + \bar{c}^a \partial_\mu D_\mu^{ab} c^b + \frac{1}{2\zeta} (\partial_\mu A_\mu^a)^2 \right]. \quad (3.10)$$

²Groups where the commutator vanishes are called Abelian.

³Fields A_μ are considered to be in the same gauge orbit if they can be transformed into each other through gauge transformations.

3.2 Symmetries of QCD

Apart from the local $SU(N_c)$ symmetry that determines the interactions of QCD there are various global symmetries (approximately) realized in the action (3.8). These symmetries will play a crucial role in the construction of our truncation. Even more interesting than the symmetries themselves is how they are broken at low energies. The breaking of chiral symmetry will reveal two essentially different phases of QCD and they are the main topic of this thesis.

$U(1)_V$ Symmetry. We start with the most obvious symmetry which is the $U(1)_V$ symmetry. It is realized as a phase change of the quark fields

$$q(x) \rightarrow e^{i\omega} q(x), \quad \bar{q}(x) \rightarrow \bar{q}(x) e^{-i\omega} \quad (3.11)$$

which clearly leaves the QCD action invariant. For any continuous global symmetry we can calculate the conserved Noether current and a correspondent charge which is constant in time

$$\mathcal{J}_\mu(x) = \frac{1}{3} \bar{q}(x) \gamma_\mu q(x), \quad B(t) = \int d^3x \mathcal{J}_0(x) = \frac{1}{3} \int d^3x q^\dagger(x) q(x). \quad (3.12)$$

The charge is the *baryon number* so that $U(1)_V$ symmetry is directly responsible for baryon number conservation.

Isospin symmetry. If we assume all quark flavors to be of equal mass then the action exhibits a global $SU(N_f)$ symmetry

$$q(x) \rightarrow e^{i\omega_a T^a} q(x) \quad (3.13)$$

where T^a with $a = 1, \dots, N_f^2 - 1$ are the generators of $SU(N_f)$ acting solely on the flavor part of the quark field. This symmetry often referred to as isospin symmetry and its breaking pattern can give insight into the meson spectrum as will be seen later on. The conserved Noether currents and charges are

$$\mathcal{V}_\mu^a(x) = \bar{q}(x) \gamma_\mu T^a q(x), \quad Q^a(t) = \int d^3x \mathcal{V}_0^a(x) = \int d^3x \bar{q}^\dagger(x) T^a q(x). \quad (3.14)$$

Just as the generators the conserved charges form the $SU(N_f)$ Lie algebra

$$[Q^a, Q^b] = i f^{abc} Q^c. \quad (3.15)$$

The assumption that all quark flavors have the same mass is not realized in nature so that isospin symmetry is not an exact but an approximate symmetry. It works especially well for $N_f = 2$ since the difference in mass between up and down quark is small $m_d - m_u < 3.4$ MeV [41]. It also often applied to $N_f = 3$ since charm, top and bottom quarks are considerably heavier than up, down and strange quarks.

We note that even in the case of explicit isospin symmetry breaking by different quark masses the charge algebra defined in (3.15) still holds at each time instance even though the charge need not be conserved. The four divergence of the current can be evaluated to

$$\partial_\mu \mathcal{V}_\mu^a = i \bar{q} [M_q, T^a] q \quad (3.16)$$

where the commutator only vanishes if $M_q \sim \mathbb{1}$ and therefore the current is only conserved if quark masses are equal.

Chiral Symmetry. We go one step further away from the physically realized case by assuming that we have N_f massless quarks. The other quark flavors are assumed to be infinitely heavy and therefore their dynamics can be neglected.

We define two projection matrices

$$P_{R/L} = \frac{1}{2}(1 \pm \gamma_5). \quad (3.17)$$

Applied to a quark spinor they project onto spinors of unique *handedness*⁴

$$q_{R/L} = P_{R/L} q, \quad \bar{q}_{R/L} = \bar{q} P_{L/R} \quad (3.18)$$

and in accordance with standard projection properties⁵ we get

$$q(x) = q_R(x) + q_L(x). \quad (3.19)$$

In the limit of massless quarks the fermionic part of the QCD Lagrangian separates into contributions from left and right handed quarks

$$\bar{q} \not{D} q = \bar{q}_R \not{D} q_R + \bar{q}_L \not{D} q_L \quad (3.20)$$

which is commonly referred to as chiral symmetry. It is easy to see that non vanishing quark masses mix left and right handed spinors and therefore break chiral symmetry

$$\bar{q} M_q q = \bar{q}_R M_q q_L + \bar{q}_L M_q q_R. \quad (3.21)$$

From this formulation it is clear that for the chiral limit we can define two $U(N_f)$ transformations that act separately on the left- and right handed spinors and leave the Lagrangian invariant. We denote these symmetries as

$$U(N_f)_L \otimes U(N_f)_R. \quad (3.22)$$

This symmetry group can be decomposed into

$$SU(N_f)_L \otimes U(1)_L \otimes SU(N_f)_R \otimes U(1)_R \quad (3.23)$$

and the conserved currents are given by

$$\mathcal{J}_{\mu,R/L} = \bar{q}_{R/L} \gamma_\mu q_{R/L}, \quad \mathcal{J}_{\mu,R/L}^a = \bar{q}_{R/L} \gamma_\mu T^a q_{R/L}. \quad (3.24)$$

We can make the connection to isospin symmetry by defining vector and axial currents

$$\begin{aligned} \mathcal{V}_\mu &= \mathcal{J}_{\mu,R} + \mathcal{J}_{\mu,L} = \bar{q} \gamma_\mu q, & \mathcal{V}_\mu^a &= \mathcal{J}_{\mu,R}^a + \mathcal{J}_{\mu,L}^a = \bar{q} \gamma_\mu T^a q, \\ \mathcal{A}_\mu &= \mathcal{J}_{\mu,R} - \mathcal{J}_{\mu,L} = \bar{q} \gamma_\mu \gamma_5 q, & \mathcal{A}_\mu^a &= \mathcal{J}_{\mu,R}^a - \mathcal{J}_{\mu,L}^a = \bar{q} \gamma_\mu \gamma_5 T^a q \end{aligned} \quad (3.25)$$

⁴We use the anti-commutator relation $\{\gamma_\mu, \gamma_5\} = 0$ for the adjoint spinor.

⁵Properties of projection operators include $P_{R,L}^2 = \mathbb{1}$, $P_R P_L = 0$, $P_R + P_L = \mathbb{1}$.

and the corresponding charges

$$\begin{aligned} Q_V(t) &= \int d^3x \mathcal{V}_0^a = \int d^3x q^\dagger q, & Q_V^a(t) &= \int d^3x \mathcal{V}_0^a = \int d^3x q^\dagger T^a q, \\ Q_A(t) &= \int d^3x \mathcal{A}_0^a = \int d^3x q^\dagger \gamma_5 q, & Q_A^a(t) &= \int d^3x \mathcal{A}_0^a = \int d^3x q^\dagger \gamma_5 T^a q. \end{aligned} \quad (3.26)$$

The $U(1)_V$ symmetry corresponding to \mathcal{V}_μ is the symmetry discussed above which lead to baryon number conservation and $SU(N_f)_V$ defined by \mathcal{V}_μ^a is just the isospin symmetry. \mathcal{V}_μ^a is conserved even for finite but equal quark masses. This is not true for the axial current since its four divergence

$$\partial_\mu \mathcal{A}_\mu^a = i\bar{q}\{M_q, T^a\}\gamma_5 q \quad (3.27)$$

is finite for $M_q \neq 0$. Finally the $U(1)_A$ corresponding to the axial current \mathcal{A}_μ plays a special role in QCD since it is anomalously broken, i.e. the symmetry is broken on the quantum level. We will discuss this in more detail in Sec. 3.4.

3.3 Spontaneous Breaking of Chiral Symmetry

Spontaneous symmetry breaking is an important mechanism in many areas of physics. It is defined as a symmetry that is realized in the action of a theory but not in its ground state. Therefore the symmetry of a theory is *hidden* and not observed in its measurements. Notable examples for spontaneous symmetry breaking include the magnetization of a ferromagnet and the Higgs mechanism.

We already noted that chiral symmetry is not realized in the QCD vacuum, because finite quark masses break chiral symmetry explicitly. Nevertheless, for the two (three) lightest quark flavors chiral symmetry should be a good approximate symmetry. Supposing that chiral symmetry is realized in the QCD vacuum there should exist parity partners of equal mass for the vector and axial-vector mesons. This is not the case for the observed meson spectrum. For example, the two lightest vector and axial-vector mesons have a mass of $m_\rho = 770$ MeV and $m_{a_1} = 1260$ MeV [41] which leads us to the conclusion that chiral symmetry is not even approximately realized. An explanation was provided by Nambu and Jona-Lasinio: They suggested that $SU(N_f)_A$ was spontaneously broken in the QCD vacuum [46].

An important implication of spontaneous chiral symmetry breaking is the emergence of massless bosons, the *Goldstone bosons* [47, 48]. For every broken global symmetry one such particle arises so that for spontaneously broken $SU(N_f)_A$, $N_f^2 - 1$ massless bosons should appear. Because finite quark masses additionally break chiral symmetry explicitly the Goldstone bosons acquire a small mass and become *pseudo Goldstone bosons*. This reasoning is supported by experimental findings; a meson triplet, made up of the pions π^0, π^\pm , is observed which is significantly lighter than all other mesons. They can be understood as the pseudo Goldstone bosons of spontaneously broken $SU(2)_A$. Furthermore, a meson octet of relatively light mass is found which correspond to the pseudo Goldstone bosons of spontaneously broken $SU(3)_A$.

That the ground state is not invariant under $SU(N_f)_A$ can be formulated in terms of the axial charges

$$Q_A^a |0\rangle \equiv |\pi_a\rangle \neq 0 \quad (3.28)$$

i.e. the axial charges do not annihilate the vacuum but create a state of pseudo scalar particles that we suggestively name pions. On the other hand, for equal quark masses $SU(N_f)_V$ is still intact so that the vector charges annihilate the vacuum $Q_V^a |0\rangle = 0$.

In QCD vacuum $U(1)_A$ symmetry is not spontaneously broken, because it is already anomalously broken. It is possible that the *axial anomaly* is weakened at high temperatures or densities

so that there might exist a point in the QCD phase diagram where $U(1)_A \otimes SU(N_f)_A \simeq U(N_f)_A$ is spontaneously broken. Consequently N_f^2 (pseudo) Goldstone bosons should be observed. In the experimentally measured meson spectrum the η' meson corresponds to $U(1)_A$ symmetry. It has a considerably higher mass than the η meson ($m_{\eta'} = 957.8$ MeV vs. $m_\eta = 547.9$ MeV) which is a direct consequence of anomalous breaking of $U(1)_A$.

One possible way to understand the dynamic breakdown of chiral symmetry is by an analogy to the formation of electron pairs in a superconductor. At low energies quarks and antiquarks feel a strong attractive force as indicated by the rise of the strong coupling. If, additionally, the quarks can be considered massless or very light then the energy cost of creating a quark-antiquark pair is small. Therefore, one can imagine the QCD vacuum to be filled with quark-antiquark pairs (condensates). Because of momentum conservation the total momentum and total angular momentum of the condensate must be zero. This means that the condensate has non-vanishing chirality. We can express the *chiral condensate* as the expectation value

$$\langle \bar{q}q \rangle = \langle \bar{q}_R q_L \rangle + \langle \bar{q}_L q_R \rangle \quad (3.29)$$

which couples left and right handed quarks and therefore breaks chiral symmetry. It can be used to identify the state of chiral symmetry: If $\langle \bar{q}q \rangle = 0$ chiral symmetry is realized in the ground state and $\langle \bar{q}q \rangle \neq 0$ signals chiral symmetry is explicitly and/or spontaneously broken. The chiral condensate therefore acts as an order parameter for the chiral phase transition of QCD.

3.4 Anomalous Breaking of $U(1)_A$

As already mentioned, the absence of a flavor-singlet (pseudo) Goldstone boson can be explained by the fact that the $U(1)_A$ symmetry is not spontaneously but instead anomalously broken in QCD. An anomalously broken symmetry is conserved at the classical level but broken by quantum fluctuations. Generally, one finds anomalies when renormalization is required but no regulator can be formulated that preserves the symmetry. Crucially, Goldstone's theorem does not apply to anomalously broken symmetries since quantum fluctuations generate a mass term and therefore no Goldstone boson arises.

Contrary to a spontaneously broken symmetry where the associated current is still conserved an anomalously broken symmetry sees a non-vanishing contribution to the divergence of the symmetry current. In the case of $U(1)_A$ we have $\partial_\mu \mathcal{A}_\mu = \partial_\mu \bar{q} \gamma_\mu \gamma_5 q \neq 0$. The need for renormalization of symmetry currents becomes evident if we write the current as a limit

$$\mathcal{A}_\mu = \lim_{x \rightarrow y} \bar{q}(x) \gamma_\mu \gamma_5 q(y) \quad (3.30)$$

which is potentially quite divergent. Of course, this is also true for \mathcal{A}_μ^a , \mathcal{V}_μ^a , \mathcal{V}_μ , the currents associated with $SU(N_f)_A$ and $U(N_f)_V$. For the vector currents a simple argument can show that they can not be affected by anomalies: The charges associated with vector symmetries always carry some physical meaning⁶ and lead to important conservation laws. Breaking of such conservation laws on the quantum level would ultimately violate gauge symmetry and therefore render the theory useless. This is not a problem for axial symmetries and only a careful calculation reveals that the anomalous contribution vanishes for $SU(N_f)_A$.

We start our analysis of the $U(1)_A$ anomaly with the fermionic part of the QCD action (3.8) in the chiral limit. Performing a *local* $U(1)_A$ transformation we get

$$S \rightarrow S' = \int_x \bar{q} e^{i\omega(x)\gamma_5} i \not{D} e^{i\omega(x)\gamma_5} q = S - (\partial_\mu \omega(x)) \mathcal{A}_\mu. \quad (3.31)$$

⁶For example baryon density, color charge, flavor charge.

If we carelessly plug this into the path integral

$$Z[0] = \int \mathcal{D}q' \mathcal{D}\bar{q}' e^{-S[q', \bar{q}']} = \int \mathcal{D}q \mathcal{D}\bar{q} e^{-S[q, \bar{q}]} \left(1 + i \int_x \omega(x) \partial_\mu \mathcal{A}_\mu \right) \quad (3.32)$$

we could come to the conclusion that $\langle \partial_\mu \mathcal{A}_\mu \rangle = 0$ if we were to assume that the integral measure is not changed by the transformation. It turns out that this is not necessarily correct for axial transformations. Rather we have to explicitly calculate the functional determinant

$$\mathcal{D}q' \mathcal{D}\bar{q}' = (\det C)^{-2} \mathcal{D}q \mathcal{D}\bar{q}. \quad (3.33)$$

It can be evaluated for example following *Fujikawa's method* [49] by expanding the determinant in eigenfunctions of \not{D} . Doing so, one encounters a singularity which can for example be regularized with a Gaussian cutoff function. We here simply state the result of this calculation which involves various trace operations and subsequently sending the cutoff parameter towards infinity. The final four divergence of the axial current reads

$$\partial_\mu \mathcal{A}_\mu = \frac{g_s^2 N_f}{8\pi^2} \text{Tr}(\tilde{F}_{\mu\nu} F_{\mu\nu}) \quad (3.34)$$

where $\tilde{F}_{\mu\nu} = \frac{1}{2} \varepsilon_{\mu\nu\alpha\beta} F_{\alpha\beta}$. Since this expression generally does not vanish it must be the anomalous contribution to the axial current.

In order to see that $SU(N_f)_A$ is not afflicted by an anomaly the same calculation can be performed for the corresponding current and one finds

$$\partial_\mu \mathcal{A}_\mu^a = \frac{g_s^2}{(4\pi)^2} \varepsilon^{\alpha\beta\mu\nu} F_{\alpha\beta}^b F_{\mu\nu}^c \text{Tr}_F(T_a) \text{Tr}_C(T_b T_c) = 0. \quad (3.35)$$

In contrary to the $U(1)_A$ case this expression vanishes because the generators of $SU(N_f)$ are traceless and therefore $\text{Tr}_F T_a = 0$.

The 't Hooft Interaction. It has been discovered by 't Hooft that the anomaly leads to instanton induced effective $2N_f$ quark interactions [37]

$$\mathcal{L}_{det} = \kappa (\det \bar{q} P_L q + \det \bar{q} P_R q) \quad (3.36)$$

where the constant κ is related to instanton density. The determinant is evaluated in flavor space which implies that the $2N_f$ quark interaction mixes quarks of different flavor. It explicitly breaks $U(1)_A$ symmetry and within a NJL-type model it can also be used to implement spontaneous chiral symmetry breaking. In the path integral formalism the 't Hooft interaction term can be expressed by auxiliary fields which are then identified with physical mesons. This has been done to lowest order stationary phase approximation in [38] and beyond [50]. The wrong mass of the η' meson in effective $U(3)_L \otimes U(3)_R$ theories is essentially corrected by the 't Hooft determinant, see i.e. [51].

Four

The Functional Renormalization Group

Our goal is it to investigate chiral symmetry restoration of QCD at high temperatures and densities. As discussed in the last section these macroscopic effects are not accessible by standard perturbation theory. The need for non-perturbative methods becomes even more urgent in the vicinity of a critical point. There the correlation length ζ diverges such that fluctuations of all length scales have to be accounted for which can not be accomplished in a perturbative expansion. This however, is exactly the point where the functional renormalization group shines.

Renormalization group in general deals with the physics of scales. It connects the known microscopic interactions of a given theory to generally complex and interesting long range interactions. In the case of QCD this could be for example the formation of hadronic matter in the low energy sector or distinct properties such as confinement. In order to make this transition from microscopic to macroscopic scales we have to consider fluctuations on all scales in between.

The functional renormalization group is based on the RG idea of Wilson. Instead of treating all fluctuations at the same time fluctuations of a small momentum range (also called momentum shells) are integrated out successively. This concept can be nicely combined with the functional approach to quantum field theory. The path integral in the partition function is essentially divided into separate contributions from fluctuations with different momenta. Starting from the classical action with no fluctuations included one integrates over low range, high momentum fluctuations going down towards long range, low momentum modes. This is not only a convenient method to find the full solution of a theory but also allows a detailed investigation of what interactions contribute at what momentum scale. This applies especially to QCD since there is a wide variety of different degrees of freedom that become dominant at different energy scales.

Considering how the effective action or arbitrary correlation functions change with an additional momentum shell integration reveals the differential structure of FRG equations which has various analytic and numerical advantages over the integral structure of standard field theory. The differential equations of FRG are typically called flow equations and here we will only consider the flow equation for a scale dependent effective action Γ_k which was first suggested by Wetterich in 1993 [52].

4.1 The Wetterich Equation

Point of our investigation is the *scale dependent effective action* Γ_k . It interpolates smoothly between the classical action at some cutoff scale Λ and the full effective action Γ as $k \rightarrow 0$

$$\Gamma_{k \rightarrow \Lambda} = S, \quad \Gamma_{k \rightarrow 0} = \Gamma. \quad (4.1)$$

The *RG scale* k loosely speaking tells us that fluctuations of momenta between k and Λ have been included in Γ_k . This is a direct implementation of Wilson's RG idea and will lead

us to the flow of the scale dependent effective action $\partial_k \Gamma_k$.

In order to define the scale dependent effective action we start by adding an IR regulating term to the classical action

$$S[\Phi] \rightarrow S[\Phi] + \Delta S_k[\Phi] \quad (4.2)$$

so that the now scale dependent partition function reads

$$Z_k[J] = \int \mathcal{D}\Phi \exp(-S[\Phi] - \Delta S_k[\Phi] + J^a \Phi_a). \quad (4.3)$$

The regulator term can for example be written as

$$\Delta S_k[\Phi] = \frac{1}{2} \Phi_a R_k^{ab} \Phi_b. \quad (4.4)$$

If R_k^{ab} is diagonal this regulator term is quadratic in the fields and can therefore be understood as a scale dependent mass term. For a single bosonic field we can express it in momentum space as

$$\Delta S_k[\varphi] = \frac{1}{2} \int_{\star p} \varphi(-p) R_k(p) \varphi(p). \quad (4.5)$$

The following conditions have to be met by the regulator function $R(p)$ so that the classical action is recovered in the UV and the full theory as $k \rightarrow 0$:

$$\lim_{k \rightarrow \Lambda \rightarrow \infty} R_k(p) = \infty, \quad \lim_{k \rightarrow 0} R_k(p) = 0. \quad (4.6)$$

On the scales in between we require $R_k(p)$ to suppress fluctuations of momentum $p^2 \lesssim k^2$ which can be implemented by

$$R_k(p)|_{p^2 \lesssim k^2} \sim k^2 \quad (4.7)$$

which effectively adds a mass $m^2 \sim k^2$ to the considered momentum modes. For $q^2 \geq k^2$ all fluctuations are to be included and therefore the regulator function should fall off

$$R_k(p)_{k^2/p^2 \rightarrow 0} = 0. \quad (4.8)$$

Typical regulator function that satisfy all of the above conditions include¹

- the exponential regulator: $R_k(p) = \frac{p^2}{e^{p^2/k^2} - 1}$,
- the optimized regulator: $R_k(p) = (k^2 - p^2)\theta(k^2 - p^2)$,
- the quartic regulator: $R_k(p) = \frac{k^4}{p^2}$,
- the sharp regulator: $R_k(p) = \frac{p^2}{\theta(k^2 - p^2)} - p^2$,
- the Callan-Symanzik regulator: $R_k(p) = k^2$.

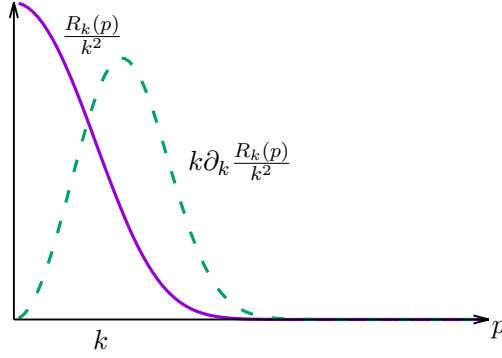


Figure 4.1: The exponential regulator (solid) and its scale derivative (dashed) in dependence of p .

As an example, we show the momentum dependence of the exponential regulator and its scale derivative in Fig. 4.1.

In direct analogy to Sec. 2.1 we define the *scale dependent generating functional*

$$W_k[J] = \ln Z_k[J] \quad (4.9)$$

which gives rise to the partially dressed, connected two point function or propagator

$$G_{k,ab} \equiv \frac{\delta^2 W_k}{\delta J^a \delta J^b} = \langle \Phi_{Jb} \Phi_{Ja} \rangle_{\text{con.}}. \quad (4.10)$$

For a constant source term we evaluate the scale derivative of the generating functional

$$\begin{aligned} \partial_k W_k[J] &= \partial_k \ln Z_k[J] = \langle -\partial_k \Delta S_k[\Phi] \rangle \\ &= -\frac{1}{2} (\partial_k R_k^{ab}) \langle \Phi_a \Phi_b \rangle \\ &= -\frac{1}{2} (\partial_k R_k^{ab}) (G_{k,ab} + \Phi_{Ja} \Phi_{Jb}) \\ &= -\frac{1}{2} (\partial_k R_k^{ab}) G_{k,ab} - \partial_k \Delta S_k[\Phi_J] \end{aligned} \quad (4.11)$$

with $\Phi_{Ja} \equiv \langle \Phi_a \rangle_J$ and we have used $\langle \Phi \Phi \rangle = \langle \Phi \Phi \rangle_{\text{con.}} + \langle \Phi \rangle \langle \Phi \rangle$ in the third line. Finally we define the *scale dependent effective action* as a modified Legendre transformation

$$\Gamma_k[\Phi_J] = -W_k[J] + J^a \Phi_{Ja} - \Delta S_k[\Phi_J]. \quad (4.12)$$

where we again substitute $J \rightarrow J[\Phi_J]$ by formally inverting

$$\Phi_{Ja} = \frac{\delta W_k[J]}{\delta J^a}. \quad (4.13)$$

Both Φ_J and J are generally scale dependent, however we will assume here that we can impose all scale dependence onto the source $J \equiv J_k$. A full derivation including scale dependent fields can be found for example in [40].

¹The regulator functions generally have to be adjusted for various field types.

The regulator term in the modified Legendre transformation can spoil the convexity of Γ_k which becomes important for example when investigating spontaneous symmetry breaking. However, since $\Delta S_{k \rightarrow 0} \rightarrow 0$ the standard Legendre transformation is obtained and convexity therefore restored in the IR.

We find that the quantum equation of motion receives a correction due to the regulator term

$$\frac{\delta(\Gamma_k[\Phi_J] + \Delta S_k[\Phi_J])}{\delta\Phi_{J\mathbf{a}}} = \gamma_{\mathbf{a}}^{\mathbf{d}} J^{\mathbf{d}} \quad (4.14)$$

where we have used $J^{\mathbf{a}}\Phi_{J\mathbf{a}} = \Phi_{J\mathbf{a}}J^{\mathbf{b}}\gamma_{\mathbf{b}}^{\mathbf{a}}$. Applying a second derivative to this expression yields

$$\frac{\delta^2\Gamma_k}{\delta\Phi_{J\mathbf{b}}\delta\Phi_{J\mathbf{a}}} + R_k^{\mathbf{ba}} = \gamma_{\mathbf{a}}^{\mathbf{d}} \frac{\delta J^{\mathbf{d}}}{\delta\Phi_{J\mathbf{b}}}. \quad (4.15)$$

We contract this with the propagator and use Eq. (4.13) to get

$$\left(\frac{\delta^2\Gamma_k}{\delta\Phi_{J\mathbf{b}}\delta\Phi_{J\mathbf{a}}} + R_k^{\mathbf{ba}} \right) \cdot \frac{\delta^2 W_k}{\delta J^{\mathbf{a}}\delta J^{\mathbf{c}}} = \gamma_{\mathbf{a}}^{\mathbf{d}} \frac{\delta J^{\mathbf{d}}}{\delta\Phi_{J\mathbf{b}}} \cdot \frac{\delta\Phi_{J\mathbf{c}}}{\delta J^{\mathbf{a}}} = \gamma_{\mathbf{c}}^{\mathbf{b}}. \quad (4.16)$$

Finally, we can invert Eq. (4.16) to find an expression for the two point function

$$G_{k,\mathbf{ac}} = \left(\Gamma_k^{(2)} + R_k \right)_{\mathbf{ab}}^{-1} \gamma_{\mathbf{b}}^{\mathbf{c}} \quad (4.17)$$

where we have introduced the shorthand notation

$$(\Gamma^{(n)})_{\mathbf{a}_1 \dots \mathbf{a}_n} \equiv \frac{\delta^n \Gamma_k}{\delta\Phi_{J\mathbf{a}_1} \dots \delta\Phi_{J\mathbf{a}_n}}. \quad (4.18)$$

To arrive at the Wetterich equation we evaluate the scale derivative of the effective action

$$\begin{aligned} \partial_k \Gamma_k[\Phi_J] &= -\partial_k(W_k[J_k]) + (\partial_k J_k^{\mathbf{a}})\Phi_{J\mathbf{a}} - \partial_k \Delta S_k[\Phi_J] \\ &= -\partial_k W_k[J] - (\partial_k J_k^{\mathbf{a}}) \frac{\delta W_k[J]}{\delta J^{\mathbf{a}}} + (\partial_k J^{\mathbf{a}})\Phi_{J\mathbf{a}} - \partial_k \Delta S_k[\Phi_J] \\ &\stackrel{(4.13)}{=} -\partial_k W_k[J] - \partial_k \Delta S_k[\Phi_J] \\ &\stackrel{(4.11)}{=} \frac{1}{2} G_{k,\mathbf{ab}} \partial_k R_k^{\mathbf{ab}}. \end{aligned} \quad (4.19)$$

This expression can be brought into the form of a trace by permuting the fields in the propagator $G_{k,\mathbf{ab}} \rightarrow G_{k,\mathbf{ba}}$ (or in $R_k^{\mathbf{ab}}$) which introduces an additional minus sign for Grassmann valued fields and no sign for bosonic fields. We keep track of this distinction by introducing the so called *super trace* which includes apart from the usual trace operation an integration over continuous indices and a minus sign for Grassmann valued fields. The Wetterich equation in operator notation now reads

$$\partial_t \Gamma_k[\Phi_J] = \frac{1}{2} \text{STr}(G_k \cdot \partial_t R_k) = \frac{1}{2} \text{STr}\left((\Gamma^{(2)} + R_k)^{-1} \gamma \cdot \partial_t R_k\right). \quad (4.20)$$

where we have introduced the so called *RG-time* $t = \ln(k/\Lambda)$ so that $\partial_t = k\partial_k$.

A few general remarks about the Wetterich equation are in order:

Wetterich equation for one boson field. Let us evaluate the Wetterich equation for a single bosonic field. We assume R_k^{ab} to be a local operator and therefore $R_k(p, q) \sim (2\pi)^d \delta(p+q)$. We find

$$\partial_t \Gamma_k = \frac{1}{2} \int_{\star p} G_k(-p, p) \partial_t R_k(p) = \frac{1}{2} \int_{\star p} (\Gamma^{(2)} + R_k)^{-1}(-p, p) \partial_t R_k(p). \quad (4.21)$$

Wetterich equation for fermion fields. In the case of fermionic fields $\psi, \bar{\psi}$ the propagator can schematically be written as

$$G_k = \begin{pmatrix} 0 & G_k^{\psi\bar{\psi}} \\ G_k^{\bar{\psi}\psi} & 0 \end{pmatrix}. \quad (4.22)$$

Permuting the fermionic indices introduces a minus sign so that $G_k^{\psi\bar{\psi}} = -G_k^{\bar{\psi}\psi}$. Similar considerations hold for the regulator matrix where we define regulators for $\psi\bar{\psi}$ and $\bar{\psi}\psi$. Performing the trace we end up with two identical contributions which gives a factor of 2 and from the super trace we receive a global minus sign. Assuming again locality of the regulator function we have

$$\partial_t \Gamma_k = - \int_{\star p} G_k^{\psi\bar{\psi}}(-p, p) \partial_t R_k^{\psi\bar{\psi}}(p). \quad (4.23)$$

Exactness. It is important to note that no truncations have been made during the derivation of the Wetterich equation which means that it is an exact equation. As discussed in section 2.2 the effective action encodes all information of a given theory. Solving the Wetterich equation therefore equates to the full solution a theory. However, since the Wetterich equation is a functional partial differential equation it is inherently an infinite tower of coupled differential equations which has to be truncated in some way for all but the most trivial cases. Truncations will of course spoil the exactness of the Wetterich equation but its non-perturbative origin allows for truncations that do not rely on a small coupling parameter and can therefore be applied to low energy QCD.

Trajectory in theory space. With the Wetterich equation a given theory is defined as an initial value problem. The initial value is the effective action at some UV cutoff Λ which can be interpreted as the *bare* theory consistent only of *bare*, microscopic interactions. Following the RG scale downwards to the IR we include continually more fluctuations, approaching the full theory with *dressed* couplings. We can view this flow from $k = \Lambda$ to $k = 0$ as a path in *theory space* which is the space of all possible operators invariant under the symmetry constraints of the theory. *Theory space* is generally infinitely dimensional and the role of truncations is to project the full theory space onto a finite dimensional subspace.

Regulator dependence. The trajectory of the flow in theory space is clearly regulator dependent, however without truncations all trajectories must arrive at the full effective action for $k \rightarrow 0$ as dictated by Eq. (4.1). A sketch of the trajectory in theory space is depicted in Fig. 4.2. When truncations are made the full effective action will generally deviate from the truncated effective action. The end point of the differential equation then becomes regulator dependent. This fact is often utilized in order to gauge the validity of a specific truncation.

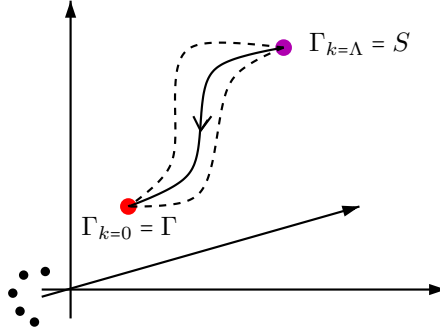


Figure 4.2: Schematic flow of the scale dependent effective action in theory space. Different regulator functions produce different paths in theory space but all end at the full effective action for $k \rightarrow 0$ [54].

One-loop nature. Since the flow of the effective action is given as a contraction of the propagator with the regulator $\partial_t R_k$ it can be represented as a one loop diagram

$$\partial_t \Gamma_k = \frac{1}{2} \text{ (one-loop diagram with a crossed dot) } . \quad (4.24)$$

This simple structure is somewhat deceiving and should not be confused with one loop diagrams in standard perturbation theory. The key difference is that the full scale dependent propagator enters in the Wetterich equation which includes all fluctuations in the limit $k \rightarrow 0$. We denote the full scale dependent propagator with a double line and the crossed dot symbolizes the regulator insertion $\partial_t R_k$. The one-loop structure is a result of ΔS_k being quadratic in the fields [53].

Flow equations for n -point functions. By differentiating the Wetterich equation with respect to the fields it is possible to obtain flow equations for arbitrary n -point functions

$$\partial_t \Gamma_k^{(n)} = \frac{\delta^n}{\delta \Phi_{a_1} \dots \delta \Phi_{a_n}} \frac{1}{2} \text{STr} (G_k \partial_t R_k) . \quad (4.25)$$

The derivative on the right hand side will generally introduce $n+1$ and $n+2$ point functions resulting in an infinite tower of coupled differential equations. In many cases one can perform projections that extract specific scale dependent couplings.

Truncations. As already mentioned the infinitely many interactions that are generated in the flow of the effective action have to be reduced to a manageable size. What truncation scheme is most suited depends on the physical system and what quantities are of interest. One possible truncation prescription is the so called vertex expansion of the effective action

$$\Gamma_k[\Phi] = \sum_{n=0}^{\infty} \frac{1}{n!} (\Gamma_k^{(n)})_{a_1 \dots a_n} \Phi^{a_1} \dots \Phi^{a_n} \quad (4.26)$$

which is an expansion in the n -point functions $\Gamma_k^{(n)}$. Another commonly used truncation scheme is the gradient expansion where all possible operators are ordered in their number of derivatives. For a bosonic field the expansion might read

$$\Gamma_k = \int_x \left[\mathcal{U}_k(\phi) + \frac{1}{2} Z_k(\phi) (\partial_\mu \phi)^2 + \mathcal{O}(\partial^4) \right]. \quad (4.27)$$

This expansion is applicable for relatively small momenta since $p_\mu = -i\partial_\mu$. The first term is the effective potential which as discussed in Sec. 2.3 already encodes a lot of information about for example the ground state of the system.

For this thesis we use this gradient expansion and we take into account only a minimal momentum dependence by setting $Z_k(\phi) = 1$ and neglecting all $\mathcal{O}(\partial^4)$ terms. All scale dependence is therefore encoded in the effective potential. This truncation is often referred to as the leading potential approximation (LPA) and it has proven to be surprisingly powerful despite its simplicity.

Five

The Chiral Phase Transition of QCD

We now apply the FRG framework introduced in the last section to study the chiral phase transition of QCD. To this end we first motivate what degrees of freedom are the most relevant for the phase transition and then construct the effective action accordingly. This defines our truncation and it is always the most crucial step in every FRG investigation. We then plug the truncated effective action into the Wetterich equation and derive a flow equation for the effective potential.

5.1 Effective Action for Low Energy QCD

Ideally we would start with an effective action that describes QCD in the perturbative regime and evolve it directly into the non-perturbative region. This is in principle possible but technically quite evolved. Here we restrict ourselves to a much lower initial scale of $\Lambda \approx 700 - 1000$ MeV. For relatively small temperatures and chemical potential this will include the most relevant degrees of freedom that drive the chiral transition.

First, let us consider the QCD action (3.10) which we identify with the effective action at the scale $k = \Lambda$

$$\Gamma_{\Lambda}^{\text{QCD}} \equiv S_{\text{QCD}}^{\text{gf}}[q, \bar{q}, c, \bar{c}, A_{\mu}] = \int_x \bar{q}(\not{D} + M_q)q + S_{\text{QCD}}^{\text{gauge}}[c, \bar{c}, A_{\mu}]. \quad (5.1)$$

We will not be focusing on the pure gauge part of the action and implicitly assume that its contribution has already been integrated out.

Using the Wetterich equation we attempt to integrate the QCD action minus the gauge contribution to the low energy regime. The flow $\partial_t \Gamma_{k=\Lambda}$ will immediately produce four-fermion interactions due to gluon exchange. For example the box diagrams depicted in Fig. 5.1 will be generated during the flow. Since such diagrams come with a factor of g_s^4 and g_s can not be considered small we write it explicitly into our action¹

$$S[q, \bar{q}] = \int_x \left(\bar{q}(\not{D} + M_q)q + \frac{1}{2} \lambda_q [(\bar{q}T^a q)^2 - (\bar{q}T^a \gamma_5 q)^2] \right) \quad (5.2)$$

where T^a are the usual generators of $U(N_f)$. From here on we will neglect further quark-gluon interactions and assume that the most important gluon fluctuations are encoded in the four-fermion vertex. Recent investigations suggest that this is not necessarily the case and further gluon fluctuations need to be incorporated to properly describe the quark dynamics [18].

¹This is also the action of the Nambu-Jona-Lasinio (NJL) model.

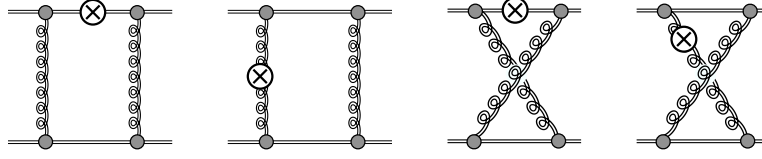


Figure 5.1: Box diagrams that produce a four-fermion vertex.

Furthermore, we have restricted ourselves to the scalar and pseudo scalar channels. More generally we would include a four-fermion vertex for each possible tensor structure

$$\sum_i \lambda_{k,i} (\bar{q} \mathcal{T}_i q)^2 \quad (5.3)$$

where \mathcal{T}_i are tensors with color-, flavor-, and Lorentz indices. The Lorentz part of \mathcal{T}_i is defined by the Clifford algebra in four space-time dimensions. It is generated by the 16 basis elements $\{\mathbb{1}, \gamma_\mu, \sigma_{\mu\nu}, \gamma_\mu \gamma_5, \gamma_5\}$. This means that we should also include vector- and axial-vector channels in our ansatz². However, for our application we suffice with the scalar and pseudo-scalar channels as defined in Eq. (5.2) since those are the dominant channels that drive spontaneous chiral symmetry breaking in the vacuum [55]. In fact, it has been shown that the vector mesons completely decouple from the flow in the vacuum due to their large mass [56].

Another subtlety known as *Fierz ambiguity* arises when considering the different four-fermion channels. It stems from the fact that an algebraic identity lets us convert the scalar, pseudo-scalar channel into the vector, axial-vector channel. For one quark flavor this identity reads

$$[(\bar{q}q)^2 - (\bar{q}\gamma_5 q)^2] = \frac{1}{2}[(\bar{q}\gamma_\mu \gamma_5 q)^2 - (\bar{q}\gamma_\mu q)^2]. \quad (5.4)$$

The different channels are therefore not independent and a direct identification with physical particles should be done with caution. A proper treatment of the four-fermion interaction would require a so called *Fierz complete basis*. The ambiguity can be related to a parameter γ . Mean field calculations of the four-fermion vertex have found to be strongly dependent on this non-physical parameter, however, in a similar FRG investigations this dependence has been found to be greatly reduced [57]. We therefore feel safe to neglect any issues that might arise through Fierz ambiguity and only include the scalar, pseudoscalar channel in our truncation.

Furthermore, we neglect any momentum dependence of the four-fermion coupling and only consider its RG scale dependence. This is often referred to as the point like approximation. We note here that a true study of bound states is only possible by calculating the momentum dependence since bound states manifest themselves as singularities in the four-fermion coupling at real momenta in Minkowski space. For our investigation the scalar condensate is of main interest, since it signals chiral symmetry breaking and it is already exactly determined at $p = 0$ which justifies the use of the point like approximation.

It turns out that the four-fermion vertex as defined in (5.2) is already sufficient to trigger spontaneous chiral symmetry breaking. This can be seen in the fix point structure of the beta function $\partial_t \lambda_q$: if g_s exceeds a critical coupling strength the four-fermion coupling diverges and a finite $\langle \bar{q}q \rangle$ is induced, see e.g. [17]. While it is possible to describe chiral symmetry breaking entirely in terms of fermions and gluons there is a more convenient way by expressing the four-fermion interaction in terms mesonic bound states. This fits nicely into the concept of RG since the degrees of freedom shift from quarks and gluons at high energies to mesons and baryons at small energies. We perform this shift in degrees of freedom by hand via an analytic transformation known as *Hubbard-Stratonovich transformation*.

²The tensor channel $(\bar{q}\sigma_{\mu\nu}q)^2$ is not invariant under $U(1)_A$ transformations.

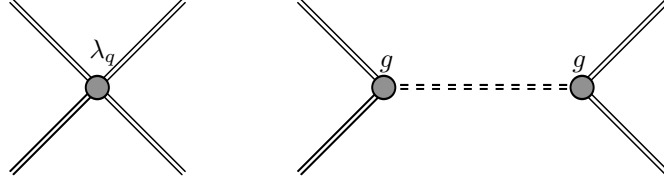


Figure 5.2: Diagrammatic representation of the four-fermion vertex before (left) and after (right) bosonization. In the bosonized formulation a four-fermion interaction is not directly included in the action but is possible via a mitigating meson (dashed line).

We begin by noting the identity

$$1 = \mathcal{N} \int \mathcal{D}\sigma_a \mathcal{D}\pi_a \exp \left[\int_x \left(\frac{m^2}{2} \sigma_a^2 + \frac{m^2}{2} \pi_a^2 \right) \right] \quad (5.5)$$

where the constant result of the Gaussian integrals is absorbed in \mathcal{N} . We combine this with the four-fermion part of the action in (5.2) and complete the square to get

$$\begin{aligned} & \exp \left[\int_x \frac{\lambda_q}{2} ((\bar{q} T^a q)^2 - (\bar{q} T^a \gamma_5 q)^2) \right] \\ &= \mathcal{N} \int \mathcal{D}\sigma_a \mathcal{D}\pi_a \exp \left[\int_x \left(\frac{\lambda_q}{2} (\bar{q} T^a q)^2 + \frac{m^2}{2} \sigma_a^2 + \frac{\lambda_q}{2} (i \bar{q} T^a \gamma_5 q)^2 + \frac{m^2}{2} \pi_a^2 \right) \right] \\ &= \mathcal{N} \int \mathcal{D}\sigma_a \mathcal{D}\pi_a \exp \left[\int_x \left(\frac{1}{2} (m \sigma_a - \sqrt{\lambda_q} \bar{q} T^a q)^2 + \sqrt{\lambda_q} m \bar{q} T^a \sigma_a q + \right. \right. \\ & \quad \left. \left. + \frac{1}{2} (m \pi_a - i \sqrt{\lambda_q} \bar{q} T^a \gamma_5 q)^2 + i \sqrt{\lambda_q} m \bar{q} T^a \pi_a \gamma_5 q \right) \right]. \end{aligned} \quad (5.6)$$

In the quadratic terms we perform a shift in the integration variables

$$\begin{aligned} \sigma_a &\longrightarrow \sigma_a - \frac{\sqrt{\lambda_q}}{m} \bar{q} T^a q \\ \pi_a &\longrightarrow \pi_a - i \frac{\sqrt{\lambda_q}}{m} \bar{q} T^a \gamma_5 q \end{aligned} \quad (5.7)$$

so that the total UV effective action now reads ³

$$S[q, \bar{q}, \sigma_a, \pi_a] = \Gamma_\Lambda = \int_x \left(\bar{q} (\not{D} + M_q + g T^a (\sigma_a + i \gamma_5 \pi_a)) q + \frac{m^2}{2} (\sigma_a^2 + \pi_a^2) \right) \quad (5.8)$$

where we have set

$$g^2 = \lambda_q m^2. \quad (5.9)$$

We have completely eliminated the four-fermion vertices in our action and in turn get a set of scalar σ_a and pseudo-scalar π_a mesons. The interaction between quarks and mesons are given by a Yukawa type vertex which allows for new four-fermion interactions (see Fig. 5.2). Crucially, box diagrams similar to Fig. 5.1, where the gluon line is now substituted by a meson line, arise in the flow. This means that the four-fermion vertex is re-generated by

³The constant value of the Gaussian integral has been dropped.

the Yukawa coupling so that the beta function for the four-fermion coupling does not vanish: $\partial_t \lambda_q \neq 0$. This is somewhat disheartening since our initial goal was it to express the four-fermion vertex entirely in terms of composite fields. It is expected that this re-emerging four-fermion interaction becomes relevant if the bosons are relatively light e.g. near a phase boundary [17]. Fortunately, it is possible to circumvent this problem by a technique called *re-bosonization*. Loosely speaking, the bosonization procedure for the constantly re-emerging four-fermion vertex is repeated at each RG step, see e.g. [54]. In fact, it is possible to resolve Fierz ambiguity using this technique. In practice, re-bosonization has been found to give a negligible correction in the spontaneously broken phase for a 2 flavor system in the vacuum [58]. We therefore suffice with the partially bosonized formulation in this thesis.

The meson fields obey the classical equations of motion

$$\begin{aligned}\frac{\delta S}{\delta \sigma_a} &= -g \bar{q} T^a q + m^2 \sigma_a = 0 \\ \frac{\delta S}{\delta \pi_a} &= -ig \bar{q} T^a \gamma_5 q + m^2 \pi_a = 0\end{aligned}\tag{5.10}$$

and therefore

$$\sigma_a = \frac{g}{m^2} \bar{q} T^a q, \quad \pi_a = \frac{ig}{m^2} \bar{q} T^a \gamma_5 q.\tag{5.11}$$

This formulation reveals that the meson fields created by the Hubbard-Stratonovich transformation are in fact quark bilinears. For vanishing quark current masses $M_q = 0$ we have seen that the QCD action is symmetric under a chiral $U(1)_V \otimes U(1)_A \otimes SU(N_f)_V \otimes SU(N_f)_A$ transformation and this directly translates to the bosonized version since we have not performed any symmetry violating steps during this short derivation. As discussed in Sec. 3.3 chiral symmetry on the action level may be broken in the ground state, indicated by a finite chiral condensate $\langle \bar{q} q \rangle$. With Eq. (5.11) we find that in the bosonized formulation spontaneous symmetry breaking is signaled by $\langle \sigma_a \rangle \equiv \bar{\sigma}_a > 0$.

From Eq. (5.8) we see that a finite $\langle g T^a \sigma_a \rangle$ acts as a mass term for the quark fields. We identify the total effective mass given as the sum of the current quark mass matrix M_q and the contribution from spontaneous chiral symmetry breaking as the *constituent mass* of the quark field.

Another nice aspect of the bosonized formulation is that Goldstone's theorem is directly manifest. We recall that λ_q diverges at the spontaneous symmetry breaking scale. For a constant Yukawa coupling this implies that $m = 0$ due to Eq. (5.9). This suggests that the auxiliary fields are massless if chiral symmetry is spontaneously broken. We will find later that the masses of the scalar fields σ_a receive contributions from higher couplings so that they are generally not massless except for special cases. The pseudoscalar fields π_a , however, remain massless in the spontaneously broken regime and we conclude that they must be the Goldstone bosons of broken $SU(N_f)_A$ or $U(N_f)_A$. This is of course only exactly true if the quark current masses M_q are zero. To study the effect of explicit symmetry breaking we bosonize the current quark mass term in Eq. (5.8)

$$\bar{q} M_q q \equiv c_a \sigma_a = c_a \frac{g}{m^2} \bar{q} T^a q.\tag{5.12}$$

Since the quark mass matrix is diagonal we only have N_f contributions on the right hand side of Eq. (5.12) corresponding to the diagonal generators of $U(N_f)$. With explicit breaking of $U(N_f)_L \otimes U(N_f)_R$ the Goldstone bosons acquire a finite mass and become pseudo Goldstone bosons.

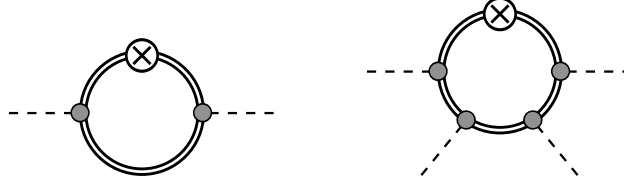


Figure 5.3: Meson propagator (left) and four meson vertex (right) generated in the flow of the bosonized action.

It is convenient to combine the $2N_f^2$ meson fields in a complex meson matrix of dimension $N_f \times N_f$

$$\phi \equiv T^a(\sigma_a + i\pi_a), \quad \phi_5 \equiv T^a(\sigma_a + i\gamma_5\pi_a) \quad (5.13)$$

where we have also defined a modified meson matrix ϕ_5 which enters in the Yukawa vertex and reflects the pseudo-scalar nature of the pion⁴. Both matrix fields transform under a chiral $U(N_f)_V \otimes U(N_f)_A$ as

$$\phi \rightarrow U_R \phi U_L^\dagger, \quad \phi_5 \rightarrow U_R \phi_5 U_L^\dagger. \quad (5.14)$$

The action (5.8) can be expressed in terms of the matrix fields by using $\text{Tr}(T^a T^b) = \delta^{ab}/2$ and therefore

$$\frac{1}{2} \sum_a (\sigma_a^2 + \pi_a^2) = \text{Tr}(\phi^\dagger \phi), \quad c_a \sigma_a = \text{Tr}[c_a T^a (\phi^\dagger + \phi)]. \quad (5.15)$$

The action of Eq. (5.8) now reads

$$S[\bar{q}, q, \sigma_a, \pi_a] = \int_x \{ \bar{q} (\not{\partial} + g\phi_5) q + m^2 \text{Tr}(\phi^\dagger \phi) + \text{Tr}[c_a T^a (\phi^\dagger + \phi)] \}. \quad (5.16)$$

Furthermore, we have to keep track of meson dynamics which are generated in the flow. For example the diagram depicted in the left panel of Fig. 5.3 acts as a meson propagator and we should therefore include a kinetic term for the mesons in our action

$$\frac{1}{2} ((\partial_\mu \sigma_a)^2 + (\partial_\mu \pi_a)^2) = \text{Tr}(\partial_\mu \phi^\dagger \partial_\mu \phi). \quad (5.17)$$

Also higher order meson vertices are generated during the flow (see right panel of Fig. 5.3), so that for example $(\text{Tr} \phi^\dagger \phi)^2$ should be captured in the flow of the effective action. This is, however, not the only possible meson vertex that respects chiral symmetry. We can construct in total N_f *chiral invariants*

$$\rho_n = \text{Tr}[(\phi^\dagger \phi)^n], \quad n = 1, \dots, N_f \quad (5.18)$$

and the flow of the corresponding vertices can conveniently be summed up in an effective potential which is a function of the chiral invariants

$$U_k(\rho_1, \dots, \rho_{N_f}). \quad (5.19)$$

⁴ ϕ_5 carries Lorentz indices whereas ϕ does not.

That the ρ_n are in fact invariant under a chiral transformation can easily be verified using Eq. (5.14)

$$\text{Tr}[(\phi^\dagger \phi)^n] \rightarrow \text{Tr}[(U_L \phi^\dagger U_R^\dagger U_R \phi U_L^\dagger)^n] = \text{Tr}[(\phi^\dagger \phi)^n]. \quad (5.20)$$

Finally, we add one further ingredient to our truncation which models the anomalous breaking of $U(1)_A$. We have discussed in Sec. 3.4 that the anomaly can be understood in terms of an instanton induced $2N_f$ quark interaction. Here we include a bosonized version the 't Hooft determinant in form of the lowest dimensional $U(1)_A$ violating term

$$\zeta \equiv \det(\phi^\dagger + \phi). \quad (5.21)$$

The same term with a relative minus sign is not included because it breaks CP invariance. Only $U(1)_A$ symmetry is explicitly broken by ζ and chiral $SU(N_f)_L \otimes SU(N_f)_R$ symmetry is not affected. We note here that a proper bosonization of the 't Hooft determinant within the path integral formalism introduces further corrections which we neglect here [50].

In the final effective action we introduce a quark chemical potential for each quark flavor by making the substitution $\phi \mathbb{1}_f \rightarrow \phi \mathbb{1}_f + \gamma_0 \mu$ where μ is a diagonal matrix in flavor space. Collecting all the above discussed contributions we end up with the following truncated effective action

$$\Gamma_\Lambda \equiv S[q, \bar{q}, \sigma_a, \pi_a] = \int_x \left\{ \bar{q} (\phi + \gamma_0 \mu + g \phi_5) q + \text{Tr}(\partial_\mu \phi^\dagger \partial_\mu \phi) + U_k(\rho_1, \dots, \rho_{N_f}) - c_A \zeta - \text{Tr}[c_a T^a (\phi^\dagger + \phi)] \right\}. \quad (5.22)$$

5.2 Deriving the Flow Equation

After having motivated all terms in our truncation we proceed by plugging this into the Wetterich equation. To this end we have to evaluate the matrix of second derivatives of the effective action. In this derivation we will refer to all meson fields as $\varphi_i(x)$ with $\varphi = (\sigma_0, \dots, \sigma_{N_f^2-1}, \pi_0, \dots, \pi_{N_f^2-1})$ the combination of the scalar and pseudo-scalar mesons. Furthermore, we have quark fields $q_\mu^{cf}(x)$ and antiquark fields $\bar{q}_\mu^{cf}(x)$ which carry Lorentz, flavor and color indices. This said we almost always suppress the color indices since no gluon fields are present in our truncation which couple to color charge.

We should also clarify the vacuum expectation value of the fields in our model since we have to project onto the vacuum after all derivatives have been calculated. The fermionic quark fields can not have a finite VEV due to required Lorentz invariance of the vacuum. Turning to the meson fields we note that only the diagonal, scalar components of the matrix field ϕ carry the quantum numbers of the vacuum and therefore can exhibit a finite expectation value. All other meson fields will be set to zero in the final flow equation.

With this we write the second derivative matrix generically as⁵

$$\Gamma^{(2)} = \begin{pmatrix} \Gamma^{\varphi\varphi} & \Gamma^{\varphi q} & \Gamma^{\varphi \bar{q}} \\ \Gamma^{q\varphi} & \Gamma^{qq} & \Gamma^{q\bar{q}} \\ \Gamma^{\bar{q}\varphi} & \Gamma^{\bar{q}q} & \Gamma^{\bar{q}\bar{q}} \end{pmatrix} = \begin{pmatrix} \Gamma^{\varphi\varphi} & 0 & 0 \\ 0 & 0 & \Gamma^{q\bar{q}} \\ 0 & \Gamma^{\bar{q}q} & 0 \end{pmatrix} \quad (5.23)$$

which is to be understood as evaluated at the VEV. There is no contribution with two quark or two antiquark fields in our truncation, since we fully bosonized the four-fermion vertex and therefore $\Gamma^{qq} = \Gamma^{\bar{q}\bar{q}} = 0$. Derivatives of the Yukawa vertex with respect to one meson field and one fermion field always leave another fermion field in our truncation and consequently those

⁵For clarity we suppress the k subscript of the effective action but k dependence is always implied.

contributions also vanish in the vacuum. Changing the order of differentiation with respect to the Grassmann valued quark fields gives a minus sign so that $\Gamma^{q\bar{q}} = -\Gamma^{\bar{q}q}$.

The next step would be to calculate the propagators which involves calculating the inverse of $\Gamma^{(2)} + R_k$. With Eq. (4.17) we generically write

$$G_k = \begin{pmatrix} (\Gamma^{\varphi\varphi} + R_k^{\varphi\varphi})^{-1} & 0 & 0 \\ 0 & 0 & -(\Gamma^{\bar{q}q} + R_k^{\bar{q}q})^{-1} \\ 0 & -(\Gamma^{q\bar{q}} + R_k^{q\bar{q}})^{-1} & 0 \end{pmatrix} \equiv \begin{pmatrix} G_k^{\varphi\varphi} & 0 & 0 \\ 0 & 0 & G_k^{q\bar{q}} \\ 0 & G_k^{\bar{q}q} & 0 \end{pmatrix} \quad (5.24)$$

where the minus signs in the first matrix arises in the contraction with the field metric, see relation (1.7). Noting that also $R_k^{q\bar{q}} = -R_k^{\bar{q}q}$ we write for the propagators

$$G_k^{\varphi\varphi} = (\Gamma_k^{\varphi\varphi} + R_k^{\varphi\varphi})^{-1}, \quad G^{q\bar{q}} = (\Gamma_k^{q\bar{q}} + R_k^{q\bar{q}})^{-1}. \quad (5.25)$$

The final step in the Wetterich equation is the contraction of all indices and integration over the loop momentum which can be done separately for the meson and quark contribution.

Meson contribution. We start the explicit calculation with the meson sector where we first have to take the second functional derivative of the effective action with respect to the meson fields. This gives

$$\begin{aligned} (\Gamma^{\phi\phi})_{ij}(x, y) &= \frac{\delta^2 \Gamma_k}{\delta \varphi_i(x) \delta \varphi_j(y)} \\ &= -\delta_{ij} \delta(x-y) \partial_\mu \partial_\mu + \int_z \frac{\delta^2}{\delta \varphi_i(x) \delta \varphi_j(y)} \tilde{U}_k(\rho_1(z), \dots, \rho_{N_f}(z), \zeta) \end{aligned} \quad (5.26)$$

where we have defined the combined meson potential

$$\tilde{U}_k(\rho_1, \dots, \rho_n, \zeta) \equiv U_k(\rho_1, \dots, \rho_n) - c_A \zeta - \text{Tr} [c_a T^a (\phi^\dagger + \phi)]. \quad (5.27)$$

The $SU(N_f)_V$ breaking term is only linear in the fields and will therefore vanish after differentiating twice. Since ζ is a determinant in flavor space it will depend on the number of quark flavors if c_A enters in the flow. For $N_f = 1$ it is linear in the fields and therefore will not contribute to $\Gamma^{(2)}$ and for $N_f = 2$ it behaves like a meson mass term. A more interesting case is $N_f = 3$ where it acts as a three meson vertex and has a non-constant contribution to $\Gamma^{(2)}$.

We hide in the notation above that the chiral invariants and ζ are functions of the meson fields i.e. $\rho_i(z) \equiv \rho_i(\varphi_1(z), \dots, \varphi_{2N_f}(z))$. Apart from the usual kinetic term we have to perform all second derivatives of the effective potential by applying the chain rule.

With the notation $\tilde{U}_k(z) \equiv \tilde{U}_k(\rho_1(z), \dots, \rho_{N_f}(z), \zeta(z))$ we can write the second derivatives of the effective potential as

$$\begin{aligned} \int_z \frac{\delta \tilde{U}_k(z)}{\delta \varphi_i(x)} &= \int_z \int_y \left[\sum_{j=1}^{N_f} \frac{\delta \rho_j(y)}{\delta \varphi_i(x)} \frac{\delta \tilde{U}_k(z)}{\delta \rho_j(y)} + \frac{\delta \zeta(y)}{\delta \varphi_i(x)} \frac{\delta \tilde{U}_k(z)}{\delta \zeta(y)} \right] \\ &= \sum_{j=1}^{N_f} \frac{\partial \rho_j}{\partial \varphi_i} \frac{\partial \tilde{U}_k}{\partial \rho_j} + \frac{\partial \zeta}{\partial \varphi_i} \frac{\partial \tilde{U}_k}{\partial \zeta}. \end{aligned} \quad (5.28)$$

The integrals cancel because of delta distributions that arise in the functional differentiation

$$\frac{\delta \varphi_j(y)}{\delta \varphi_i(x)} = \delta_{ij} \delta(x-y), \quad \frac{\delta \tilde{U}_k(z)}{\delta \rho_j(y)} = \frac{\partial \tilde{U}_k}{\partial \rho_j} \delta(y-z). \quad (5.29)$$

The second derivative is evaluated in the same manner and gives a global $\delta(x-y)$ factor. The explicit expressions for the derivatives of the higher chiral invariants are lengthy due to their non trivial dependence of the meson fields. For now we simply write

$$\int_z \frac{\delta^2 \tilde{U}_k(z)}{\delta \varphi_i(x) \delta \varphi_j(y)} \equiv \delta(x-y) (M_{k,\varphi(x)}^2)_{ij} \quad (5.30)$$

where $M_{k,\varphi}^2$ is the Hessian matrix consistent of all second derivatives of \tilde{U}_k with respect to the fields. Note that these are ordinary partial derivatives since the functional part has already been taken care of. After all derivatives have been calculated we replace fields with their VEVs which generally leads to large cancellations in $M_{k,\varphi}^2$.

Going into momentum space and adding the optimized Litim regulator in three dimensions

$$R_k^{\varphi\varphi}(\mathbf{p}, \mathbf{q}) = (k^2 - \mathbf{p}^2) \theta(k^2 - \mathbf{p}^2) \delta(\mathbf{p}, \mathbf{q}) (2\pi)^3 \quad (5.31)$$

we get

$$G_k^{\varphi\varphi}(\mathbf{p}, \mathbf{q}) = (2\pi)^{-4} \delta(\mathbf{p} + \mathbf{q}) [\mathbb{1} p^2 + M_{k,\varphi}^2 + \mathbb{1} (k^2 - \mathbf{p}^2) \theta(k^2 - \mathbf{p}^2)]^{-1} \quad (5.32)$$

where $\mathbb{1}$ denotes the $2N_f^2 \times 2N_f^2$ dimensional unit matrix.

At this point we make the finite temperature substitution $p = (\omega_n, \mathbf{p})$ so that $p^2 = \omega_n^2 + \mathbf{p}^2$

$$\begin{aligned} G_k^{\varphi\varphi}(\mathbf{p}, \mathbf{q}) &= (2\pi)^{-3} \delta(\mathbf{p} + \mathbf{q}) \delta_{\omega_n \omega_m} [\mathbb{1} \omega_n^2 + \mathbb{1} \mathbf{p}^2 + M_{k,\varphi}^2 + \mathbb{1} (k^2 - \mathbf{p}^2) \theta(k^2 - \mathbf{p}^2)]^{-1} \\ &= (2\pi)^{-3} \delta(\mathbf{p} + \mathbf{q}) \delta_{\omega_n \omega_m} \left[\frac{\theta(k^2 - \mathbf{p}^2)}{\mathbb{1}(\omega_n^2 + k^2) + M_{k,\varphi}^2} + \frac{\theta(\mathbf{p}^2 - k^2)}{\mathbb{1}(\omega_n^2 + \mathbf{p}^2) + M_{k,\varphi}^2} \right] \end{aligned} \quad (5.33)$$

where $q_0 = \omega_m$. Ignoring the second term in the parentheses this has the familiar structure of a propagator for particles with energy $\omega_n^2 + k^2$ and mass $(M_{k,\varphi}^2)_{ii}$. This identification should, however, not be made too hastily, because $M_{k,\varphi}^2$ is not necessarily diagonal yet. We get the meson masses by diagonalizing the second derivative matrix

$$U^\dagger M_{k,\varphi}^2 U \equiv \mathcal{M}_{k,\varphi}^2 = \text{diag}(m_{k,\pi^0}^2, m_{k,\pi^+}^2, m_{k,\pi^-}^2, m_{k,\sigma}^2, \dots). \quad (5.34)$$

These are so called curvature masses and they are itself not physical quantities. However, an investigation within a 2 flavor quark-meson model including a fully momentum dependent propagator has revealed the difference between curvature masses and experimentally measurable pole masses to be relatively small [59].

We furthermore define the diagonalized propagator

$$U^\dagger G_k^{\varphi\varphi} U = \mathcal{G}_k^{\varphi\varphi} = \text{diag}(G_k^{\pi^0 \pi^0}, G_k^{\pi^+ \pi^+}, G_k^{\pi^- \pi^-}, G_k^{\sigma \sigma}, \dots). \quad (5.35)$$

which consists of individual propagators for the physical mesons in our truncation. Note that this rotation does not alter the final flow equation since we can absorb it in the trace $\text{Tr}(U^\dagger G_k U \cdot \partial_t R_k) = \text{Tr}(G_k \cdot \partial_t R_k)$ because $R_k \sim \mathbb{1}$ in meson field space.

Finally, we contract the diagonal propagator with $\partial_t R_k^{\varphi\varphi}$ and perform the trace. First let us explicitly write out the momentum dependence of the contraction

$$\begin{aligned} (\mathcal{G}_k^{\varphi\varphi} \partial_t R_k^{\varphi\varphi})(\mathbf{p}, \mathbf{q}) &= \int_{\mathbf{p}'} \mathcal{G}_k^{\varphi\varphi}(\mathbf{p}, \mathbf{p}') \cdot \partial_t R_k^{\varphi\varphi}(\mathbf{p}', \mathbf{q}) (2\pi) \delta_{p'_0 q_0} \\ &\equiv \int_{\mathbf{p}'} \mathcal{G}_k^{\varphi\varphi}(\mathbf{p}) \delta(\mathbf{p} + \mathbf{p}') \cdot \partial_t R_k^{\varphi\varphi}(\mathbf{q}) (2\pi)^4 \delta(\mathbf{p}' + \mathbf{q}) \\ &= \mathcal{G}_k^{\varphi\varphi}(\mathbf{p}) \cdot \partial_t R_k^{\varphi\varphi}(\mathbf{q}) (2\pi)^4 \delta(\mathbf{p} - \mathbf{q}). \end{aligned} \quad (5.36)$$

The super trace in the Wetterich equation also acts on momentum space so that only the momentum-diagonal components of $\mathcal{G}_k \partial_t R_k$ survive. We therefore set $p = q$ and get a factor of $(2\pi)^4 \delta(0) = V$ which is just the four dimensional volume of the system. Plugging this into the Wetterich equation we get

$$\partial_t \Gamma_k^{\varphi\varphi} = \frac{1}{2} \text{Tr}(\mathcal{G}_k^{\varphi\varphi} \cdot \partial_t R_k^{\varphi\varphi}) = V \frac{1}{2} \sum_{i=1}^{2N_f^2} \int_{\star p} (\mathcal{G}_k^{\varphi\varphi}(p))_{ii} \partial_t R_k^{\varphi\varphi}(\mathbf{p}) \quad (5.37)$$

where only the momentum integral is left to be evaluated. Evaluating the scale derivative of the regulator function we find

$$\partial_t R_k^{\varphi\varphi}(\mathbf{p}) = 2k^2 \theta(k^2 - \mathbf{p}^2). \quad (5.38)$$

Taking the derivative of the Heaviside step function introduces a term of the form $x\delta(x)$ which we can omit because it always vanishes in an integral. The meson propagator from Eq. (5.33) has two contributions where one is proportional to $\theta(1 - k^2/\mathbf{p}^2)$ and the other to $\theta(k^2/\mathbf{p}^2 - 1)$. Multiplying the propagator with $\partial_t R_k^{\varphi\varphi}(\mathbf{p})$ only the first term survives because $\theta(k^2/\mathbf{p}^2 - 1)\theta(1 - k^2/\mathbf{p}^2) = 0$. The momentum integration can be trivially performed

$$\begin{aligned} \int_{\star p} (\mathcal{G}_k^{\varphi\varphi}(p))_{ii} \partial_t R_k^{\varphi\varphi} &= \frac{T}{2} \sum_{n=-\infty}^{\infty} \int \frac{d^3 p}{(2\pi)^3} \frac{2k^2 \theta(k^2 - \mathbf{p}^2)}{\omega_n^2 + k^2 + m_{k,i}^2} \\ &= \frac{T}{6\pi^2} \sum_{n=-\infty}^{\infty} \frac{k^5}{\omega_n^2 + k^2 + m_{k,i}^2}. \end{aligned} \quad (5.39)$$

For the remaining sum over Matsubara frequencies we use the relation

$$\coth(x) = \sum_{n=-\infty}^{\infty} \frac{x}{(\pi n)^2 + x^2} \quad (5.40)$$

and substitute ω_n with the bosonic Matsubara frequencies $\omega_n = 2\pi T n$. Plugging the result into Eq. (5.37) we arrive at the final flow equation for the meson part of our truncation

$$\partial_t \Gamma_k^{\varphi\varphi} = \frac{V k^5}{12\pi^2} \sum_{i=1}^{2N_f^2} \frac{1}{E_i} \coth\left(\frac{E_i}{2T}\right), \quad (5.41)$$

with the meson energies given by $E_i = \sqrt{k^2 + m_{k,i}^2}$.

Quark Contribution. For the quark contribution the general procedure is exactly the same and here we only review some important steps. The second derivative of the effective action in coordinate space is given by

$$(\Gamma_k^{q\bar{q}})^{ff'}_{\mu\nu}(x, y) = \frac{\delta^2 \Gamma_k}{\delta q_\mu^{f'}(y) \delta \bar{q}_\mu^f(x)} = \left(\not{D}_{\mu\nu} \delta^{ff'} + \gamma_0 \mu_\nu \mu_f \delta^{ff'} + g \phi_5^{ff'} \right) \delta(x - y). \quad (5.42)$$

We switch to momentum space and add the optimized fermion regulator in three dimensions

$$R_k^{q\bar{q}}(\mathbf{p}, \mathbf{q}) = i(\boldsymbol{\gamma} \cdot \mathbf{p}) r_k(\mathbf{p}) \delta(\mathbf{q} + \mathbf{p}) (2\pi)^3, \quad r_k(\mathbf{p}^2) = \left(\frac{k}{\sqrt{\mathbf{p}^2}} - 1 \right) \theta(k^2 - \mathbf{p}^2). \quad (5.43)$$

which inverted leads to the propagator

$$(G_k^{q\bar{q}})^{ff'}(p, q) = \frac{-\gamma_0(i\omega_n + \mu_f) - i(\boldsymbol{\gamma} \cdot \mathbf{p})(1 + r_k(\mathbf{p}^2)) + g\phi_5^{\dagger ff}}{(i\omega_n + \mu_f)^2 + \mathbf{p}^2(1 + r_k(\mathbf{p}^2))^2 + m_{q,f}^2} (2\pi)^{-4} \delta(p + q) \delta^{ff'} \quad (5.44)$$

where we have used the following abbreviation for the squared quark mass matrix

$$m_{q,f}^2 = g^2 \phi_5^{ff} \phi_5^{\dagger ff}. \quad (5.45)$$

Since we evaluate the propagator at the VEVs it is clear that m_q^2 is diagonal and we can define separate propagators for each quark flavor.

Finally we contract with $\partial_t R_k^{q\bar{q}}$ and perform the trace. Only the term proportional to $\boldsymbol{\gamma} \cdot \mathbf{p}$ survives the Dirac trace and color trace gives the usual factor of N_c . After the trivial momentum integration we perform the Matsubara sum analytically to arrive at

$$\partial_t \Gamma_k^{q\bar{q}} = -\frac{N_c V k^5}{6\pi^2} \sum_{f=1}^{N_f} \left(\tanh\left(\frac{E_{q,f} + \mu_f}{2T}\right) + \tanh\left(\frac{E_{q,f} - \mu_f}{2T}\right) \right) \quad (5.46)$$

where we have defined the scale dependent quark energy $E_{q,f} = \sqrt{k^2 + m_{q,f}^2}$.

Flow Equation For The Effective Potential. The flow of the effective action is still a complicated functional differential equation because the fields $\varphi_i(x)$ depend on space time. In order to extract the *ordinary* partial differential equation for the effective potential we set the fields constant as suggested in Sec. 2.3. Dividing by the four dimensional volume factor V we end up with the flow equation for the effective potential

$$\partial_t \mathcal{U}_k = \frac{k^5}{12\pi^2} \left[\sum_{i=1}^{2N_f^2} \frac{1}{E_i} \coth\left(\frac{E_i}{2T}\right) - 2N_c \sum_{f=1}^{N_f} \left(\tanh\left(\frac{E_{q,f} + \mu_f}{2T}\right) + \tanh\left(\frac{E_{q,f} - \mu_f}{2T}\right) \right) \right]. \quad (5.47)$$

5.3 Flow Equation for 2+1 Flavor

So far we have formulated the flow equation for the general case of $U(N_f)_L \otimes U(N_f)_R$ symmetry. We now specify the discussion to the 2+1 flavor configuration which will be the main topic of this thesis.

Approximate $U(3)_L \otimes U(3)_R$ symmetry gives rise to a scalar and pseudoscalar nonet (see Sec. 3.3). The pseudoscalar and scalar part of the meson field matrix $\phi = T^a(\sigma_a + i\pi_a)$ can be expanded as

$$\begin{aligned} T^a \pi_a &= \frac{1}{\sqrt{2}} \begin{pmatrix} \frac{\pi^0}{\sqrt{2}} + \frac{\pi_0}{\sqrt{3}} + \frac{\pi_8}{\sqrt{6}} & \pi^- & K^- \\ \pi^+ & -\frac{\pi^0}{\sqrt{2}} + \frac{\pi_0}{\sqrt{3}} + \frac{\pi_8}{\sqrt{6}} & \bar{K}^0 \\ K^+ & \bar{K}^0 & \frac{\pi_0}{\sqrt{3}} - \frac{2\pi_8}{\sqrt{3}} \end{pmatrix} \\ T^a \sigma_a &= \frac{1}{\sqrt{2}} \begin{pmatrix} \frac{a_0^0}{\sqrt{2}} + \frac{\sigma_0}{\sqrt{3}} + \frac{\sigma_8}{\sqrt{6}} & a_0^- & \kappa^- \\ a_0^+ & -\frac{a_0^0}{\sqrt{2}} + \frac{\sigma_0}{\sqrt{3}} + \frac{\sigma_8}{\sqrt{6}} & \bar{\kappa}^0 \\ \kappa^+ & \kappa^0 & \frac{\sigma_0}{\sqrt{3}} - \frac{2\sigma_8}{\sqrt{3}} \end{pmatrix} \end{aligned} \quad (5.48)$$

where T^a for $a = 0, \dots, 8$ are the generators of $U(3)$ given by the Gell-Mann matrices completed with $\sqrt{2/3} \mathbf{1}$. Some identifications with experimentally known particles have already been performed: The pion triplet is given by

$$\pi^0 = \pi_3, \quad \pi^\pm = \frac{1}{\sqrt{2}}(\pi_1 \pm i\pi_2) \quad (5.49)$$

and the two kaon doublets

$$K^\pm = \frac{1}{\sqrt{2}}(\pi_4 \pm i\pi_5), \quad K^0 = \frac{1}{\sqrt{2}}(\pi_6 + i\pi_7), \quad \bar{K}^0 = \frac{1}{\sqrt{2}}(\pi_6 - i\pi_7). \quad (5.50)$$

Similar relations hold for the scalar particles.

We have already established that only the diagonal entries in $T^a \sigma_a$ can have finite expectation values which are in the case of $N_f = 3$ the fields σ_0, σ_3 and σ_8 . From Eq. (5.48) with $a_0^0 = \sigma_3$ we can read off that a finite $\langle \sigma_0 \rangle \equiv \bar{\sigma}_0$ does not break $SU(3)_V$ symmetry. However, if $\bar{\sigma}_8 > 0$ the $SU(3)_V$ symmetry is broken down to $SU(2)_V$ i.e. we see a difference in the strange- and up, down condensates. If furthermore $\bar{\sigma}_3$ is finite, isospin symmetry is completely broken and there is a difference in the up and down quark condensates.

From now on we will simplify our calculations by assuming exact $SU(2)_V$ symmetry, i.e. $\bar{\sigma}_3 = 0$. This is a good approximation, since the experimentally measured quark masses are very similar for up and down quarks, whereas the strange quark is heavier than both light quarks by a factor of ~ 20 . We refer to this as the 2+1 flavor configuration.

It is convenient to separate light and strange part of σ_0 and σ_8 which can be done with the rotation

$$\begin{pmatrix} \sigma_l \\ \sigma_s \end{pmatrix} = \frac{1}{\sqrt{3}} \begin{pmatrix} \sqrt{2} & 1 \\ 1 & -\sqrt{2} \end{pmatrix} \begin{pmatrix} \sigma_0 \\ \sigma_8 \end{pmatrix}. \quad (5.51)$$

Using this substitution the vacuum expectation value of the meson field matrix now reads

$$\langle \phi \rangle = \frac{1}{2} \text{diag} \begin{pmatrix} \bar{\sigma}_l \\ \bar{\sigma}_l \\ \sqrt{2}\bar{\sigma}_s \end{pmatrix}. \quad (5.52)$$

With $\bar{\sigma}_3 = 0$ the explicit symmetry breaking parameter c_3 must also vanish and we express the two non-vanishing parameters c_0 and c_8 in the nonstrange-strange basis. The explicit symmetry breaking term in the meson potential now reads

$$-c_l \sigma_l - c_s \sigma_s \quad (5.53)$$

where $SU(2)_V$ symmetry is apparent.

For $N_f = 3$ we have 3 independent chiral invariants, however, in our calculations we will neglect the effect of the third chiral invariant ρ_3 for simplicity. This means that the meson potential is a function of ρ_1, ρ_2 and ζ . The undiagonalized mass matrix from Eq. (5.30) is then given by

$$(M_{k,\varphi}^2)_{ij} = \frac{\partial^2}{\partial \varphi_j \partial \varphi_i} \tilde{U}_k(\rho_1, \rho_2, \zeta) = \frac{\partial^2}{\partial \varphi_j \partial \varphi_i} (U_k(\rho_1, \rho_2) - c_A \zeta) \quad (5.54)$$

where we specify $\varphi = (\sigma_l, \sigma_1, \dots, \sigma_7, \sigma_s, \pi_0, \dots, \pi_8)$. After explicitly performing the differentiation we set the fields to their VEVs and find that large parts of the mass matrix vanish. The general structure of the mass matrix can be schematically written as

$$M_{k,\varphi}^2 \sim \begin{pmatrix} \sigma_{ll} & & & \sigma_{sl} & & & \\ & \mathbf{a_0} & & & & 0 & \\ & & \kappa & & & & \\ \sigma_{ls} & & & \sigma_{ss} & & & \\ & 0 & & & \pi_{00} & & \pi_{80} \\ & & & & \boldsymbol{\pi} & & \\ & & & & & K & \\ & & & & \pi_{08} & & \pi_{88} \end{pmatrix}. \quad (5.55)$$

In this compressed notation we indicate that due to $SU(2)_V$ symmetry some meson masses degenerate. For example the $\boldsymbol{\pi}$ triplet has three identical entries in the mass matrix and the same is true for the $\mathbf{a_0}$ triplet. Furthermore, the two kaon doublets degenerate and so do the κ mesons. As discussed in section 5.2 we get the meson masses by diagonalizing $M_{k,\varphi}^2$. In our case we only have non-diagonal components in the nonstrange-strange or 0-8 sector. This can be easily diagonalized by two separate 2×2 rotations respectively acting on the scalar and pseudoscalar part of the mass matrix. In terms of physical particles this is observed as mixing of the pseudoscalar η' and η mesons and the scalar σ and f_0 mesons. The mesons η and η' are therefore mixtures of a singlet and octet state. Similarly σ and f_0 have strange and non-strange components. For ideal flavor mixing the off-diagonal entries in the mass matrix vanish and η' becomes a pure singlet state and σ is non-strange. The explicit expressions for all non-vanishing entries of $M_{k,\varphi}^2$ and definitions for the scalar and pseudoscalar mixing angle are listed in appendix B.1.

The quark masses are much simpler in structure. Evaluating Eq. (5.45) at the vacuum expectation value we find in the nonstrange-strange basis

$$m_l = g \frac{\sigma_l}{2}, \quad m_s = g \frac{\sigma_s}{\sqrt{2}}. \quad (5.56)$$

Finally, we mention two important PCAC relations for the 2+1 flavor quark-meson model. They relate the decay constants of the (pseudo) Goldstone bosons to the light and strange condensate. Such relations can generally be derived as shown in [60] and in our case they read

$$f_\pi = \bar{\sigma}_l, \quad f_K = \frac{\bar{\sigma}_l}{2} + \frac{\bar{\sigma}_s}{\sqrt{2}}. \quad (5.57)$$

For the numerical calculations we use experimental values for f_π and f_K to fix the condensates to the values $\bar{\sigma}_l = 92.4$ MeV and $\bar{\sigma}_s = 94.5$ MeV in the vacuum. Further details on the parameter fixing procedure are summarized in appendix C.

5.4 Flow Equation for the $SU(2)_L \otimes SU(2)_R$ Model

We now consider the following important limit of the 2+1 flavor system: If we assume the strange quark to be infinitely heavy⁶ they will completely decouple from the flow and we have effectively only the two light quarks i.e. approximate $U(2)_L \otimes U(2)_R$ symmetry. It is possible to investigate the axial anomaly also in this approximation. For $N_f = 2$ the 't Hooft determinant acts as a mass term since it is quadratic in the fields. The $U(2)_L \otimes U(2)_R$ symmetric quark-meson model has been investigated in a FRG treatment for example in [61]. Here we will consider axial symmetry to be completely broken. If we perform the limit $c_A \rightarrow \infty$ the chiral partners a_0 and η' become infinitely heavy and therefore decouple from the flow. We are left with approximate $U(2)_V \otimes SU(2)_A \simeq U(1)_V \otimes SU(2)_L \otimes SU(2)_R$ symmetry which is often

⁶We also assume charm, top and bottom quarks to be infinitely heavy.

referred to as the $SU(2) \otimes SU(2)$ quark-meson model since the baryon number of $U(1)_V$ is trivially conserved.

In the $SU(2) \otimes SU(2)$ model isospin symmetry is automatically conserved since only one scalar condensate exists—the sigma meson. The other remaining mesons are given by the pseudoscalar pion triplet. The LPA effective action at the UV scale can be written as

$$\Gamma_{k=\Lambda} = \int_x \left\{ \bar{q}_2 \left(\not{\partial} + g(\sigma + i\gamma_5 \boldsymbol{\tau} \cdot \boldsymbol{\pi}) \right) q_2 + \frac{1}{2}(\partial_\mu \sigma)^2 + \frac{1}{2}(\partial_\mu \boldsymbol{\pi})^2 + U(\rho) - c\sigma \right\} \quad (5.58)$$

where $\boldsymbol{\tau}$ are generators of $SU(2)$ given by the three Pauli matrices. We define the 2 flavor quark field as $q_2(x) = (u(x), d(x))^T$. There is only one chiral invariant $\rho = \sigma^2 + \boldsymbol{\pi}^2$ if axial symmetry is broken and the meson potential can therefore be written as a function of ρ . This simplifies the meson masses significantly since only derivatives with respect to one chiral invariant occur. We find for the quark and meson masses

$$m_\sigma^2 = 2U'_k + 4\rho U''_k, \quad m_\pi^2 = 2U'_k, \quad m_q^2 = g^2 \rho. \quad (5.59)$$

Six

Numerical Results

In this section we collect and discuss the results of extensive numerical calculations of the previously discussed flow equations. We solved the 2+1 flavor and 2 flavor FRG flow equations (see Eq. (5.47) with masses as discussed in Sec. 5.3 and 5.4) as well as the 2+1 flavor system in standard mean field approximation (MFA). The derivation of the effective potential in MFA is outlined in appendix A. We compare the FRG results to corresponding mean fields calculations in order to gauge the importance of meson fluctuations on the chiral phase transition. This is not strictly true since we also neglect the divergent vacuum energy in the standard mean field approximation. It is possible to include the vacuum energy for example by dimensional regularization [62] which is then equivalent to FRG calculations without the meson loop.

The flow equations for the effective potential are highly non-linear, stiff partial differential equations and therefore constitute a significant numerical challenge. Several methods have been successfully used to find solutions to such flow equation which all have their strengths and weaknesses. We discuss some of those methods in Sec. 7 and there we also describe in detail the specific implementation used during this work. For $N_f = 2$ we use a novel approach to solve flow equations which combines strengths of various other methods. We discuss this thoroughly in Sec. 7.2. Parameter fixing is done in the vacuum so that experimentally measured pion and kaon decay constants are recovered and a range of meson masses. Furthermore, we neglect any T and μ dependence of the parameters. Details on the parameter fixing and start potential for the flow equations can be found in appendix C. All results shown here will be for the 2+1 flavor system unless stated otherwise.

We structure the discussion of our results as follows: First we investigate the finite temperature behavior at vanishing chemical potential where we discuss the condensates, meson spectrum and pressure density. At finite chemical potential we reveal the full phase structure of the chiral quark meson truncation and also investigate effects of unsymmetrical quark matter. Finally we investigate the order of the chiral phase transition in dependence of pion and kaon mass which can be considered the main result of this work.

6.1 Finite Temperature

We start our discussion at vanishing chemical potential and finite temperature. Since the sigma meson is experimentally only known as a very broad resonance we vary the sigma mass in our calculations to gauge its effect on the chiral phase transition. Fig. 6.1 shows the light and strange condensate for three different sigma masses including the $U(1)_A$ breaking determinant. In agreement with Lattice simulations and e.g. calculations using Dyson Schwinger equation [63] we find the chiral transition to be a smooth crossover at vanishing chemical potential. We use the inflection point in the light condensate as definition for the critical temperature which gives $T_c = 139.7, 156.0, 175.1$ MeV corresponding to the sigma masses $m_\sigma = 400, 480, 560$ MeV. Lattice calculations agree on a pseudo critical temperature of $T_c \sim 150$ MeV [64] which suggests that our range of sigma masses is reasonable.

We find that $\bar{\sigma}_l$ falls off faster than $\bar{\sigma}_s$ with increasing temperature indicating that $SU(2)_L \otimes SU(2)_R$ is restored first. Only at very high temperatures, not accessible within our truncation,

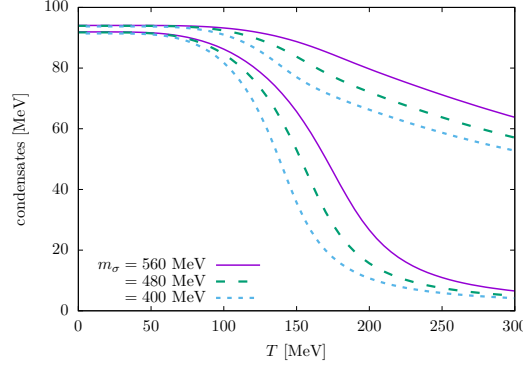


Figure 6.1: Light (lower lines) and strange (upper lines) condensate in dependence of temperature with $U(1)_A$ anomaly and for three different sigma masses. With smaller sigma masses the drop of the light condensate becomes steeper.

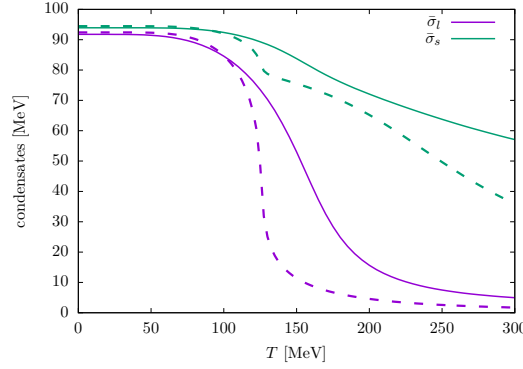


Figure 6.2: Temperature dependence of the light and strange condensate with $U(1)_A$ anomaly for $m_\sigma = 480$ MeV. Solid lines are FRG calculations and dashed lines are analogous calculations in mean field approximation.

$\bar{\sigma}_s$ also approximately vanishes and full chiral $SU(3)_L \otimes SU(3)_R$ symmetry is restored. This can be understood as a consequence of the higher mass of strange quarks which acts against chiral symmetry restoration. Additionally, we see that lighter sigma masses increase the steepness of the chiral transition and consequently decrease the critical temperature.

We compare the FRG results to corresponding calculations in mean field approximation in Fig. 6.2 where we have chosen the sigma mass $m_\sigma = 480$ MeV. Similar to 2 flavor MFA calculations (see e.g. [21]) we find a steep drop in the light condensate and therefore a significantly lower critical temperature. Furthermore, we see a steep but small drop in the strange condensate near T_c and generally a faster decline at high temperatures compared to FRG results. In mean field approximation we also find an increasingly steeper chiral transition with decreasing sigma mass and for $m_\sigma \lesssim 350$ MeV the chiral transition is of first-order even at $\mu = 0$. We conclude that fluctuations wash out the chiral phase transition i.e. move further away from a first-order phase transition.

Using two different parameter sets, where one includes the 't Hooft determinant term and one omits it, we can see the effect of the axial anomaly on the condensates. The solid lines in Fig. 6.3 denote the light and strange condensate calculated with the anomaly and dashed lines were calculated without the anomaly. Both parameter sets were fitted to give identical sigma masses in the vacuum $m_\sigma \sim 480$ MeV. We find that the anomaly only marginally affects the light condensate. It pushes the chiral transition to a slightly higher temperature and the drop in the light condensate is less steep. In the strange condensate we find an obverse effect: It

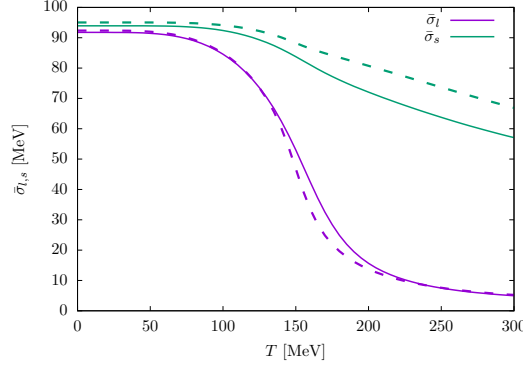


Figure 6.3: Temperature dependence of the light and strange condensate with- (solid lines) and without (dashed lines) $U(1)_A$ anomaly for $m_\sigma = 480$ MeV.

vanishes more rapidly at high temperatures if the anomaly is included which means that the anomaly works in favor of chiral $SU(3)_L \otimes SU(3)_R$ restoration. This could, however, be an artifact of not properly fitted start parameters since both condensates do not perfectly agree at $T = 0$.

6.2 The Scalar-Pseudoscalar Meson Spectrum

The temperature dependence of the scalar and pseudoscalar meson masses in MFA and FRG are compared in Fig. 6.4. Because only the masses of the pseudoscalar nonet and the sigma mass were used in the fitting procedure all other scalar meson masses are predictions. The scalar a_0 triplet in our calculation is 5% heavier than the experimentally measured $a_0(980)$. For the other scalar particles the identification with measured particles becomes less clear: The κ mesons are experimentally very broad resonances and the f_0 meson can be identified with either the $f_0(980)$ or $f_0(1370)$ particle. In our calculations the mass of the f_0 meson is special in a sense that it is the only mass where the predictions of FRG and MFA differ in the vacuum. In MFA the f_0 mass is 5% higher than the FRG result of 1155 MeV. However, since both the FRG and MFA f_0 masses lie somewhere between the two experimentally measured masses a clear identification can not be made.

At finite temperature we see the restoration of chiral symmetry realized in the degeneration of meson masses. This can be observed for the chiral partners π and σ as well as a_0 and η' . They start to degenerate at temperatures above the pseudo critical temperature $T_c \sim 150$ MeV and are approximately degenerate at $T \sim 250$ MeV. This is a result of $SU(2) \otimes SU(2)$ restoration which, as discussed in the last section, is linked to the melting light condensate around the pseudo critical temperature. The mass gap between π, σ and a_0, η' is generated by an opposite sign of the anomaly term $m_{a_0/\pi}^2 \sim \pm c_A \sigma_s$ (see Appendix B.1). In agreement with experimental observations we find a drop of the η' meson mass around the critical temperature [65, 66]. This has also been observed in FRG treatment of the $U(2)_L \otimes U(2)_R$ quark-meson model with a temperature dependent 't Hooft determinant term [61].

In mean field approximation we see qualitatively the same symmetry breaking features as in the FRG calculation. However, the degeneration of the chiral partners sets in earlier and is less smooth compared to the FRG calculation. This is in agreement with the earlier observation that the light condensate falls off steeper and at lower temperatures in MFA and a similar behavior has been found in two flavor calculations [67]. At large temperatures the chiral partners are degenerate in both the FRG and MFA calculations. There is, however, a growing gap between FRG and MFA masses at larger temperatures. Furthermore, we find a smaller mass gap between π, σ and a_0, η' at high temperatures in the MFA calculation. Both

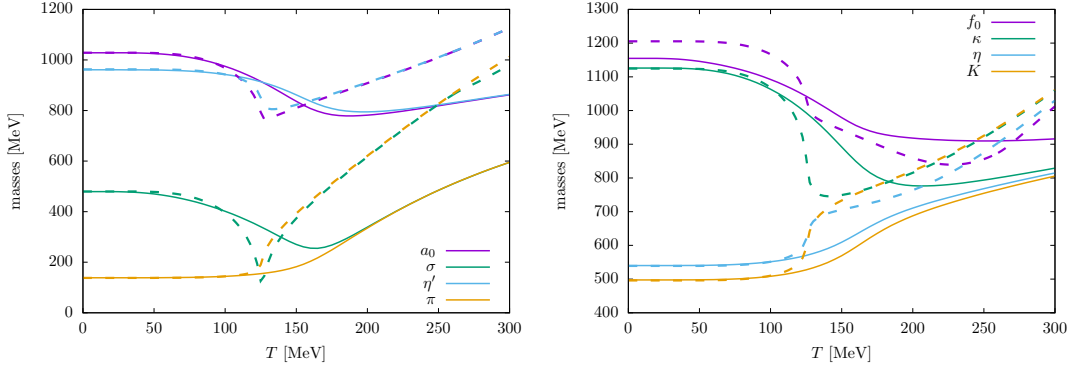


Figure 6.4: Temperature dependence of the scalar and pseudoscalar meson masses with $U(1)_A$ anomaly at $\mu = 0$. Solid lines are FRG calculations and dashed lines are analogous calculations in mean field approximation.

observations can be understood as a consequence of the faster melting strange condensate in MFA.

With the chiral partners K and κ we find that the degeneration sets in at temperatures well above the pseudo critical temperature $T_c < T \sim 280$ MeV and the last remaining chiral partners f_0, η do not degenerate in the investigated temperature region. This is a result of non-ideal flavor mixing and broken $SU(3)_L \otimes SU(3)_R$ symmetry even at high temperatures due to a slowly vanishing strange condensate. At even higher temperatures all meson masses will eventually degenerate as $SU(3)_L \otimes SU(3)_R$ symmetry is fully restored. Because the 't Hooft determinant term ζ contains meson fields to the third power, the anomaly term in the meson masses is linear in the fields. Consequently the mass gaps caused by the anomaly will also vanish at very high temperatures when $\sigma_l \rightarrow 0$ and $\sigma_s \rightarrow 0$. In MFA the f_0 meson becomes lighter than κ , K and f_0 at temperatures $T \gtrsim 250$ and then approaches the f_0 mass from below. This is not seen in the FRG calculation where f_0 is always the heaviest meson.

Fig. 6.5 shows the meson spectrum with (solid lines) and without $U(1)_A$ anomaly (dashed lines). Without the anomaly η' degenerates with the pion for all temperatures and the dashed blue line is therefore hidden in Fig. 6.5 under the yellow pion mass line. The significant drop in the η' mass can be explained by the fact that without the anomaly it becomes a pseudo Goldstone boson. We also find that the scalar a_0 triplet drops 19% in mass if the anomaly is excluded. Furthermore, the mass gap between the chiral partners π, σ and η', a_0 vanishes above the pseudo critical temperature and all non-strange particles degenerate.

Without the anomaly we find that the f_0 and η masses increase by 11% and 17% respectively and consequently the f_0 meson degenerates with the κ, K and η mesons at higher temperatures when compared to the corresponding masses including the anomaly. It is possible that this is an artifact of the fitting procedure since the start parameters resulting in a specific sigma mass are possibly not unique. This means that there might be multiple start parameters that exactly reproduce the fitted parameters but give a different f_0, κ and η mass.

6.3 Pressure Density

With knowledge of the effective potential $\mathcal{U} \equiv \mathcal{U}_{k=0}$ a wide range of thermodynamic properties are easily calculated. For example the energy density ϵ , entropy density s , particle density n and pressure density p can be expressed as derivatives of the potential with respect to the thermodynamic variables T and μ

$$\epsilon = \mathcal{U} - T \frac{\partial \mathcal{U}}{\partial T} - \mu \frac{\partial \mathcal{U}}{\partial \mu}, \quad s = -\frac{\partial \mathcal{U}}{\partial T}, \quad n = -\frac{\partial \mathcal{U}}{\partial \mu}, \quad p = -\mathcal{U} \quad (6.1)$$

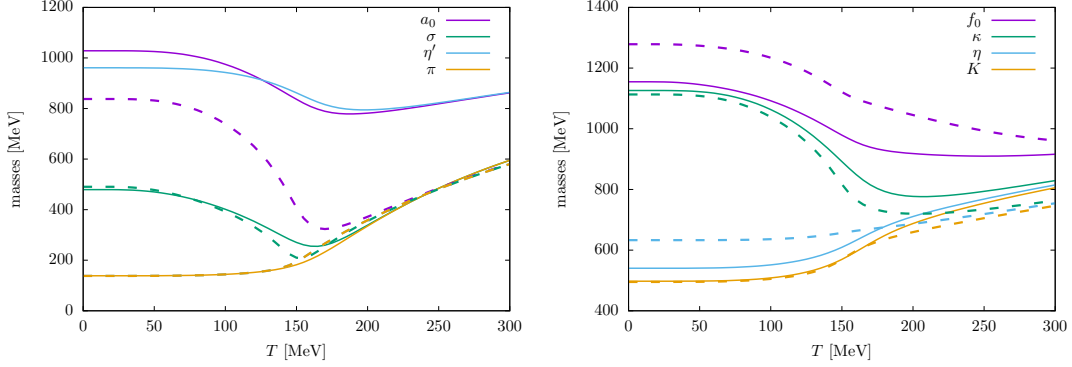


Figure 6.5: Temperature dependence of the meson masses with (solid lines) and without (dashed lines) $U(1)_A$ anomaly. Without the anomaly the η' meson degenerates with the pion at all temperatures.

and higher order derivatives lead to generalized susceptibilities.

Here we will only examine the pressure density in our truncation and compare it with lattice QCD data. We perform the comparison with lattice data in order to gauge the validity and expose missing contributions in our truncation.

In section 5.1 we have defined the truncation with a UV cutoff scale Λ . Thermal and quantum fluctuations with $q^2 > \Lambda^2$ are therefore lacking within our FRG treatment which leads to wrong high temperature behavior of thermodynamic properties. The pressure density is known to approach the Stefan Boltzmann (SB) limit at high temperatures which is for QCD

$$\frac{p_{SB}}{T^4} = \frac{N_f N_c}{6} \left[\frac{7\pi^2}{30} + \mathcal{O}(\mu^2) \right] + \frac{(N_c^2 - 1)\pi^2}{45}. \quad (6.2)$$

Here we use the following simplistic approach to cure the wrong high temperature limit: We add the potential of a free quark-gluon gas to the FRG effective potential which guarantees that eventually the SB limit is approached. This approach accounts for some thermal fluctuations, but ignores important interactions between quarks and gluons and gluon self interactions.

The fermionic part of the quark-gluon gas can be extracted from the flow equation (5.47) by omitting the meson terms and dropping the divergent vacuum contribution which can be absorbed in the normalization of the potential. We additionally set the quark masses to zero and add an ideal boson gas which incorporates free gluons. Putting all together the correction to the UV truncated potential reads

$$\mathcal{U}_{QG}^\Lambda(T, \mu) = \int_\Lambda^\infty dk \frac{k^3}{6\pi^2} [N_g n_B(k) + 2N_c N_f (n_F(k, \mu) + n_F(k, -\mu))] \quad (6.3)$$

with $N_g = 16$ and $n_B(k)$, $n_F(k, \mu)$ are the usual bosonic and fermionic occupation numbers

$$n_B(k) = \frac{1}{e^{k\beta} - 1}, \quad n_F(k, \mu) = \frac{1}{e^{(k-\mu)\beta} + 1}. \quad (6.4)$$

This integral can be performed numerically without further complications. The total expression for the pressure density within our procedure now reads

$$p(T) = -\mathcal{U}_{k=0}(T) + \mathcal{U}_{k=0}(T=0) - \mathcal{U}_{QG}^\Lambda(T). \quad (6.5)$$

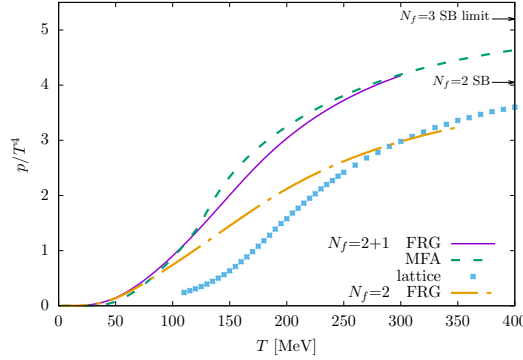


Figure 6.6: Temperature dependence of the scaled pressure density p/T^4 . For 2+1 flavor we show the FRG and MFA results and compare with Lattice data from [64]. Additionally we show the 2 flavor pressure density calculated with the bilocal expansion. The arrows denote the 2 and 3 flavor Stefan Boltzmann limit (see Eq. 6.2).

In Fig. 6.6 we show the resulting pressure density calculated with FRG and MFA. Since we have no cutoff scale in MFA the full range of thermal quark fluctuations is already included and only the free gluon gas has to be added. We also show recent lattice results for the 2+1 flavor pressure [64] and a 2 flavor FRG calculation which was done using the bilocal expansion. Compared to the lattice results the 2+1 flavor FRG pressure rises at smaller temperatures and approaches the SB limit significantly faster. This is mainly due to missing gluon fluctuations in our truncation. Since gluon self-interactions are attractive they reduce the pressure compared to an ideal boson gas. It is possible to incorporate gluon degrees of freedom in the form of an effective gluon potential for example through the Polyakov loop [21]. A variation of the Polyakov loop implemented within the 2+1 flavor quark-meson model is in perfect agreement with lattice results within temperatures upto 1.3 times the pseudo critical temperature [24]. In MFA we find a sharper increase in the pressure compared to our FRG calculation. Overall the difference is rather small and constrained to the temperature region $T \in [120, 240]$ MeV. We conclude that gluon fluctuations play a vital role in the thermodynamics of QCD, more so than meson fluctuations.

6.4 Finite μ and the Phase Diagram

In this section we investigate the phase structure of the 2+1 flavor model at finite chemical potential. We will focus on symmetric quark matter where $\mu = \mu_l = \mu_s$ for the most part of this section but towards the end also discuss the phase diagram for unsymmetric quark matter.

The typical behavior of the light condensate in the T, μ plane is depicted in Fig. 6.7. As already discussed for a sigma mass of $m_\sigma \sim 480$ MeV, the chiral transition is a smooth crossover at zero chemical potential in both FRG and MFA. Increasing μ the drop in the light condensate becomes steeper until the temperature derivative diverges at the critical end point. This is accompanied by a drop of the sigma mass at the CEP which is a general feature of the quark-meson model. We see this in the MFA calculation at $\mu_c \sim 165$ MeV and for even higher chemical potential both the light and strange condensates become discontinuous. This jump in the order parameter signals a first-order phase transition and is accompanied by the emergence of two discrete minima in the effective potential. The first-order critical line is then given as points in the T, μ plane where the potential values at both minima degenerate.

In agreement with earlier observations at vanishing chemical potential we find that fluctuations wash out the chiral phase transition and the first-order region is significantly smaller in the FRG calculation. Because the critical line curves onto the μ axis at large μ we define polar coordinates in T, μ space. In the crossover region we fix the critical line at the minimum of

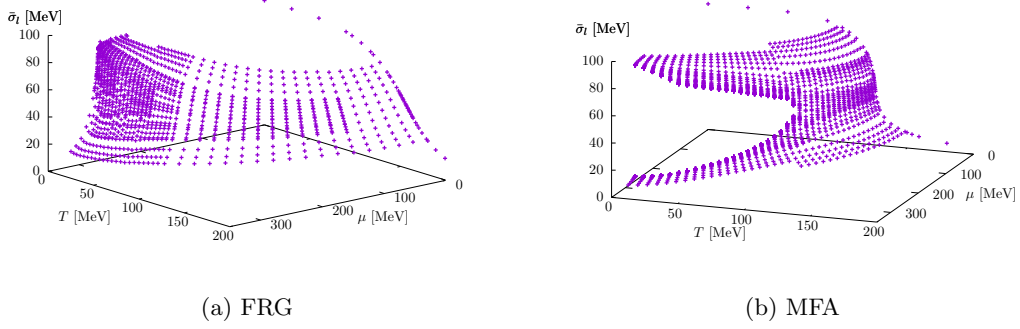


Figure 6.7: Light condensate near the critical line at $k_{\text{end}} = 90$ MeV and $m_\sigma = 480$ MeV. The left panel shows FRG result and right panel the corresponding MFA results. Only condensate values near the chiral transition were calculated.

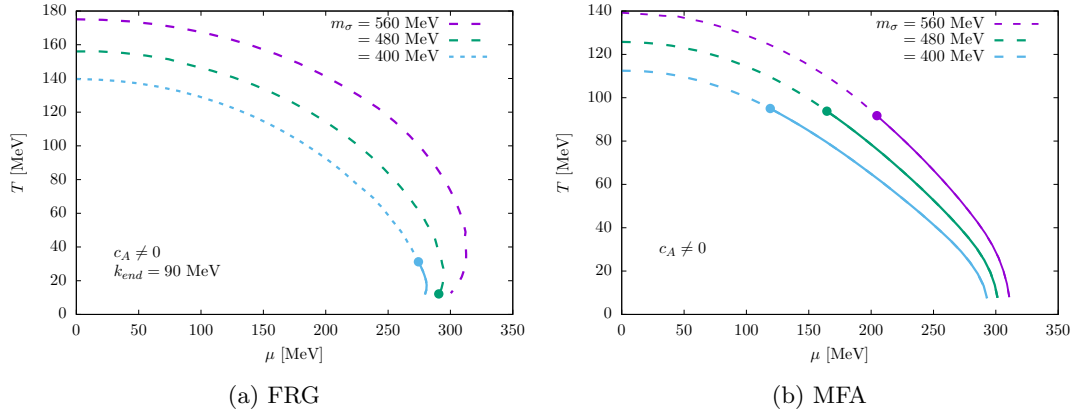


Figure 6.8: FRG (left panel) and MFA (right panel) phase diagram for three different sigma masses including axial anomaly. Dashed lines denote crossover and solid lines first-order phase transitions.

$\frac{\partial \bar{\sigma}_l}{\partial r}$, the derivative in radial direction. The crossover region spans over almost the entire T, μ plane and only at $(T_c, \mu_c) = (12.2, 290.7)$ MeV do we find that the radial derivative of the light condensate diverges and the identifying drop in the sigma mass. Temperatures lower than $T \sim 12$ MeV at high μ could not be accurately calculated due to numerical difficulties. It is, however, very likely that a small first-order region exists that connects the CEP with the μ axis.

We show the FRG and MFA phase diagrams for three different sigma masses in Fig. 6.8. Apart from the significantly smaller first-order region in the FRG calculation we find that the critical line bends backwards as it approaches the μ axis which is not seen in the MFA phase diagram. This is a common feature of FRG phase diagrams. The effect of the sigma mass on the phase diagram is qualitatively the same in FRG and MFA. With increasing sigma mass the critical line shifts to higher T and μ and the first-order region shrinks until at some critical sigma mass the CEP hits the μ axis. Within the FRG calculation this already happens at sigma masses around $m_\sigma \gtrsim 560$. However, because of the aforementioned numerical difficulties we can not give a precise value for this critical sigma mass.

In Fig. 6.9 we show both the 2+1 and 2 flavor phase diagram for a comparable sigma mass. We find that the course of the critical line is entirely determined by 2 flavor dynamics. The location of the CEP is pushed towards lower temperatures which suggests that the added

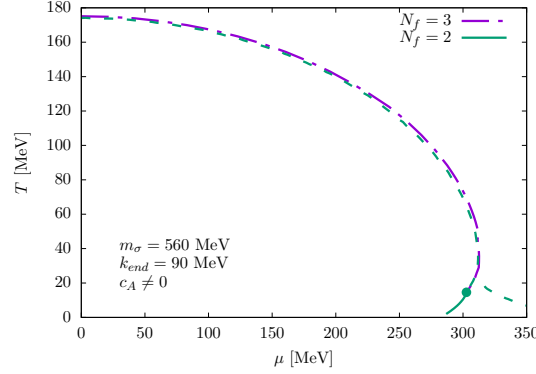


Figure 6.9: Phase diagram for 2+1 and 2 flavor. Dashed lines denote crossover and the green solid line first-order phase transitions. In the 2 flavor formulation a CEP is found at $(T_c, \mu_c) = (14.6, 302.695)$ MeV while for 2+1 flavor the phase transition is a smooth crossover at $T \sim 12$ MeV.

fluctuations further wash out first-order phase transitions which are mainly driven by the pion triplet and the two light quarks. In the 2+1 flavor case we can not make definite statements if a CEP exists for a sigma mass of $m_\sigma = 560$ MeV. However, the trend observed in Fig. 6.8 suggests that it is located at very small temperatures or is non existent. Furthermore, we could not identify the triangular structure of the phase diagram observed at low temperatures in the 2 flavor case. It is possible that the added fluctuations wash out this already subtle feature of the 2 flavor phase diagram, but it could also be missing due to numerical deficiencies in the 2+1 flavor setup.

Contrary to MFA where the 't Hooft term does not significantly influence the phase diagram we find that for the full FRG calculation the phase diagram is pushed inwards to smaller temperatures and chemical potential if the 't Hooft term is neglected ($c_A = 0$). This reduces the pseudo critical temperature at $\mu = 0$ by ~ 15 MeV and at low temperatures we find a difference in the critical chemical potential of ~ 23 MeV.

Finally, we extend our discussion to unsymmetrical quark matter where we consider two independent chemical potentials. The critical surface in T, μ_l, μ_s space is shown in Fig. 6.10. In the right panel we show the MFA result where we differentiate crossover- and first-order phase transitions by dashed and solid grid lines respectively. The FRG critical surface is crossover for the numerically treatable temperatures $T \gtrsim 12$ MeV shown in Fig. 6.10. It borders on a first-order region at low temperatures which can be inferred from the existence of a CEP at comparable temperatures (see Fig. 6.8). The general structure of the critical surface is the same in MFA and FRG. It takes on a *quarter dome*-like structure centered around $T = \mu_l = \mu_s = 0$ and stretched in the μ_s direction. The phase diagram for symmetric quark matter from Fig. 6.8 is found by a diagonal cut along the critical surface (red line in Fig. 6.10). Remarkably, the phase diagram for symmetric quark matter is almost identical to the $\mu_s = 0$ phase diagram (bottom plane in Fig. 6.10). We conclude that the chiral phase transition is mainly driven by light quark density and is less sensitive to the strange quark chemical potential. Further evidence of this is found at high μ_l and small temperatures: the critical surface is completely independent of μ_s until a critical value, comparable to the constituent strange quark mass, is reached, $m_s \sim \mu_s \sim 433$ MeV, from where on the critical surface collapses onto the μ_s -axis at $T = \mu_l = 0$.

Extrapolating to the critical chemical potential where the phase boundary hits the μ_l (or μ_s) axis at $T = \mu_s = 0$ (or $T = \mu_l = 0$) we find $\mu_{l,c} \sim 302$ MeV ($\mu_{s,c} \sim 495$ MeV) for the MFA calculation and $\mu_{l,c} \sim 280$ MeV ($\mu_{s,c} \sim 560$ MeV) in the FRG calculation. The higher critical $\mu_{s,c}$ can be understood as a consequence of the constituent quark mass being higher for strange quarks than for light quarks ($m_s \sim 433$ MeV vs. $m_l \sim 300$ MeV).

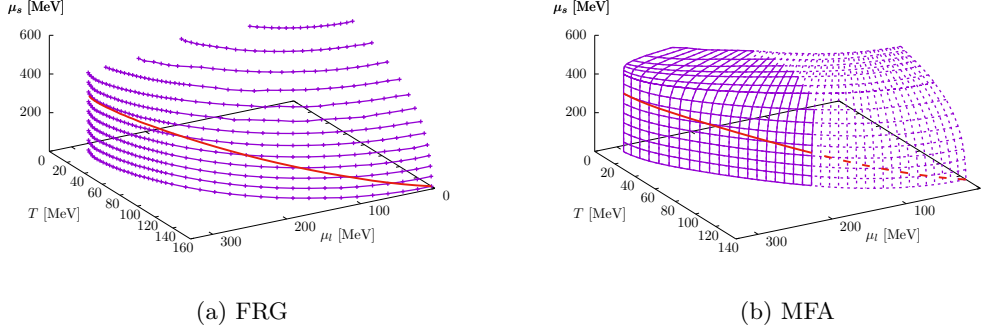


Figure 6.10: FRG (left panel) and MFA (right panel) critical surface in T , μ_l , μ_s space for $m_\sigma = 480$ MeV at $k_{\text{end}} = 90$ MeV including the axial anomaly. The FRG critical surface is crossover for the shown temperature region. The first-order region at $T \lesssim 12$ MeV could numerically not be reached. In the right panel dashed lines denote crossover and solid lines first-order regions of the MFA critical surface. The red line cuts across the critical surface at $\mu_l = \mu_s$ and projected onto the $\mu_s = 0$ plane gives the respective phase diagrams from Fig. 6.8.

6.5 The Light Chiral Limit

Finally, we investigate the chiral phase transition in dependence of c_l and c_s . An important limit of the 2+1 flavor system is the limit of vanishing light quark masses (*light chiral limit*). To this end we set the explicit symmetry breaking in the light direction c_l to zero and leave c_s at its physical value. In the Columbia plot the light chiral limit is reached by going left from the physical point.

We show both condensates at vanishing chemical potential, with and without anomaly in the left panel of Fig. 6.11. The order of the phase transition is determined by the state of $U(1)_A$ symmetry: Including the anomaly we find a second-order phase transition at $\mu = 0$. This supports the idea that a tricritical point exists at some $m_{s,\text{tri}} < m_{s,\text{phys}}$ and $m_l = 0$ with a second-order line continuing along the m_s axis into the 2 flavor limit. Without the anomaly we find a discontinuity in the light condensate indicating a first-order phase transition.

In MFA the chiral phase transition is first-order at $\mu = 0$ independent of axial anomaly. Consequently we find a first-order transition line over the whole T , μ plane. The sigma mass does not have any effect on the order of the chiral phase transition. However, as in the physical phase diagram the critical line is moved to higher T and μ with increasing m_σ . Including the vacuum term which we neglect in the standard mean field approximation a second-order phase transition has been observed both with and without anomaly [23].

The full FRG phase diagram for symmetric quark matter is shown in the right panel of Fig. 6.11. With anomaly the CEP is found at $(T_c, \mu_c) = (54.1, 240.0)$ MeV. Compared to the corresponding physical phase diagram (depicted in Fig. 6.8) the CEP moves to higher temperatures and lower chemical potential so that the first-order region is significantly larger in the light chiral limit. Without the anomaly no CEP exists and the critical line is always first order. Both critical lines could not be continued to the μ axis due to numerical instabilities at high μ and small T .

In Fig. 6.12 we compare 2+1 and 2 flavor phase diagrams of the light chiral limit with comparable sigma masses. Both critical lines exactly overlap and only the location of the CEP is pushed to marginally smaller temperatures if strange dynamics are included. This again supports the observation that the chiral phase transition is completely driven by 2 flavor dynamics. In the 2 flavor chiral phase diagram a unique triangular structure with a secondary CEP is observed at low temperatures. This could not be reproduced in the 2+1 flavor calculation since only temperatures above $T \gtrsim 20$ MeV could be calculated due to numerical deficiencies of the two dimensional grid.

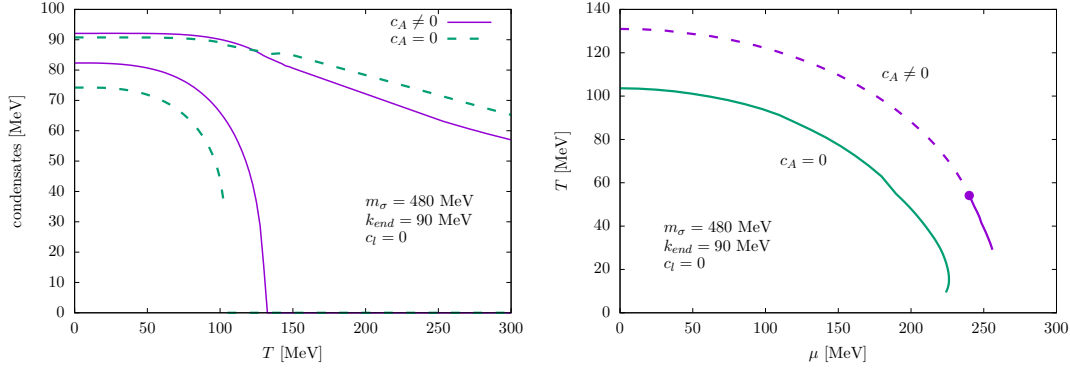


Figure 6.11: *Left panel:* Temperature dependence of the condensates in the light chiral limit ($c_l = 0$) with and without anomaly for $\mu = 0$. Without the anomaly a discontinuity is seen in the light condensate which indicates a first-order phase transition at $\mu = 0$. *Right panel:* Phase diagram of the light chiral limit with and without axial anomaly. Dashed line denotes a crossover and solid lines first-order phase transition. Without the anomaly there is no CEP and the phase transition is first-order even at $\mu = 0$. The phase transition lines could not be continued to the μ axis due to numerical difficulties.

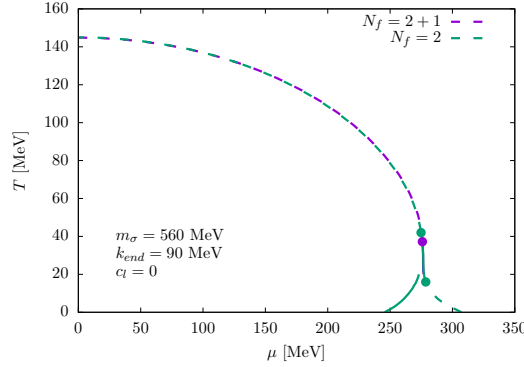


Figure 6.12: Comparison of the 2+1 flavor and 2 flavor phase diagram in the light chiral limit. Both critical lines lie on top of each other and only the location of the CEP shifts to slightly lower temperatures in the 2+1 flavor model. Only temperatures $T \gtrsim 20$ MeV could be numerically calculated in the 2+1 flavor case.

6.6 The Chiral Critical Line

We extend the discussion of the previous section by investigating the chiral phase transition for arbitrary symmetry breaking parameters c_l and c_s . Many interesting limits are contained in the 2+1 flavor system by adjusting the symmetry breaking parameters. For example if c_s is increased from its physical value, the strange quark and all mesons containing strangeness will gain in mass and eventually decouple from the flow. This is equivalent to a 2 flavor description and depending on the state of the anomaly will reproduce the phase diagram of the $SU(2)_L \otimes SU(2)_R$ or $U(2)_L \otimes U(2)_R$ model. Similarly we recover a one flavor model in the limit $c_l \rightarrow \infty$. This is, however, highly non-physical since it essentially means that the light quarks have infinite mass while the strange quark mass is finite.

Another important limit is the full chiral limit given by $c_l = c_s = 0$. Renormalization group arguments predict a first-order phase transition in the three flavor chiral limit independent of the state of $U(1)_A$ symmetry [27]. We investigate how this prediction connects with the physical point where the chiral phase transition is a smooth crossover.

By using the Ward identities

$$c_l = f_\pi m_\pi^2, \quad c_s = \sqrt{2} f_K m_K^2 - \frac{1}{\sqrt{2}} f_\pi m_\pi^2 \quad (6.6)$$

we express the symmetry breaking parameters in terms of pion and kaon masses. A direct translation from c_l, c_s to light and strange current quark masses is not apparent beyond the mean field level and we therefore investigate the order of the chiral phase transition in the m_π, m_K plane.

Spontaneous Symmetry Breaking in the Chiral Limit. While the light chiral limit gives reasonable values for f_π that are in agreement with chiral perturbation theory [68] we find, going into the full chiral limit, that both light and strange condensates vanish. We visualize this in Fig. 6.13 where we have chosen a straight path from the physical point to the chiral limit

$$\begin{pmatrix} c_l \\ c_s \end{pmatrix} = \alpha \cdot \begin{pmatrix} c_{l,phys} \\ c_{s,phys} \end{pmatrix}. \quad (6.7)$$

Both condensates melt with decreasing α and at the chiral limit ($\alpha = 0$) they are exactly zero. Furthermore, we find that the drop in the sigma mass shifts towards $T = 0$ and therefore $T_c \rightarrow 0$ going into the chiral limit. This implies that no spontaneous symmetry breaking occurs in the chiral limit which is in contradiction to arguments made in section 3.3: The formation of quark-antiquark condensates is favored for massless quarks, since the energy cost of creating such a pair decreases with the quark mass.

The absence of spontaneous symmetry breaking in our model is seen more explicitly in the MFA formulation. Considering only the light sector of the meson potential we have in chiral limit

$$U(\bar{\sigma}_l) = \frac{m^2}{2} \bar{\sigma}_l^2 + \frac{2\lambda_1 + \lambda_2}{8} \bar{\sigma}_l^4. \quad (6.8)$$

Assuming $2\lambda_1 + \lambda_2 > 0$ so that the potential is bounded from below a finite expectation value for $\bar{\sigma}_l$ is only generated if $m^2 < 0$. With the parameter fixing procedure described in Appendix C we find for sigma masses in the range $m_\sigma \in [400, 600]$ MeV that m^2 is positive and therefore no spontaneous symmetry breaking is observed. In MFA this can be cured by setting the sigma mass unreasonably high ($m_\sigma \sim 800$ MeV) where m^2 becomes negative [32]. This is not possible within the FRG formulation where the flow equation dictates that only sigma masses in the range $m_\sigma \in [400, 600]$ MeV can be found.

In Sec. 3 we have seen that the one-loop β -function of QCD becomes positive for $N_f > 33/2$ so that QCD transforms from an asymptotically free to an IR free theory as the number of flavors is increased. Adding further quark dynamics therefore reduces the strong coupling in the IR. For spontaneous symmetry breaking to occur some critical value for the strong coupling must be exceeded and the question arises if already for three massless quarks the strong coupling falls below this critical value. Intuitively, this seems highly unlikely since the strange quark is already light compared to charm, top and bottom quarks. Furthermore, lattice simulations with light domain wall fermions see clear signs of spontaneous chiral symmetry breaking [69] upto $N_f = 8$.

For the remainder of this investigation we will assume that spontaneous symmetry breaking should be present in the QCD vacuum. Its absence in our model is likely related to the parameter fixing procedure. So far we have held all parameters in the UV constant and only adjust c_l, c_s going into the chiral limit. The flow from the perturbative region of QCD to our initial scale $\Lambda = 700$ MeV will certainly produce different initial conditions depending on

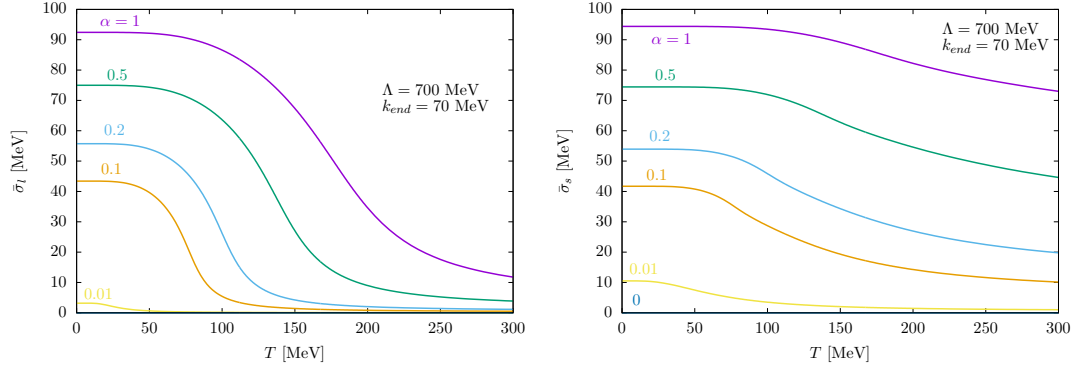


Figure 6.13: Light and strange condensates in dependence of temperature as the chiral limit is approached. The parameter α linearly interpolates between the physical point ($\alpha = 1$) and the chiral limit ($\alpha = 0$). Both condensates vanish in the chiral limit, signaling that no spontaneous symmetry breaking occurs.

the quark masses. Without direct access to the perturbative regime it is not clear how the initial parameters change and here we propose a somewhat heuristic approach to account for the changing potential at Λ : Instead of changing the initial parameters we adjust the UV cutoff Λ while approaching the chiral limit. With this we fix the light condensate in the vacuum for each value of c_l and c_s to its physical value of $\bar{\sigma}_l = f_\pi = 92.4$ MeV, i.e. we force spontaneous symmetry breaking also in the chiral limit.

With an increasing UV cutoff the system is allowed more *time* in the chirally symmetric regime and crucially the chiral symmetry breaking scale $k_{\chi SB}$ rises. We use this to counteract the decreasing $k_{\chi SB}$ going into the chiral limit and by fixing $\bar{\sigma}_l$ in the IR the symmetry breaking scale is held almost constant for different c_l and c_s .

The approach into the chiral limit can be seen in Fig. 6.14 where we show both condensates and the sigma mass for different cutoff values starting with $\Lambda = 700$ MeV at the physical point going up to $\Lambda \sim 1143$ MeV in the chiral limit. For each cutoff value we have adjusted c_l and c_s such that $\bar{\sigma}_l = 92.4$ MeV in the IR. Since we have only one condition and two parameters c_l and c_s each cutoff value corresponds to a line in the c_l, c_s or equivalently in the m_π, m_K plane. For Fig. 6.14 we have again chosen a straight path from the physical point to the chiral limit with the interpolating parameter α .

Going into the chiral limit the light condensate at $T = 0$ is fixed by construction. With decreasing α the chiral phase transition gets steeper and in the chiral limit ($\alpha = 0$) we find a first-order phase transition in agreement with [27]. We note that for $\Lambda = 1100$ MeV which corresponds to $\alpha \sim 0.04$ the phase transition is still crossover which indicates that the first-order region around the chiral limit is fairly small. Going into the chiral limit the strange condensate drops by about 30%. The reasoning for not fixing the strange condensate to the physical point is as follows: The light quark constituent mass is almost entirely generated by spontaneous symmetry breaking and only about 0.8%-1.6% of the constituent mass comes from its current mass. Therefore it is reasonable to assume that the constituent mass is not changed significantly going into the chiral limit. On the other hand, the strange quark has a significantly higher current mass which makes up about 23% of its constituent mass. Since $\bar{\sigma}_s$ is connected to the constituent mass of the strange quark it will decrease going into the chiral limit because the contribution from the current quark mass vanishes.

The existence of a critical end point at $\mu = 0$ going from the physical point toward the chiral limit is further suggested by the drop in the sigma mass. At some critical value $0 < \alpha_c < 0.04$ it drops to zero at the critical temperature and for $\alpha < \alpha_c$ the chiral phase transition is first order.

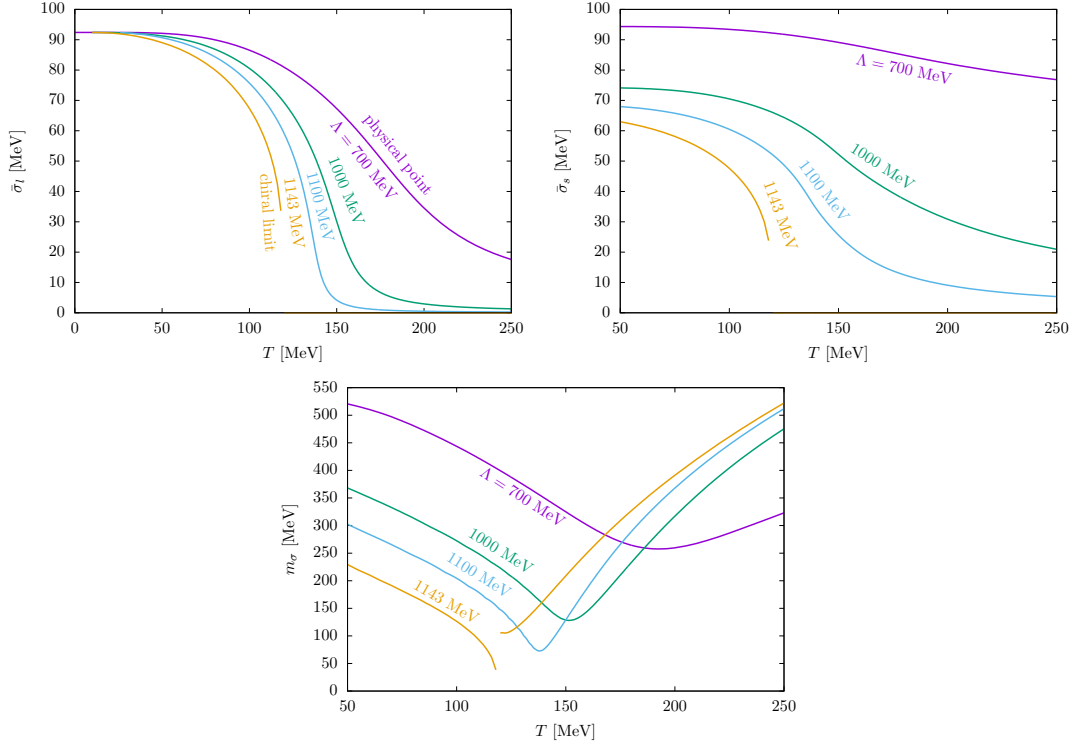


Figure 6.14: Condensates and sigma mass in dependence of temperature as the chiral limit is approached. For each cutoff value the symmetry breaking parameter has been adjusted such that $\bar{\sigma}_l = 92.4$ in the vacuum. The symmetry breaking parameters are $c_{l/s} = (0, 0.04, 0.17, 1) \cdot c_{l/s,phys}$ corresponding to $\Lambda = (1143, 1100, 1000, 700)$ MeV.

The Chiral Critical Line in MFA. We start our discussion by examining the order of the chiral phase transition without meson fluctuations. We use model parameters that give a sigma mass of $m_\sigma = 800$ MeV to ensure spontaneous symmetry breaking in the chiral limit. The order of the chiral phase transition is identified for different combinations of c_l and c_s , including the chiral limit. The result for vanishing chemical potential are shown in Fig. 6.15 where we use Eq. (6.6) to translate from c_l , c_s to m_π , m_K . In the left panel the 't Hooft term is included and in the right panel $c_A = 0$ so that $U(1)_A$ symmetry is intact. In both cases we find a first-order phase transition in the chiral limit and a surrounding first-order region which follows along the m_K axis. It is separated from the crossover region by a second-order line—the *chiral critical line*—marked in red in Fig. 6.15. The physical point lies in the crossover region as suggested by earlier results. With included 't Hooft term the first-order band along the m_K axis spans up to a pion mass of $m_\pi \sim 57$ MeV. With decreasing kaon mass the critical line bends away from the m_K axis.

Without the 't Hooft term the critical line is constant at $m_\pi \sim 55$ MeV and no bending away from the m_K axis could be observed. The blank triangles in the lower right corner of both graphs is an area with negative c_s which happens for $m_K < \sqrt{f_\pi/2f_K}$.

Finally, we extend the critical line into the $\mu = \mu_l = \mu_s$ dimension which gives rise to a critical surface. The existence of a CEP in the physical phase diagram already allows us to exclude the non standard scenario since we know that the physical point must hit the critical surface at μ_{CEP} . Fig. 6.16 shows the critical surface in m_π, m_K, μ space with and without axial anomaly. As expected the curvature of the critical surface is positive at $\mu = 0$ so that the first-order region is expanded with increasing μ .

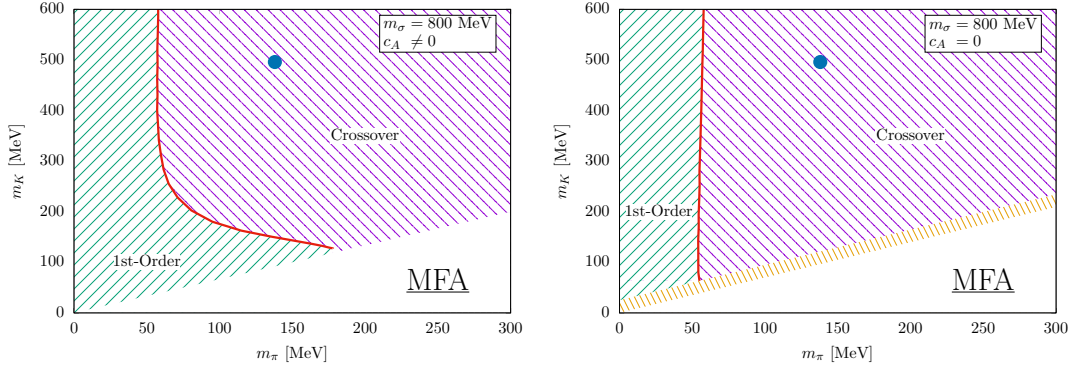


Figure 6.15: Order of the chiral phase transition in dependence of m_π and m_K in MFA. Here $\mu_l = \mu_s = 0$ and $m_\sigma = 800$ MeV. Left panel with- and right panel without axial anomaly. First-order and crossover regions are separated by the chiral critical line (red). The blank triangle in the lower right of both graphs is an area with negative c_s which happens for $m_K < \sqrt{f_\pi/2f_K}$. The yellow band in the right panel could not accurately be determined and might involve a sharp turn of the chiral critical line. The blue dot indicates realistic pion and kaon masses (physical point).

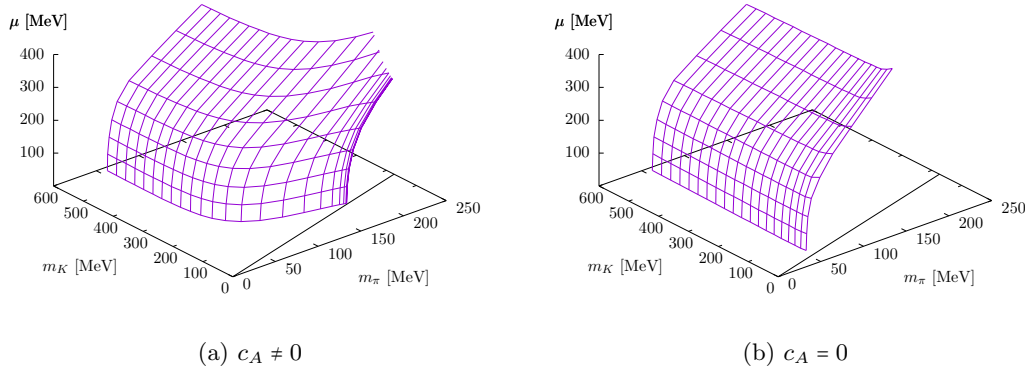


Figure 6.16: MFA critical surface in m_π , m_K , μ space for $m_\sigma = 800$ MeV with and without axial anomaly. In both cases the curvature of the critical surface is positive.

The Chiral Critical Line Including Fluctuations. In Fig. 6.17 we show the order of the chiral phase transition in dependence of m_π and m_K including meson fluctuations within the FRG framework. We force chiral symmetry breaking in the chiral limit by applying the procedure discussed above. A detailed description of the numerical steps leading to Fig. 6.17 are disclosed in Appendix D.

We have already seen that in the light chiral limit the order of the phase transition is dependent on the state of $U(1)_A$ symmetry. Including the 't Hooft term we see a second-order phase transition at $\mu = 0$ and this holds true for less than physical kaon masses as can be seen in the left panel of Fig 6.17. We find a second-order phase transition line right at the m_K axis. Only at the tricritical point at kaon masses of $m_{K,tric} \sim 25$ MeV does the chiral critical line turn away from the m_K axis and thereby encloses a small first-order region surrounding the chiral limit. Note that the plot range is enlarged in the left panel compared to other figures. While examining the physical phase diagram we have seen that meson fluctuations wash out first-order phase transitions and here it leads to a collapse of the first-order region to pion and kaon masses of $m_\pi \lesssim 20$ MeV, $m_K \lesssim 25$ MeV. We indicate with the dashed line in Fig. 6.17 that

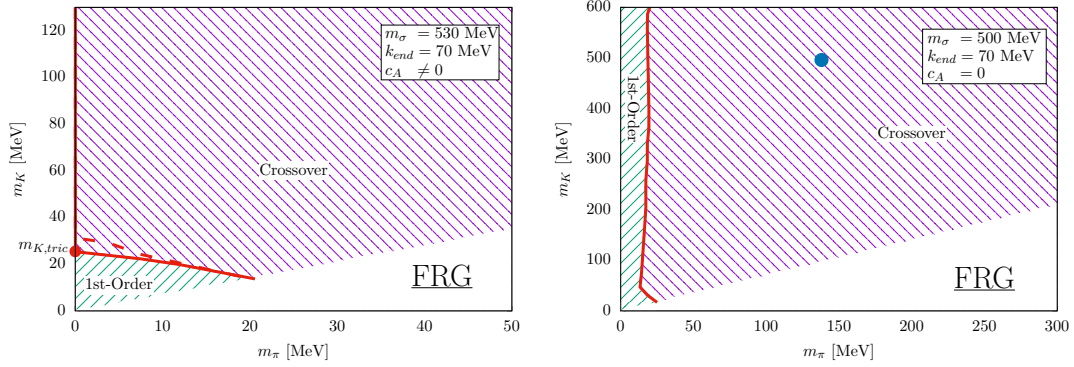


Figure 6.17: Order of the chiral phase transition in dependence of m_π and m_K including fluctuations. Left panel with and right panel without axial anomaly. First-order and crossover regions are separated by the chiral critical line (solid red line). The blank triangle in the lower right of both graphs is an area with negative c_s . With included anomaly we find a tricritical point at $m_K \sim 25$ MeV and $m_\pi = 0$. The dashed line in the left panel denotes the second-order transition line at $k_{\text{end}} = 100$ MeV and implies that the tricritical point has not entirely converged in k . The blue dot in the right panel indicates realistic pion and kaon masses (physical point).

the location of the tricritical point is not completely settled in the RG flow. Between $k = 100$ MeV and $k = 70$ MeV the tricritical point moves towards lower kaon mass by $\Delta m_K \sim 6$ MeV.

Without anomalous breaking of $U(1)_A$ we find a first-order band that continues along the m_K axis similar to the MFA results. For kaon masses larger than $m_K \sim 47$ the chiral critical line runs loosely perpendicular to the m_K axis at a pion mass of $m_\pi \sim 20$ MeV. Continuing this into the 2 flavor limit we have a tricritical point at $m_{\pi, \text{tric}} \sim 20$ MeV and $m_{K, \text{tric}} = \infty$. A more precise assessment of $m_{\pi, \text{tric}}$ could be made by investigating the order of the phase transition in a $U(2)_L \otimes U(2)_R$ model in dependence of c_l . On the lower side of the m_π, m_K plane we find for kaon masses $m_K \lesssim 47$ MeV a trend away from the m_K axis until a pion mass of $m_\pi = 25$ MeV is reached.

Our results both with and without anomaly extrapolate well into the corresponding 2 flavor limit. If $U(1)_A$ is broken we recover the $SU(2)_L \otimes SU(2)_R$ quark-meson model. It exhibits a second-order phase transition at $\mu = 0$ in the (light) chiral limit. The second-order line along the m_K axis is therefore likely continued into the 2 flavor limit. Similarly, in the case of intact $U(1)_A$ symmetry renormalization group arguments predict a first-order phase transition for $N_f = 2$ [27]. This is also in agreement with our findings if we continue the first-order band along the m_K axis.

Seven

Numerical Implementation

In section 5.2 we have derived a flow equation that connects the bare action at a UV cutoff with the truncated effective action or effective potential in the IR. In our case the flow equation (5.47) is a highly non-linear, stiff partial differential equation and no procedure is known which solves such a differential equation analytically. We therefore turn to numerical methods, where the study of partial differential equations is a vast field. Approaches to solve flow equations for the effective potential usually fall under one of two broad categories: A Taylor expansion of the potential breaks down the infinite number of couplings to a truncated set of coupled β -functions [25, 70, 71]. The expansion can be done either around a fixed expansion point (*static Taylor*) or around the k -dependent minimum of the potential (*co-moving Taylor*). For $O(N)$ models the co-moving Taylor has been found to converge, see e.g. [15]. However, for models including fermionic and mesonic degrees of freedom this is not necessarily true and a static expansion might be preferable as we will show later (see also [72]). Both Taylor expansions have in general a limited range of validity which might not include a secondary minimum of the potential. Accurate knowledge of all local minima becomes important when investigating the order of a phase transition. To this end one can discretize the independent variables of the effective potential on a so called grid and solve the flow equation on each grid point [19, 73, 74]. The differentiating factor for grid methods is the way in which the derivatives on the right hand side of the flow equation are calculated. Recently, pseudo-spectral methods have been used to integrate flow equations with promising results [75].

The purpose of this section is twofold: First we describe the numerical setup for the 2+1 flavor investigation where we solve the flow equation on a two dimensional grid. Then we briefly present a novel method which combines the benefits of a standard Taylor expansion and general grid methods. A more detailed discussion of this *bilocal* expansion scheme can be found in [76].

7.1 Two Dimensional Grid

We start by defining the independent, positive variables [23]

$$x = \sigma_l^2, \quad y = 2\sigma_s^2 - \sigma_l^2. \quad (7.1)$$

The vacuum expectation values of the chiral invariants in terms of the new coordinates are given by

$$\rho_1 = \frac{1}{4}(3x + y), \quad \tilde{\rho}_2 = \rho_2 - \frac{\rho_1^2}{3} = \frac{y^2}{24}. \quad (7.2)$$

Here we have introduced a modified chiral invariant $\tilde{\rho}_2$ which simplifies some expressions later on. We rewrite all derivatives that enter in the meson masses as derivatives with respect

to x and y by applying the chain rule (see Appendix B.1). Finally, we discretize both the x and y coordinate and solve the flow equation on each grid point

$$\partial_t U_k(x, y) \rightarrow \partial_t U_k(x_i, y_j) \equiv \partial_t U_{ij} = f \left(U_k, U_k^{(1,0)}, U_k^{(0,1)}, U_k^{(2,0)}, U_k^{(0,2)}, U_k^{(1,1)} \right) \Big|_{x=x_i, y=y_j} \quad (7.3)$$

where we have used the notation $U_k^{(p,q)} \equiv \partial_x^p \partial_y^q U_k(x, y)$. The derivatives on the right hand side of the flow equation can be calculated for example using finite difference formulas or an appropriate interpolation method. This will give a linear relation between derivative- and potential values at each grid point which we can write as $U_{ij}^{(p,q)} = A_{ijmn}^{(p,q)} U_{mn}$. Plugging this into the flow equation we arrive at a set of coupled ordinary differential equations which can be solved by standard numerical methods

$$\partial_t U_{ij} \equiv \tilde{f}(\{U_{ij}\}). \quad (7.4)$$

Solving FRG flow equations in this manner is often computationally expensive because of singular terms of the form $1/\sqrt{k^2 + 2U^{(1,0)}}$ which are hard to evaluate at small field values where $U^{(1,0)} \sim k^2/2$. However, one is awarded with the full potential at a wide range of field values which makes it possible to identify first-order phase transitions and metastable states. Since the flow equation for our truncation can be classified as a stiff equation it is worthwhile to use an implicit ODE solver instead of the usual explicit Runge Kutta method. But even with an implicit solver the approach to the IR is hampered by the non-analytical behavior of the solution, which foils all good convergence properties of the interpolation method. Generally $k = 0$ can not be reached and one has to choose a point k_{end} where all relevant fluctuations are included. Furthermore, the computation required for a single evaluation of the flow equation increases with $\mathcal{O}(N^2)$ where N is the number of grid points in x and y direction. This is a serious challenge for the computations on a two dimensional grid. CPU time has to be constantly balanced against needed accuracy which can be adjusted with the number of grid points.

For the 2+1 flavor results presented in this thesis we have used the following setup: We initialized an equidistant grid in $\sqrt{x} = \sigma_l$ and $\sqrt{y} = \sqrt{2\sigma_s^2 - \sigma_l^2}$ so that the final grid is linear in the field dimension. This has proven to be more accurate than a grid equidistant in x and y when describing phase transitions with a relatively low number of grid points. However, for a sufficiently high number of grid points both give identical results. In order to calculate the derivatives of the potential on the right hand side of the flow equation we have used cubic spline interpolation in two dimensions. This interpolation was also used to determine the minimum (minima) of the potential and derivatives at that point which enter in the meson masses. Having established the linear relation between the potential values at each grid point and derivatives of the potential, we solved the resulting set of coupled ordinary differential equations using the semi-implicit ODE solver **StepperSie** as implemented in [77]. We have found that the semi-implicit solver performs significantly better in our case than various Runge Kutta solvers.

In order to make sure that the numerical results are reliable we have performed the following checks for all calculations: We have compared different values of k_{end} to determine whether the flow has converged. If we do not point it out specifically in Sec. 6 no significant dependence on k_{end} could be found. Additionally we have repeated the calculations with different grid configurations e.g. by increasing the number of grid points and varying the start and end points of the grid. Numerical accuracy varies heavily for different T, μ points. We find that a $N_x \times N_y = 15 \times 15$ grid is already sufficient to give reliable results at $\mu = 0$. Closer to the critical end point we have increased the number of grid points to 30×20 and sometimes 40×20 . These configurations were used for all calculations involving a possible first-order phase transition. An even finer grid would further decrease the error for example in Fig. 6.17.

7.2 Bilocal Expansion

We now present a novel method to solve flow equations that bridges the gap between standard Taylor expansions and grid methods. The key idea behind the bilocal expansion scheme is to extend the standard Taylor method to find a global solution of the potential and not one that is limited to a small range of field values. We start by expanding the potential up to order N around two distinct expansion points ρ_L and ρ_R . We restrict ourselves to a potential dependent upon one invariant ρ but generalizations to arbitrary independent variables should be straight forward. The goal is to transfer information from one expansion point to the other i.e. couple both expansions together. We do so by demanding both expansions to be equal for all ρ

$$U_k(\rho) = \sum_{i=0}^N \frac{a_i}{i!} (\rho - \rho_L)^i = \sum_{i=0}^N \frac{b_i}{i!} (\rho - \rho_R)^i . \quad (7.5)$$

The coefficients a_i and b_i are RG-scale dependent while the expansion points ρ_L and ρ_R are not, as in a static Taylor expansion. This is certainly not the only possible coupling procedure and there is plenty of room for experimentation.

Continuing with Eq. (7.5) we can compare in powers of ρ which gives

$$\sum_{i=n}^N \frac{a_i}{i!} \binom{i}{n} (-\rho_L)^{i-n} = \sum_{i=n}^N \frac{b_i}{i!} \binom{i}{n} (-\rho_R)^{i-n} \quad n = 0, \dots, N . \quad (7.6)$$

These are $N + 1$ equations for the in total $2(N + 1)$ coefficients a_i and b_i which have to be determined. Similar to a standard Taylor expansion we solve the flow of coupled β -functions $\partial_t a_i$ and $\partial_t b_i$ but with Eq. (7.6) we can reduce the number of β functions by $N + 1$. To make this explicit we divide the $2(N + 1)$ coefficients into $N + 1$ *known* and $N + 1$ *unknown* coefficients

$$\text{known: } \mathbf{a}_k \equiv \underbrace{(a_0, \dots, a_{N/2-1})}_{N/2} \quad \mathbf{b}_k \equiv \underbrace{(b_0, \dots, b_{N/2})}_{N/2+1}, \quad (7.7)$$

$$\text{unknown: } \mathbf{a}_u \equiv \underbrace{(a_{N/2}, \dots, a_N)}_{N/2+1} \quad \mathbf{b}_u \equiv \underbrace{(b_{N/2+1}, \dots, b_N)}_{N/2}. \quad (7.8)$$

For the $N + 1$ known coefficients we solve the β -functions which generally depend upon the $N + 1$ unknown coefficients. For every instance in the flow¹ we calculate the unknown coefficients from the known coefficients using Eq. (7.6). The specific choice made in (7.7) is again not unique but it is in our experience the numerically most stable configuration and we therefore restrict our discussion to this specific case.

Eq. (7.6) can be written as a linear matrix equation

$$A(\rho_L) \cdot \begin{pmatrix} \mathbf{a}_k \\ \mathbf{a}_u \end{pmatrix} = B(\rho_R) \cdot \begin{pmatrix} \mathbf{b}_k \\ \mathbf{b}_u \end{pmatrix} \quad (7.9)$$

with the matrices

$$(A(\rho_L))_{ji} = \begin{cases} \frac{1}{j!(i-j)!} (-\rho_L)^{i-j} & \text{if } i \geq j \\ 0 & \text{otherwise} \end{cases}, \quad (B(\rho_R))_{ji} = \begin{cases} \frac{1}{j!(i-j)!} (-\rho_R)^{i-j} & \text{if } i \geq j \\ 0 & \text{otherwise} \end{cases}. \quad (7.10)$$

¹Practically this means for every k -step the ODE solver takes.

This set of equations has to be solved for the unknown coefficients \mathbf{a}_u and \mathbf{b}_u . Since $A(\rho_L)$ and $B(\rho_R)$ are upper triangular matrices the inversion can be easily done analytically. If furthermore $\rho_L = 0$ the linear system of equations simplifies significantly.

To recap: we have connected two different points of the flow with a linear system of equations which essentially cuts the number of β -functions that have to be solved in half. If we choose for example $\rho_L = 0$ and $\rho_R = \sigma_R^2 = (90\text{MeV})^2$ then the potential will be continuous between these expansion points and not diverge as in the case of a standard Taylor expansion. It is important to keep in mind that the final potential is still only a polynomial of order N which is now tasked with describing the global potential instead of a limited range of field values. This is clearly a severe approximation to the true potential which is known to exhibit non analytic behavior in the IR. Crucially, the potential in the IR becomes convex and within our bilocal expansion scheme it is not possible to describe a convex potential while remaining in the spontaneously broken regime. This is, however, not an eliminating fault since we extract all physical information at $k_{\text{end}} > 0$ where the potential is not necessarily convex anyway.

Results for the 2 flavor quark meson model. We solve the bilocal system of equations with a standard Runge Kutta algorithm for the $SU(2)_L \otimes SU(2)_R$ realization of the flow equation (5.47) as described in Sec. 5.4. In Fig. 7.1 we show the potential for different values of k in the vacuum. The potential agrees with analogous calculations using a grid method and it is evident that with $k \rightarrow 0$ one approaches a convex potential even though no fully convex potential can be reached.

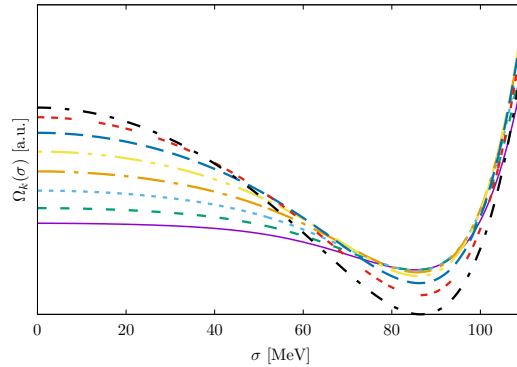


Figure 7.1: Potential calculated with the bilocal expansion at k values ranging from $k = 50$ MeV (innermost line) to 210 MeV (outermost line) with $\Delta k = 20$ MeV between each line. Convexity is approached in the IR even though no fully convex potential can be reached with the bilocal system.

We investigate the convergence properties in the expansion order N in Fig. 7.2. Using the same start parameters we extract f_π and the sigma mass in the IR for different N . We additionally compare this with a standard co-moving Taylor expansion and a static Taylor expansion using the same start parameters. With the co-moving expansion we find no clear sign of convergence. On the other hand, both the static and bilocal expansions converge already at order $N = 6$. In Fig. 7.3 we show the pressure density², f_π and the sigma mass at finite temperature and $\mu = 0$. We find that already $N = 4$ gives almost perfect agreement with grid calculations and only in the sigma mass small deviations can be found. At $N = 6$ or higher we find that the bilocal expansion reproduces the grid results. Similar agreement can be found with a static Taylor expansion which also converges already at $N = 6$ for the quantities discussed here.

²We do not add the ideal quark-gluon gas in this comparison which causes p/T^4 to fall off at large temperatures.

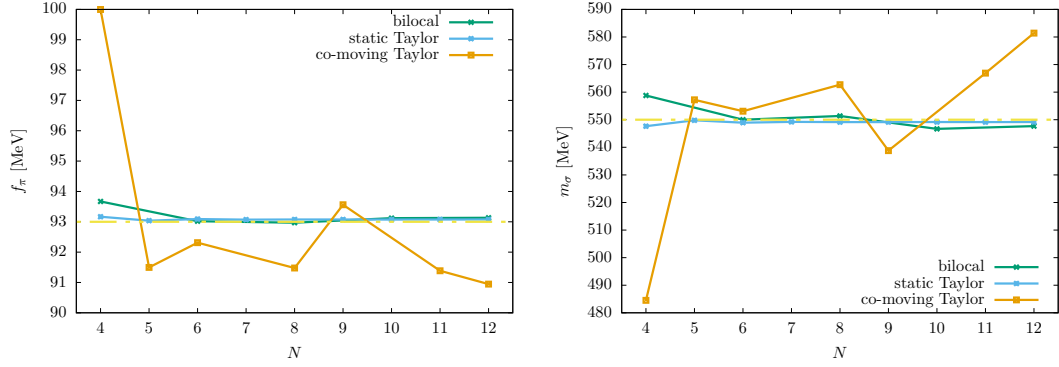


Figure 7.2: Convergence of the bilocal, static Taylor and co-moving Taylor system with the expansion order N . The co-moving Taylor system shows no definite convergence whereas both the static Taylor and bilocal expansion show excellent convergence.

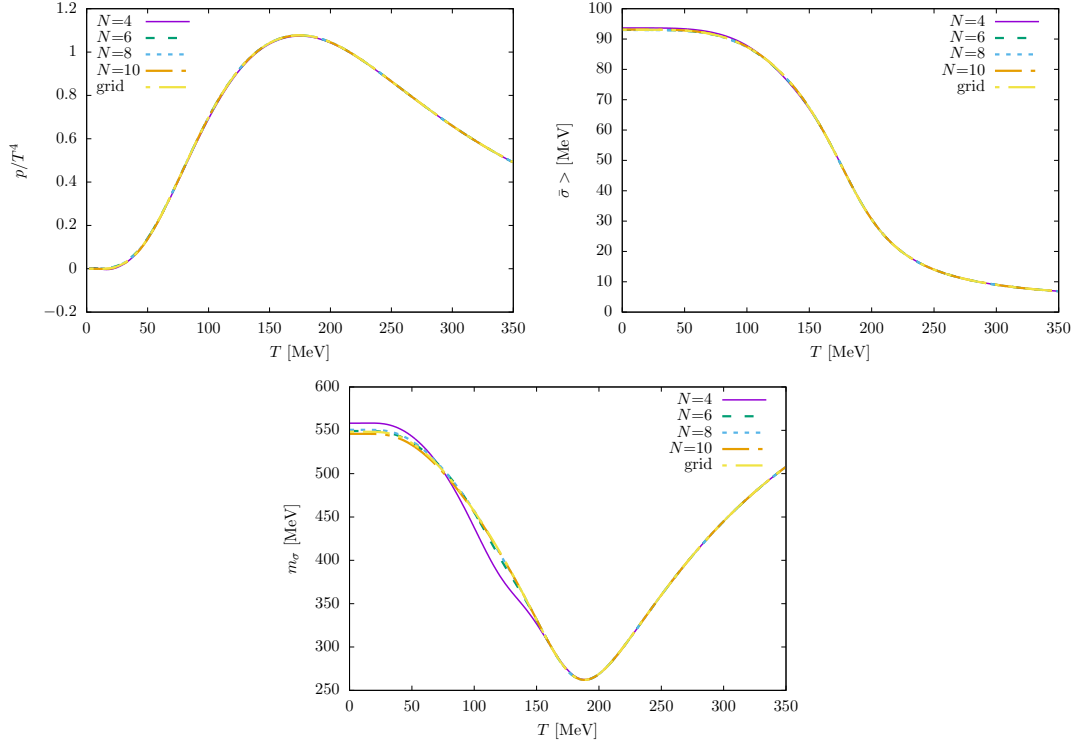


Figure 7.3: Temperature dependence of the pressure density, order parameter and sigma mass calculated with the bilocal expansion.

The reason why a standard Taylor expansion gives such accurate results for thermodynamic properties is that they are defined at the minimum of the potential. This means that if one tunes the expansion point such that the minimum lies within the range of validity it will give good results for thermodynamic properties. However, near a first-order phase transition at least two local minima will emerge in the potential and the range of validity of a standard Taylor expansion is often not wide enough to cover both. This is where the advantage of the bilocal expansion lies. Since the potential is known globally it encompasses all local minima and therefore allows an accurate description of first-order phase transitions. To show this we calculate the phase diagram of the 2 flavor quark-meson model in the chiral limit which is

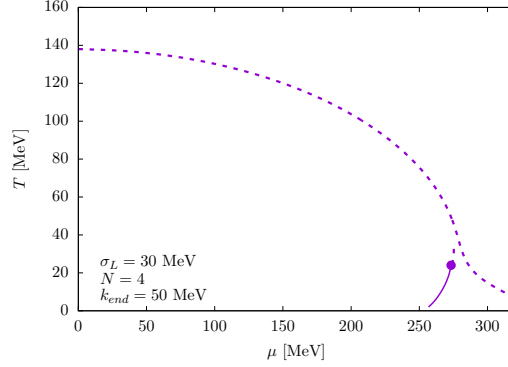


Figure 7.4: Phase diagram of the chiral $SU(2)_L \otimes SU(2)_R$ quark meson model calculated with the bilocal expansion. The dashed line denotes second-order phase transition and the solid line first order. Both regions are separated by a critical end point at $(T, \mu) = (273.3, 24.0)$ MeV.

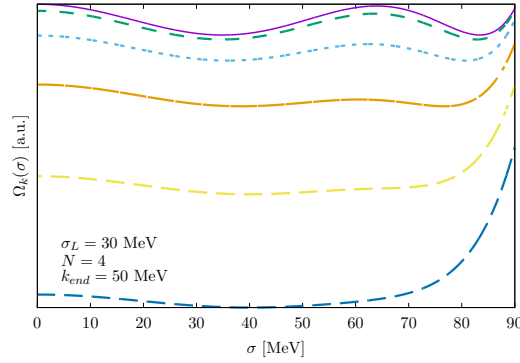


Figure 7.5: Multiple potentials along the critical line as seen in Fig. 7.4. The top line corresponds to $T = 5$ MeV and the lowest to $T = 30$ MeV with 5 MeV between each line. At low temperatures there is a distinct maximum between the two potential minima, which indicates a first-order phase transition. With increasing temperature this maximum is dampened until it vanishes at the critical end point from where on the first-order becomes a second-order phase transition.

essentially a replication of [19]. The phase diagram is depicted in Fig. 7.4. We find a critical end point at slightly lower temperatures compared to [19] but otherwise good agreement. Even the triangular structure at high μ can be observed with the bilocal expansion if we set a finite left expansion point $\sigma_L = \sqrt{\rho_L} \gtrsim 20$ MeV. We emphasize that the phase diagram was calculated with $N = 4$ which means that the flow of only 5 β -function were solved. Finally, we show in Fig. 7.5 that a clear distinction between first and second-order phase transitions can be made. In the first-order region two distinct minima of the potential are found and following the critical line to higher temperatures we see the maximum between both minima flattening until only one minimum remains.

Eight

Summary and Outlook

In this thesis we have investigated the chiral phase transition of 2+1 flavor QCD beyond mean field approximation. Fluctuations were included via the FRG formalism—more specifically we used the Wetterich equation as a means to interpolate between the known microscopic interactions and the macroscopic phenomena comprised in the QCD phase diagram.

We have derived our truncation from the QCD action where we neglected the pure gauge part. Using standard bosonization techniques we established the scalar and pseudoscalar meson nonet as the effective degrees of freedom of three flavor QCD at low energies. The $U(1)_A$ anomaly was modeled by a 't Hooft interaction which we included in our truncation in a simple bosonized form. The quark mass matrix was rewritten in terms of meson fields which functions as an explicit chiral symmetry breaking term. Finally, we allowed for meson interactions of arbitrary order by introducing a meson potential which we wrote as a function of two independent chiral invariants. The final form of the truncated effective action is reminiscent of an effective model known as the *quark-meson model*. Using the Wetterich equation we have derived the flow of the effective potential in leading potential approximation. Apart from the 2+1 flavor realization of this flow equation we also discussed the 2 flavor limit with broken $U(1)_A$ symmetry.

We then solved the 2+1 flavor flow equation numerically on a two dimensional grid using cubic splines to interpolate the effective potential. This gave the IR effective potential in dependence of temperature and chemical potential from which we were easily able to extract the condensates, meson masses and pressure density. We determined the order of the chiral phase transition by examining the light condensate in the T, μ plane and scanning the effective potential for secondary minima. In order to gauge the effect of anomalous breaking of $U(1)_A$ we performed calculations both with and without the 't Hooft determinant.

In the 2 flavor case we made use of a newly developed method, the *bilocal expansion scheme*. We found that we were able to reliably calculate the 2 flavor phase diagram with only 5 β -functions. We showed that it is possible to clearly differentiate between first and second-order phase transitions which is often problematic using standard Taylor expansions. We also compared the convergence properties of the bilocal expansion to standard, static and co-moving Taylor expansion and concluded that both the bilocal and static Taylor expansion converge already at order $N = 6$. However, we were not able to find convergence with the co-moving Taylor expansion.

We started the discussion of the numerical results at vanishing chemical potential and finite temperature where we observed that the chiral phase transition is a smooth crossover in agreement with lattice QCD findings. We observed that chiral $SU(2)_L \otimes SU(2)_R$ symmetry is effectively restored first and only at very high temperatures is the full chiral $SU(3)_L \otimes SU(3)_R$ symmetry approximately restored. The slow restoration of the strange sector could also be seen in the pseudoscalar and scalar mass spectrum since all mesons degenerate only at very high temperatures. We have further seen that the large experimentally measured mass of the η' meson can be explained by the 't Hooft interaction.

Examining the phase diagram for physical quark masses we have observed that the chiral

phase transition is almost completely driven by 2 flavor dynamics. Strange flavor fluctuations wash out first-order phase transitions. However, we found that this effect is relatively small. We find a CEP at high chemical potential and low temperatures as long as the sigma mass does not exceed a critical mass of $m_{s,c} \sim 560$ MeV. Going beyond the usual study of symmetric quark matter we have evaluated the critical surface in T, μ_l, μ_s space. We have found that the chiral phase transition is mainly sensitive to the light chemical potential until the strange chemical potential exceeds the constituent mass of the strange quark $\mu_s \gtrsim m_s \sim 433$ MeV.

Contrary to our mean field calculation where we found the effect of the 't Hooft term to be small it can not be neglected in the FRG calculation where we observed an enlarged first-order region without the anomaly. This is even more prominent in the limit of massless light quarks: We have found the order of the phase transition at $\mu = 0$ to be entirely dependent on the state of the anomaly. Including the 't Hooft term the chiral phase transition is second-order and without the explicit $U(1)_A$ breaking a first-order transition is found at $\mu = 0$. Since the chiral phase transition in the light chiral limit is effectively governed by 2 flavor dynamics this agrees with arguments made in [27] which predict a first-order phase transition for $N_f = 2$ with $U(1)_A$ symmetry.

Finally, we have discussed the chiral phase transition in dependence of pion and kaon masses including the full chiral limit. For fixed start values at the UV cutoff scale Λ we have found that both the light and strange condensates vanish in the chiral limit. We have argued that this is not physical behavior but rather caused by changing initial conditions at Λ depending on the quark masses. Instead of changing the initial parameters at Λ we have introduced a variable UV cutoff going into the chiral limit and fixed f_π to its value at the physical point which ensured spontaneous symmetry breaking for all quark masses. With this variable cutoff we were able to reach the full chiral limit and we found in agreement with [27] that the phase transition is first-order independent of $U(1)_A$ symmetry.

Examining the order of the phase transition for various pion and kaon masses we found a qualitatively very different behavior depending on the axial anomaly. For a broken $U(1)_A$ symmetry we found a small first-order region around the chiral limit which was confined in the m_K direction by a tricritical point at a kaon mass of $m_{K,\text{tric}} \sim 25$ MeV. We have compared this to mean field type calculations which predict a significantly larger first-order region and concluded that meson fluctuations effectively wash out first-order phase transitions. From the tricritical point upwards the phase transition is second-order along the m_K axis which connects intuitively with the 2 flavor limit. Without the 't Hooft determinant a first-order band follows the m_K axis with a critical pion mass of $m_{\pi,\text{tric}} \sim 25$ MeV. In this case the tricritical point lies in the 2 flavor limit and is effectively determined by the $U(2)_L \otimes U(2)_R$ model.

We have seen that the existence of a tricritical point is determined by the state of $U(1)_A$ symmetry at the critical temperature. Within our model we have taken the strength of the 't Hooft determinant to be temperature independent. Consequently the restoration of $U(1)_A$ symmetry is linked to the slowly vanishing strange condensate. By taking into account the temperature dependence of the axial anomaly a more accurate assessment of $U(1)_A$ symmetry at the chiral phase transition should be possible.

Large qualitative differences between FRG and MFA results have been found. The chiral phase transition in MFA seems to generally favor a first-order transition and the effect of the axial anomaly is less pronounced compared to the FRG calculation. This can be in part explained by fluctuation, however, we want to emphasize that the vacuum energy is neglected in standard mean field approximation. The comparison with FRG results is therefore misleading since qualitatively different results are obtained in extended mean field calculations where the vacuum term is included [23, 62].

The discussion of the chiral critical line within the FRG formulation was restricted to vanishing chemical potential. This is simply due to time constraints and the long run time of calculations on a two dimensional grid. There is no apparent problem with repeating the calculations at finite μ and this should be performed in the future. We also would have liked to make the direct connection to the Columbia plot where some results for the chiral critical line exist from lattice calculations, see e.g. [29]. However, this requires an accurate relation

between m_π , m_K and m_l , m_s , the light and strange quark current masses. This should be the topic of further investigation.

Because we have omitted the pure gauge part in our truncation of the QCD action no statement about the deconfinement transition could be made. It would be of interest to see how the $U(1)_A$ anomaly relates to the deconfinement transition. This might give an indication on how the chiral and deconfinement phase transitions are linked. The omission of gluonic degrees of freedom also became apparent in the pressure density where our calculation predicted a much faster approach to the Stefan-Boltzmann limit compared to recent lattice calculations. The usual way to include gluon interactions is by including the Polyakov loop as an effective gluon potential. This leads to the Polyakov-quark-meson model, see e.g. [21, 24] for a FRG discussion.

It is evident that the truncation used for this work is just the first step in a FRG treatment of 2+1 flavor QCD. Going beyond the leading potential approximation a scale dependent wave function renormalization should be included for quark and meson fields. Furthermore, a scale and field dependent Yukawa interaction has been shown to unfold important new dynamics in 2 flavor calculations [72]. The main goal of FRG investigations is to bridge the gap between microscopic QCD interactions and macroscopic phenomena. In our truncation we start with a partially bosonized effective action where quarks and mesons are the degrees of freedom. This is not in the true spirit of microscopic QCD and should be improved by allowing the shift in effective degrees of freedom to happen naturally. Recent investigations have found that this can be achieved by a technique called dynamical hadronization [16, 18, 55]. Ultimately this allows the direct connection to perturbative QCD and eliminates the need for model parameters present in our truncation.

On the numerical side there is also considerable room for improvement. We have used a two dimensional grid method in order to reliably differentiate between first and second-order as well as crossover transitions. Since the two dimensional grid comes with $\mathcal{O}(N^2)$ scaling in the number of grid points we had to sacrifice accuracy to keep the run-time manageable. Improving the numerical setup would likely allow us to reach smaller IR scales and access smaller temperatures in the high μ region. A promising alternative for the two dimensional grid is the bilocal expansion scheme which we only discussed in one dimension, but should also be applicable in two dimensions.

A

Effective Potential in Mean Field Approximation

Here we briefly outline the derivation of the 2+1 flavor effective potential in mean field approximation. We start with the generating functional at vanishing external sources $\mathbf{J} = 0$

$$Z = \int \prod_a \mathcal{D}\sigma_a \mathcal{D}\pi_a \int \mathcal{D}q \mathcal{D}\bar{q} \exp(-S[q, \bar{q}, \sigma_a, \pi_a]) \quad (\text{A.1})$$

where we identify S with the action defined in Eq. (5.22). In mean field approximation we set all meson fields to their vacuum expectation value so that the path integral over meson fields is lost and the meson potential as a function of the two finite condensates $\bar{\sigma}_l$, $\bar{\sigma}_s$ can be factored out of the path integral

$$Z = \exp[-V_4 \tilde{U}(\bar{\sigma}_l, \bar{\sigma}_s)] \cdot \int \mathcal{D}q \mathcal{D}\bar{q} \exp\left(-\int_x q(\not{D} + \gamma_0 \mu + g(T^0 \bar{\sigma}_0 + T^8 \bar{\sigma}_8))q\right) \equiv Z_m \cdot Z_q. \quad (\text{A.2})$$

The effective potential¹

$$\mathcal{U}(T, \mu_f; \bar{\sigma}_l, \bar{\sigma}_s) = -\frac{\ln Z}{V_4} \quad (\text{A.3})$$

then divides into separate contributions from the meson and quark Lagrangian

$$\mathcal{U}(T, \mu_f; \bar{\sigma}_l, \bar{\sigma}_s) = \tilde{U}(\bar{\sigma}_l, \bar{\sigma}_s) - \frac{\ln Z_q}{V_4}. \quad (\text{A.4})$$

We expand the meson potential in the chiral invariants ρ_1 and ρ_2 up to renormalizable couplings

$$\tilde{U}(\rho_1, \rho_2, \zeta) = m^2 \rho_1 + \lambda_1 \rho_1^2 + \lambda_2 \rho_2 - c_A \zeta - c_l \sigma_l - c_s \sigma_s. \quad (\text{A.5})$$

In MFA we evaluate this at the vacuum expectation value for σ_l and σ_s which is in the nonstrange-strange basis

$$\begin{aligned} \tilde{U}(\bar{\sigma}_l, \bar{\sigma}_s) = \frac{m^2}{2} (\bar{\sigma}_l^2 + \bar{\sigma}_s^2) + \frac{\lambda_1}{4} (\bar{\sigma}_l^2 + \bar{\sigma}_s^2)^2 + \frac{\lambda_2}{8} (\bar{\sigma}_l^4 + 2\bar{\sigma}_s^4) \\ - \frac{c_A}{2\sqrt{2}} \bar{\sigma}_s \bar{\sigma}_l^2 - c_l \bar{\sigma}_l - c_s \bar{\sigma}_s. \end{aligned} \quad (\text{A.6})$$

¹As discussed in Sec. 2.3 it is in this case equivalent to the grand potential density.

Here we have used that the chiral invariants and the 't Hooft term evaluated at the vacuum expectation value yields

$$\bar{\rho}_1 = \frac{1}{2} (\bar{\sigma}_l^2 + \bar{\sigma}_s^2), \quad \bar{\rho}_2 = \frac{1}{8} (\bar{\sigma}_l^4 + 2\bar{\sigma}_s^4), \quad \bar{\zeta} = \frac{\bar{\sigma}_s \bar{\sigma}_l^2}{2\sqrt{2}}. \quad (\text{A.7})$$

The meson potential is independent of T and μ_f which is a result of neglected thermal fluctuations in mean field approximation. However, for the quarks we can perform the path integral explicitly since it is a Gaussian integral over Grassman valued fields. This basically gives the determinant of the exponent and using the relation $\ln \det D = \text{Tr} \ln D$ we evaluate the trace over momentum, color and flavor. After summation over fermionic Matsubara frequencies and dropping constant terms which are independent of β, μ or V we end up with (see [78] for details)

$$\ln Z_q = 2V N_c \sum_{f=u,d,s} \int \frac{d^3 p}{(2\pi)^3} [\beta \omega_f + \ln(1 + e^{-\beta(\omega_f - \mu)}) + \ln(1 + e^{-\beta(\omega_f + \mu)})]. \quad (\text{A.8})$$

This result allows an intuitive interpretation of separate contributions from quark and anti-quarks. The first term in the integrand is the divergent vacuum energy. For our calculations we will simply subtract this divergent constant which is sometimes called *no-sea approximation* or standard MFA. It has been applied to the 2+1 flavor quark meson model in for example in [32] and for the $SU(2)_L \otimes SU(2)_R$ case in [79].

As usual, the physical state is found at the minimum of the effective potential

$$\left. \frac{\partial \mathcal{U}}{\partial \sigma_l} \right|_{\substack{\sigma_l = \bar{\sigma}_l \\ \sigma_s = \bar{\sigma}_s}} = \left. \frac{\partial \mathcal{U}}{\partial \sigma_s} \right|_{\substack{\sigma_l = \bar{\sigma}_l \\ \sigma_s = \bar{\sigma}_s}} = 0 \quad (\text{A.9})$$

and the meson masses are defined by the Hesse matrix of the effective action. The individual expressions are similar in structure to the FRG meson masses, however, derivatives of the running meson potential are substituted with the respective derivatives of Eq. (A.5). Note, that it is important to calculate the derivatives of the full effective potential before substituting the expectation values of the fields. Furthermore, it is necessary to consider second derivatives of the quark effective potential because the quark mass matrix is dependent on the meson fields. We list the individual expressions in appendix B.2. As in the FRG formulation the diagonalization leads to mixing of σ and f_0 as well as η' and η .

B

Meson Mass Matrix

B.1 Meson Masses in FRG

Here we list all non-vanishing entries of the squared mass matrix $M_{k,\varphi}^2$ for the 2+1 flavor system. They are found by differentiating Eq. (5.27) with respect to the meson fields and evaluating the result at the vacuum expectation values. In order to simplify some expressions we introduce a modified chiral invariant $\tilde{\rho}_2 = \rho_2 - \rho_1^2/3$ and write the meson potential as a function of ρ_1 and $\tilde{\rho}_2$. Since we numerically represent the effective potential on a grid in the coordinates x and y we transform the derivatives ∂_{ρ_1} and $\partial_{\tilde{\rho}_2}$ into derivatives ∂_x and ∂_y by applying the chain rule.

We start with the already diagonal entries of $M_{k,\varphi}^2$. For the scalar mesons we have the a_0 and κ meson masses

$$\begin{aligned} m_{a_0}^2 &= \tilde{U}^{(1,0)}(\rho_1, \tilde{\rho}_2) + \frac{1}{6}(7\sigma_l^2 - 2\sigma_s^2) \tilde{U}^{(0,1)}(\rho_1, \tilde{\rho}_2) + \frac{c_A \sigma_s}{\sqrt{2}} \\ &= \frac{2(y-2x)}{y} \tilde{U}^{(1,0)}(x, y) + \frac{2(6x-y)}{y} \tilde{U}^{(0,1)}(x, y) + \frac{1}{2} c_A \sqrt{x+y} \\ m_\kappa^2 &= \tilde{U}^{(1,0)}(\rho_1, \tilde{\rho}_2) + \frac{1}{6}(3\sqrt{2}\sigma_l\sigma_s + \sigma_l^2 + 4\sigma_s^2) \tilde{U}^{(0,1)}(\rho_1, \tilde{\rho}_2) + \frac{c_A \sigma_l}{2} \\ &= -\frac{1}{y} (2\sqrt{x(x+y)} + 2x) \tilde{U}^{(1,0)}(x, y) + \frac{1}{y} (6\sqrt{x(x+y)} + x + 4y) \tilde{U}^{(0,1)}(x, y) + \frac{\sqrt{x} c_A}{2} \quad (\text{B.1}) \end{aligned}$$

where $m_{a_0}^2 = (M_{k,\varphi}^2)_{\sigma_i \sigma_i}$ for $i = 1, 2, 3$ and $m_\kappa^2 = (M_{k,\varphi}^2)_{\sigma_i \sigma_i}$ for $i = 4, \dots, 7$. The masses of the a_0 triplet degenerates due to $SU(2)_V$ symmetry and so do the masses of the two κ doublets. The analogous entries of the pseudoscalar sector are given by

$$\begin{aligned} m_\pi^2 &= \tilde{U}^{(1,0)}(\rho_1, \tilde{\rho}_2) + \frac{1}{6}(\sigma_l^2 - 2\sigma_s^2) \tilde{U}^{(0,1)}(\rho_1, \tilde{\rho}_2) - \frac{c_A \sigma_s}{\sqrt{2}} \\ &= 2\tilde{U}^{(1,0)}(x, y) - 2\tilde{U}^{(0,1)}(x, y) - \frac{1}{2} c_A \sqrt{x+y} \\ m_K^2 &= \tilde{U}^{(1,0)}(\rho_1, \tilde{\rho}_2) + \frac{1}{6}(-3\sqrt{2}\sigma_l\sigma_s + \sigma_l^2 + 4\sigma_s^2) \tilde{U}^{(0,1)}(\rho_1, \tilde{\rho}_2) - \frac{1}{2} c_A \sigma_l \\ &= \frac{2}{y} (3x + 2y - 3\sqrt{x(x+y)}) \left(\tilde{U}^{(0,1)}(x, y) - \frac{1}{3} \tilde{U}^{(1,0)}(x, y) \right) + \frac{4}{3} \tilde{U}^{(1,0)}(x, y) - \frac{1}{2} \sqrt{x} c_A \quad (\text{B.2}) \end{aligned}$$

with $m_\pi^2 = (M_{k,\varphi}^2)_{\pi_i \pi_i}$ for $i = 1, 2, 3$ and $m_K^2 = (M_{k,\varphi}^2)_{\pi_i \pi_i}$ for $i = 4, \dots, 7$. The only non-diagonal entries in the mass matrix are comprised in the $0-8$ or $l-s$ sector. Derivatives with respect to σ_l and σ_s yield

$$\begin{aligned}
m_{\sigma_l \sigma_l}^2 &= 2\tilde{U}^{(1,0)}(x, y) - 2\tilde{U}^{(0,1)}(x, y) + 4x[\tilde{U}^{(2,0)}(x, y) + 2\tilde{U}^{(1,1)}(x, y) + \tilde{U}^{(0,2)}(x, y)] - \frac{1}{2}c_A\sqrt{x+y}, \\
m_{\sigma_l \sigma_s}^2 &= 4\sqrt{2x(x+y)}[\tilde{U}^{(1,1)}(x, y) - \tilde{U}^{(2,0)}(x, y)] - c_A\sqrt{\frac{x}{2}}, \\
m_{\sigma_s \sigma_s}^2 &= 4\tilde{U}^{(0,1)}(x, y) + 8(x+y)\tilde{U}^{(0,2)}(x, y)
\end{aligned} \tag{B.3}$$

where $m_{ij}^2 = (M_{k,\varphi}^2)_{ij}$. There is no overlap between the scalar and pseudoscalar mass matrix, which means that we can already diagonalize this 2×2 submatrix. Introducing the scalar mixing angle ϕ_S we write

$$\begin{aligned}
m_{f_0}^2 &= m_{\sigma_l \sigma_l}^2 \cos^2 \phi_S + m_{\sigma_s \sigma_s}^2 \sin^2 \phi_S - m_{\sigma_l \sigma_s}^2 \sin^2(2\phi_S) \\
m_{\sigma}^2 &= m_{\sigma_l \sigma_l}^2 \sin^2 \phi_S + m_{\sigma_s \sigma_s}^2 \cos^2 \phi_S + m_{\sigma_l \sigma_s}^2 \sin^2(2\phi_S)
\end{aligned} \tag{B.4}$$

which follows from a rotation of the nonstrange-strange sector

$$\begin{aligned}
f_0 &= \sigma_l \cos \phi_S - \sigma_s \sin \phi_S \\
\sigma &= \sigma_l \sin \phi_S + \sigma_s \cos \phi_S.
\end{aligned} \tag{B.5}$$

For $\phi_S = 90^\circ$ we have ideal flavor mixing where $\sigma = \sigma_l$ has no strange component and $f_0 = \sigma_s$ is a pure strange state. We find the following relation for the mixing angle

$$\tan(2\phi_S) = \frac{2m_{\sigma_l \sigma_s}^2}{m_{\sigma_s \sigma_s}^2 - m_{\sigma_l \sigma_l}^2}. \tag{B.6}$$

In the pseudoscalar sector we derive the masses in the 0 – 8 basis

$$\begin{aligned}
m_{\pi_0 \pi_0}^2 &= \tilde{U}^{(1,0)}(\rho_1, \tilde{\rho}_2) + \frac{1}{3}c_A(2\sigma_l + \sqrt{2}\sigma_s) = \frac{4}{3}\tilde{U}^{(1,0)}(x, y) + \frac{1}{3}c_A(\sqrt{x+y} + 2\sqrt{x}), \\
m_{\pi_0 \pi_8}^2 &= \frac{(\sigma_l^2 - 2\sigma_s^2)}{3\sqrt{2}}\tilde{U}^{(0,1)}(\rho_1, \tilde{\rho}_2) + \frac{1}{6}c_A(2\sigma_s - \sqrt{2}\sigma_l) \\
&= \frac{2}{3}\sqrt{2}\tilde{U}^{(1,0)}(x, y) - 2\sqrt{2}\tilde{U}^{(0,1)}(x, y) + \frac{c_A(\sqrt{x+y} - \sqrt{x})}{3\sqrt{2}}, \\
m_{\pi_8 \pi_8}^2 &= \tilde{U}^{(1,0)}(\rho_1, \tilde{\rho}_2) + \frac{1}{6}(2\sigma_s^2 - \sigma_l^2)\tilde{U}^{(0,1)}(\rho_1, \tilde{\rho}_2) + \frac{1}{6}c_A(\sqrt{2}\sigma_s - 4\sigma_l) \\
&= \frac{2}{3}\tilde{U}^{(1,0)}(x, y) + 2\tilde{U}^{(0,1)}(x, y) + \frac{1}{6}c_A(\sqrt{x+y} - 4\sqrt{x})
\end{aligned} \tag{B.7}$$

which can be diagonalized by introducing the pseudoscalar mixing angle θ_P

$$\begin{aligned}
\eta &= \pi_8 \cos \theta_P - \pi_0 \sin \theta_P \\
\eta' &= \pi_8 \sin \theta_P + \pi_0 \cos \theta_P.
\end{aligned} \tag{B.8}$$

We can transform the 0 – 8 basis into the nonstrange-strange basis according to Eq. (5.51) which is a rotation of π_0, π_8 by the constant angle $-\arctan \sqrt{2} \sim -54.74^\circ$. With this the pseudoscalar mixing angle in the nonstrange-strange basis ϕ_P as defined by

$$\begin{aligned}
\eta &= \pi_l \cos \phi_P - \pi_s \sin \phi_P \\
\eta' &= \pi_l \sin \phi_P + \pi_s \cos \phi_P
\end{aligned} \tag{B.9}$$

can be expressed as $\phi_P = \theta_P + \arctan \sqrt{2}$.

B.2 Meson Masses in Mean Field Approximation

In MFA the meson masses are given as derivatives of the expanded meson potential from Eq. (A.5). The derivatives of the with respect to the scalar fields are given by

$$\begin{aligned}
\frac{\partial^2 U}{\partial \sigma_0^2} &= m^2 + \frac{1}{3}c_A \left(-2\sigma_l - \sqrt{2}\sigma_s \right) + \lambda_2 (\sigma_l^2 + \sigma_s^2) + \frac{1}{3}\lambda_1 \left(7\sigma_l^2 + 4\sqrt{2}\sigma_s\sigma_l + 5\sigma_s^2 \right), \\
\frac{\partial^2 U}{\partial \sigma_0 \partial \sigma_8} &= \frac{1}{6}c_A \left(\sqrt{2}\sigma_l - 2\sigma_s \right) + \frac{\lambda_2 (\sigma_l^2 - 2\sigma_s^2)}{\sqrt{2}} + \frac{2}{3}\lambda_1 \left(\sqrt{2}\sigma_l^2 - \sigma_s\sigma_l - \sqrt{2}\sigma_s^2 \right), \\
\frac{\partial^2 U}{\partial \sigma_i^2} &= m^2 + \frac{3}{2}\lambda_2\sigma_l^2 + \frac{c_A\sigma_s}{\sqrt{2}} + \lambda_1 (\sigma_l^2 + \sigma_s^2) \quad \text{for } i = 1, 2, 3 \\
\frac{\partial^2 U}{\partial \sigma_i^2} &= m^2 + \frac{c_A\sigma_l}{2} + \lambda_2 \left(\frac{\sigma_l^2}{2} + \frac{\sigma_s\sigma_l}{\sqrt{2}} + \sigma_s^2 \right) + \lambda_1 (\sigma_l^2 + \sigma_s^2) \quad \text{for } i = 4, \dots, 7 \\
\frac{\partial^2 U}{\partial \sigma_8^2} &= m^2 + \frac{1}{6}c_A \left(4\sigma_l - \sqrt{2}\sigma_s \right) + \frac{1}{2}\lambda_2 (\sigma_l^2 + 4\sigma_s^2) + \frac{1}{3}\lambda_1 \left(5\sigma_l^2 - 4\sqrt{2}\sigma_s\sigma_l + 7\sigma_s^2 \right) \quad (\text{B.10})
\end{aligned}$$

and the derivatives with respect to the pseudo scalar fields

$$\begin{aligned}
\frac{\partial^2 U}{\partial \pi_0^2} &= m^2 + \frac{1}{3}c_A \left(2\sigma_l + \sqrt{2}\sigma_s \right) + \lambda_1 (\sigma_l^2 + \sigma_s^2) + \frac{1}{3}\lambda_2 (\sigma_l^2 + \sigma_s^2), \\
\frac{\partial^2 U}{\partial \pi_0 \partial \pi_8} &= \frac{1}{6}c_A \left(2\sigma_s - \sqrt{2}\sigma_l \right) + \frac{\lambda_2 (\sigma_l^2 - 2\sigma_s^2)}{3\sqrt{2}}, \\
\frac{\partial^2 U}{\partial \pi_i^2} &= m^2 + \frac{1}{2}\lambda_2\sigma_l^2 + \lambda_1 (\sigma_l^2 + \sigma_s^2) - \frac{c_A\sigma_s}{\sqrt{2}} \quad \text{for } i = 1, 2, 3 \\
\frac{\partial^2 U}{\partial \pi_i^2} &= m^2 + \lambda_2 \left(\frac{\sigma_l^2}{2} - \frac{\sigma_s\sigma_l}{\sqrt{2}} + \sigma_s^2 \right) + \lambda_1 (\sigma_l^2 + \sigma_s^2) - \frac{c_A\sigma_l}{2} \quad \text{for } i = 4, \dots, 7 \\
\frac{\partial^2 U}{\partial \pi_8^2} &= m^2 + \frac{1}{6}c_A \left(\sqrt{2}\sigma_s - 4\sigma_l \right) + \lambda_1 (\sigma_l^2 + \sigma_s^2) + \frac{1}{6}\lambda_2 (\sigma_l^2 + 4\sigma_s^2). \quad (\text{B.11})
\end{aligned}$$

In MFA the meson masses receive further corrections from second derivatives of the quark contribution. We have

$$\begin{aligned}
\left. \frac{\partial^2 \Omega_q(T, \mu)}{\partial \phi_{i,a} \partial \phi_{i,b}} \right|_{\text{VEV}} &= \frac{\nu_c}{2} \sum_{f=l,s} \int \frac{d^3 p}{(2\pi)^3} \frac{1}{E_{q,f}} \left[(n_{q,f} + n_{\bar{q},f}) \left(m_{f,ab}^2 - \frac{m_{f,a}^2 m_{f,b}^2}{2E_{q,f}^2} \right) \right. \\
&\quad \left. - (b_{q,f} + b_{\bar{q},f}) \frac{m_{f,a}^2 m_{f,b}^2}{2E_{q,f} T} \right], \quad (\text{B.12})
\end{aligned}$$

where we have abbreviate derivatives of the quark masses $m_{f,a}^2 = \frac{\partial m_f^2}{\partial \phi_a}$, $m_{f,ab}^2 = \frac{\partial^2 m_f^2}{\partial \phi_a \partial \phi_b}$ and introduce the quark function $b_{q,f} = n_{q,f}(1 - n_{q,f})$ with its corresponding antiquark function $b_{\bar{q},f}(T, \mu_f) = b_{q,f}(T, -\mu_f)$.

The quark mass matrix can be worked out to be

$$M_q^2 = g^2 \phi_5 \phi_5^\dagger = g^2 \left[(T^a \sigma_a)^2 + (T^a \pi_a)^2 \right] \quad (\text{B.13})$$

and its derivatives with respect to the meson fields are given by

	$m_{l,a}^2 m_{l,b}^2 / g^4$	$m_{l,ab}^2 / g^2$	$m_{s,a}^2 m_{s,b}^2 / g^4$	$m_{s,ab}^2 / g^2$
$\sigma_0 \sigma_0$	$\frac{1}{3} \sigma_l^2$	$\frac{2}{3}$	$\frac{1}{3} \sigma_s^2$	$\frac{1}{3}$
$\sigma_1 \sigma_1, \dots, \sigma_3 \sigma_3$	$\frac{1}{2} \sigma_l^2$	1	0	0
$\sigma_4 \sigma_4, \dots, \sigma_7 \sigma_7$	$\frac{1}{2\sqrt{2}} \sigma_l \sigma_s$	$\frac{1}{2}$	$\frac{1}{2\sqrt{2}} \sigma_l \sigma_s$	$\frac{1}{2}$
$\sigma_8 \sigma_8$	$\frac{1}{6} \sigma_l^2$	$\frac{1}{3}$	$\frac{2}{3} \sigma_s^2$	$\frac{2}{3}$
$\sigma_0 \sigma_8$	$\frac{\sqrt{2}}{3} \sigma_l^2$	$\frac{\sqrt{2}}{3}$	$-\frac{\sqrt{2}}{3} \sigma_s^2$	$-\frac{\sqrt{2}}{3}$

Table B.1: Vacuum expectation value of the quark mass derivatives in respect to the meson fields. Only derivatives with respect to the scalar mesons σ_a are shown since $m_{f,\pi_a}^2 = 0$ and $m_{f,\pi_a\pi_b}^2 = m_{f,\sigma_a\sigma_b}^2$.

$$\begin{aligned}
\left. \frac{\partial M_q^2}{\partial \sigma_a} \right|_{\text{VEV}} &= 2g^2 (T^0 \sigma_0 + T^8 \sigma_8) T^a, & \left. \frac{\partial M_q^2}{\partial \pi_a} \right|_{\text{VEV}} &= 0, \\
\left. \frac{\partial^2 M_q^2}{\partial \sigma_a \partial \sigma_b} \right|_{\text{VEV}} &= \left. \frac{\partial^2 M_q^2}{\partial \pi_a \partial \pi_b} \right|_{\text{VEV}} = 2g^2 T^a T^b.
\end{aligned} \tag{B.14}$$

The u, d, s quark masses are given by the diagonal elements of the quark mass matrix and so are their respective derivatives. Because we enforce $SU(2)$ isospin symmetry we have $E_{q,u} = E_{q,d}$ so that we only need to integrate over the light- and strange quark contributions separately in Eq. (B.12). We define the sum of up and down mass derivatives as $m_{l,a}^2 m_{l,b}^2 = m_{u,a}^2 m_{u,b}^2 + m_{d,a}^2 m_{d,b}^2$ and $m_{l,ab}^2 = m_{u,ab}^2 + m_{d,ab}^2$ which are tabulated in Tab. B.1.

C

Parameter Fixing

As initial condition we for the flow equation we define the effective potential \mathcal{U} at the cutoff scale Λ . We expanding \mathcal{U} in the chiral invariants ρ_1 and $\tilde{\rho}_2$ up to renormalizable couplings. Subsequently adding the explicit symmetry breaking terms we have

$$\mathcal{U}_\Lambda = a_{10}\rho_1 + \frac{a_{20}}{2}\rho_1^2 + a_{01}\tilde{\rho}_2 - c_A\zeta - c_l\sigma_l - c_s\sigma_s. \quad (\text{C.1})$$

The parameters in the initial potential and the Yukawa coupling g were fitted to several IR values. With the pion and kaon masses ($m_\pi = 138$ MeV, $m_K = 496$ MeV) and the respective decay constants ($f_\pi = 92.4$ MeV, $f_K = 113$ MeV) we analytically evaluate the explicit symmetry breaking parameters using Eq. (6.6). The 't Hooft determinant term is fixed by the combined η' and η masses [32] and we choose $g = 6.5$ which gives constituent quark masses of $m_l = 300$ MeV and $m_s = 433$ MeV. The other free parameters are fixed by f_π , f_K and the sigma mass in the IR. Since the flow equation is a highly non-linear partial differential equation the task of finding suitable start parameters is non-trivial. We use three parameter sets from [23] with $\Lambda = 1$ GeV and find further start parameters using the stochastic minimization algorithm *Differential Evolution* [80]. The structure of the flow equation limits the range of possible IR values. This limits the possible sigma masses to $m_\sigma \in [400, 600]$ MeV which fortunately includes realistic sigma masses.

In the $SU(2)_L \otimes SU(2)_R$ model we have only one chiral invariant $\rho = \sigma^2$ and since $U(1)_A$ is maximally broken a single explicit symmetry breaking parameter remains. The expansion up to marginal couplings reads

$$\mathcal{U}_\Lambda = a_{10}\rho_1 + \frac{a_{20}}{2}\rho_1^2 - c\sigma. \quad (\text{C.2})$$

We fix the three parameters by demanding physical values for f_π , m_π and m_σ in the IR. All parameters used for the 2+1 and 2 flavor FRG calculations are collected in Tab. C.1 and its caption.

Parameters in Mean Field Approximation. In the mean field approximation we do not have to evolve from the UV to the IR which simplifies the parameter fixing. We follow the procedure put forward in [32] and for comparison with FRG results we fitted parameters to the sigma masses $m_\sigma = 400, 480, 560$ MeV. All MFA parameters can be found in Tab. C.2 and its caption.

N_f	Λ [MeV]	a_{10} [MeV ²]	a_{01}	a_{20}	c_A [MeV]	m_σ [MeV]
2+1	1000	$(972.63)^2$	50	2.5	4807.84	400
		$(867.76)^2$	50	12	4807.84	480
		$(542.22)^2$	50	36	4807.84	560
		$(306.60)^2$	140	19.68	0	480
2+1	700	$(562.02)^2$	50.38	26.31	4807.84	490
		$(345.84)^2$	108.70	14.73	0	540
2	900	$(417.99)^2$	-	2.614	-	560

Table C.1: Parameters for the 2 and 2+1 flavor initial potential. First three parameter sets from [23]. The remaining free parameters are $g = 6.5$ and at the physical point $c_l = c = (120.73 \text{ MeV})^3$, $c_s = (336.41 \text{ MeV})^3$.

m^2 [MeV ²]	λ_1	λ_2	c [MeV]	m_σ [MeV]
494.76^2	-5.90	46.48	4807.84	400
448.56^2	-3.40	46.48	4807.84	480
384.71^2	-0.36	46.48	4807.84	560
$-(306.26)^2$	13.49	46.48	4807.84	800
225.23^2	-21.98	82.47	0	480
$-(503.55)^2$	-4.55	82.47	0	800

Table C.2: Parameter sets for the effective potential in mean field approximation. The remaining free parameters are $g = 6.5$ and at the physical point $c_l = c = (120.73 \text{ MeV})^3$, $c_s = (336.41 \text{ MeV})^3$.

D

Determining the Chiral Critical Line

Here we describe some technical aspects that went into calculating the chiral critical line.

An important first realization is that we can add the explicit symmetry breaking terms in the IR because $\partial_t c_l = \partial_t c_s = 0$ and c_l, c_s do not appear in the meson masses since the explicit symmetry breaking terms are linear in the fields. This is not true for the 't Hooft determinant where we also have $\partial_t c_A = 0$ but ζ is cubic in the fields and therefore c_A enters in the meson masses. Because c_l and c_s do not enter in the flow we always calculate the effective potential in the chiral limit and subsequently add the explicit symmetry breaking terms. This drastically reduces the numerical effort for the calculation of the critical line since the potential in chiral limit has to be calculated essentially once which is the computationally expensive step. Retroactively different quark masses can be adjusted by varying the parameters c_l and c_s . This constitutes *tilting* the potential in the σ_l and σ_s direction and subsequently minimizing to extract $\bar{\sigma}_l$ and $\bar{\sigma}_s$. This step is numerically much cheaper compared to solving the flow equation.

What can not be avoided is the calculation of different temperature and chemical potential values. This gives the effective potential in chiral limit as a function of T and μ . Naturally, this can be also extended to unsymmetrical quark matter with independent chemical potential μ_l and μ_s . We then numerically minimize the effective potential for a set value of c_l and c_s which gives the condensates as a function of T and μ

$$\bar{\sigma}_{l,c_l c_s}(T, \mu), \quad \bar{\sigma}_{s,c_l c_s}(T, \mu). \quad (\text{D.1})$$

Each set of c_l and c_s can be attributed to a point in the m_π, m_K plane using Eq. (6.6). We then determine the order of the chiral phase transition from the temperature dependence of the light condensate. A discontinuity in the order parameter $\bar{\sigma}_l$ is the necessary condition for a first-order phase transition with the existence of two minima in the effective potential being a sufficient condition. Distinguishing a first-order from a very steep second-order or crossover transition is at times difficult because numerically only a finite number of T values can be computed. This is especially true right at the chiral critical line.

In our calculations we have computed T values in $\Delta T = 0.5$ MeV steps in the vicinity of the critical temperature. With this relatively fine temperature resolution a clear distinction between first-order and crossover in the vicinity of the chiral critical line was still not possible. In order to complement the finite number of temperature values $\{T_i\}$ we make use of the information encoded in the effective potential: We determine the temperature T_i closest to the critical temperature T_c . Then we examine if the potential exhibits two discrete minima at this temperature. We do this numerically by tilting the potential

$$\tilde{\mathcal{U}}_{c_l c_s}(\alpha, T_i, \mu_j, \sigma_l, \sigma_s) = \mathcal{U}_{c_l c_s}(T_i, \mu_j, \sigma_l, \sigma_s) - \alpha(\sigma_l + \sigma_s) \quad (\text{D.2})$$

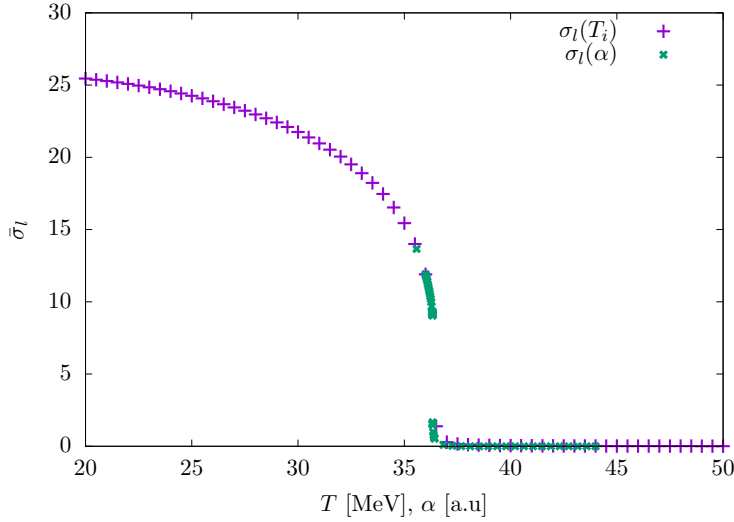


Figure D.1: Light condensate at numerically calculated temperature values and approximate intermediate condensate values near the critical temperature by tilting the effective potential (see text for details).

which upon minimization gives $\bar{\sigma}_{l,c_l c_s}(\alpha, T_i, \mu_j)$ and $\bar{\sigma}_{s,c_l c_s}(\alpha, T_i, \mu_j)$. If two discrete minima exist in the potential the light condensate will be discontinuous as a function of α ¹. This procedure is visualized in Fig. D.1. The light condensate at the computed T_i values are shown and at the point where a jump in the order parameter might occur additional (approximate) condensate values are calculated by tilting the potential. In this case a first-order transition could be clearly identified.

We automate this process in order to calculate the chiral critical line. To this end we have constructed a simple recursive algorithm that terminates if a *sufficiently sharp* peak in $\partial_\alpha \bar{\sigma}_l$ could be found. We use this as a criterion for a first-order phase transition.

As described in Sec. 6.6, we calculate the chiral effective potential for different UV cutoffs to cure the problem of vanishing condensates in the chiral limit. Fixing f_π to its physical value we end up with lines in the m_π, m_K plane corresponding to a single value of Λ . This is visualized in Fig. D.2 where we show the output of the recursive algorithm for different Λ values. This is the underlying data used for the right panel of Fig. 6.17.

¹Assuming that both minima are not on a line perpendicular to the tilt direction. This is never the case in our system.

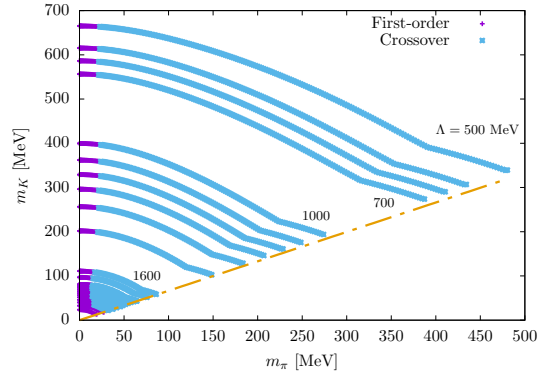


Figure D.2: The order of the chiral phase transition without anomaly in dependence of pion and kaon masses. Each line in the plot corresponds to a different UV cutoff Λ . We have noted several cutoff values inside the plot. The order of the phase transition was determined at each point in the plot using the recursive procedure (see text). At the yellow line $c_s = 0$.

Bibliography

- [1] M. Gell-Mann, Phys. Lett. **8**, 214 (1964).
- [2] G. Zweig, CERN-TH **401** (1964).
- [3] D. Gross, and F. Wilczek, Phys. Rev. **D8**, 3633 (1973).
- [4] H. D. Politzer, Phys. Rev. Lett. **30**, 1346 (1973).
- [5] B. Svetitsky, Phys. Rept. **132** (1986).
- [6] A. Masayuki, and Y. Koichi, Nucl. Phys. **A504**, 668 (1989).
- [7] GSI Helmholtzzentrum für Schwerionenforschung, http://www.gsi.de/uploads/pics/quark-gluon-phasendiagramm_01.png.
- [8] M. Alford, K. Rajagopal, and F. Wilczek, Phys. Lett. **B422**, 247 (1998).
- [9] J. Berges, and K. Rajagopal, Nucl. Phys. **B538**, 215 (1999).
- [10] Y. Aoki, G. Endrodi, Z. Fodor, S. D. Katz, and K. K. Szabo, Nature **443** (2006).
- [11] S. Borsanyi, et al., JHEP **1009**, 073 (2010).
- [12] A. Bazavov, T. Bhattacharya, M. Cheng, C. DeTar, H. Ding, et al., Phys. Rev. **D85**, 054503 (2012).
- [13] C. Bonati, P. de Forcrand, M. D’Elia, O. Philipsen, and F. Sanfilippo, Phys. Rev. **D90** (2014).
- [14] G. Aarts, PoS **Lattice**, 017 (2013).
- [15] D. F. Litim, Nucl. Phys. **B631**, 128 (2002).
- [16] H. Gies, and C. Wetterich, Phys. Rev. **D65**, 065001 (2002).
- [17] J. Braun, J. Phys. **G39**, 033001 (2012).
- [18] F. Rennecke, “The chiral phase transition of qcd”, PhD thesis (Ruperto-Carola University, Heidelberg, 2015).
- [19] B.-J. Schaefer, and J. Wambach, Nucl. Phys. **A757**, 479 (2005).
- [20] J. M. Pawłowski, AIP Conf. Proc. **1343**, 75 (2011).
- [21] B.-J. Schaefer, J. M. Pawłowski, and J. Wambach, Phys. Rev. **D76**, 074023 (2007).
- [22] T. K. Herbst, “Polyakov-loops and the qcd phase structure”, PhD thesis (Karl-Franzens-Universität Graz, 2012).
- [23] M. Mitter, and B.-J. Schaefer, Phys.Rev. **D89**, 054027 (2014).
- [24] T. K. Herbst, M. Mitter, J. M. Pawłowski, B.-J. Schaefer, and R. Stiele, PoS **QCD-TNT-III**, 030 (2014).
- [25] K. Kamikado, and T. Kanazawa, Journal of High Energy Physics **2015**, 1 (2015).
- [26] Y. Jiang, T. Xia, and P. Zhuang, Phys. Rev. **D93**, 074006 (2015).

- [27] R. D. Pisarski, and F. Wilczek, Phys. Rev. **D29**, 338 (1984).
- [28] C. Schmidt, K. Karsch, and E. Laermann, Nucl. Phys. Proc. Suppl. **106**, 423 (2002).
- [29] P. de Forcrand, and O. Philipsen, JHEP **0701**, 077 (2007).
- [30] S. Ejiri, F. Karsch, E. Laermann, C. Miao, S. Mukherjee, P. Petreczky, C. Schmidt, W. Soeldner, and W. Unger, Phys. Rev. **D80** (2009).
- [31] C. Bonati, G. Cossu, M. D’Elia, A. D. Giacomo, and C. Pica, PoS LATTICE **204** (2009).
- [32] B.-J. Schaefer, and M. Wagner, Phys. Rev. **D79**, 014018 (2009).
- [33] J. T. Lenaghan, Phys. Rev. **D63**, 037901 (2001).
- [34] O. Philipsen, and C. Pinke, Phys. Rev. **D93**, 114507 (2016).
- [35] E. Witten, Nucl. Phys. **B156**, 269 (1979).
- [36] G. Veneziano, Nucl. Phys. **B159**, 213 (1979).
- [37] G. ’t Hooft, Phys. Rev. Lett. **37**, 8 (1976).
- [38] H. Reinhardt, and R. Alkofer, Phys. Lett. **B207**, 482 (1988).
- [39] A. A. Osipov, and B. Hiller, Phys. Lett. B **539**, 76 (2002).
- [40] J. M. Pawłowski, Annals Phys. **322**, 2831 (2007).
- [41] K. Olive, et al., Chin. Phys. **C38** (2014).
- [42] S. Weinberg, *The quantum theory of fields*, The Quantum Theory of Fields 3 Volume Hardback Set Bd. 2 (Cambridge University Press, 1995).
- [43] L. Faddeev, and V. Popov, Phys. Lett. **B25**, 29 (1967).
- [44] V. Gribov, Nucl. Phys. **B139**, 1 (1978).
- [45] M. Peskin, and D. Schroeder, *An introduction to quantum field theory*, Advanced book classics (Addison-Wesley Publishing Company, 1995).
- [46] Y. Nambu, and G. Jona-Lasinio, Phys. Rev. **122**, 345 (1961).
- [47] J. Goldstone, Il Nuovo Cimento **19**, 154 (1961).
- [48] J. Goldstone, A. Salam, and S. Weinberg, Phys. Rev. **127**, 965 (1962).
- [49] K. Fujikawa, and H. Suzuki, *Path integrals and quantum anomalies*, International Series of Monographs on Physics (OUP Oxford, 2013).
- [50] B. Hiller, and A. A. Osipov, (2007).
- [51] M. C. Ruivo, P. Costa, C. A. de Sousa, and Yu. L. Kalinovsky, PoS **HEP2005**, 109 (2006).
- [52] C. Wetterich, Phys. Lett. **B301**, 90 (1993).
- [53] D. F. Litim, and J. M. Pawłowski, Phys. Rev. **D 66**, 025030 (2002).
- [54] H. Gies, Lect. Notes Phys. **852**, 287 (2012).
- [55] M. Mitter, J. M. Pawłowski, and N. Strodthoff, Phys. Rev. **D91**, 054035 (2015).
- [56] F. Rennecke, Phys. Rev. **D92**, 076012 (2015).
- [57] J. Jaeckel, “Effective actions for strongly interacting fermionic systems”, PhD thesis (2007).
- [58] J. Braun, L. Fister, J. M. Pawłowski, and F. Rennecke, (2014).
- [59] A. J. Helmboldt, J. M. Pawłowski, and N. Strodthoff, Phys. Rev. **D91**, 054010 (2014).
- [60] J. T. Lenaghan, D. H. Rischke, and J. Schaffner-Bielich, Phys. Rev. **D62**, 085008 (2000).
- [61] M. Heller, and M. Mitter, (2015).
- [62] V. Skokov, B. Friman, E. Nakano, K. Redlich, and B.-J. Schaefer, Phys. Rev. **D82**, 034029 (2010).

- [63] C. S. Fischer, J. Luecker, and C. A. Welzbacher, Nucl. Phys. **A931**, 774 (2014).
- [64] S. Borsanyi, Z. Fodor, C. Hoelbling, S. D. Katz, S. Krieg, and K. K. Szabo, Phys. Lett. **B370**, 99 (2013).
- [65] R. Vertesi, T. Csorgo, and J. Sziklai, Phys. Rev. **C83** (2009).
- [66] T. Csorgo, R. Vertesi, and J. Sziklai, Phys. Rev. Lett. **105** (2009).
- [67] E. Nakano, B. J. Schaefer, B. Stokic, B. Friman, and K. Redlich, Phys. Lett. **B682**, 401 (2009).
- [68] G. Colangelo, and S. Drr, Eur. Phys. J. **C33**, 543 (2004).
- [69] T. Appelquist, R. C. Brower, G. T. Fleming, J. Kiskis, M. F. Lin, et al., Phys. Rev. **D90**, 114502 (2014).
- [70] D. U. Jungnickel, and C. Wetterich, Proceedings "The exact renormalization group", Faro (1998).
- [71] G. Papp, B.-J. Schaefer, H.-J. Pirner, and J. Wambach, Phys. Rev. **D61**, 096002 (2000).
- [72] J. M. Pawłowski, and F. Rennecke, Phys. Rev. **D90**, 076002 (2014).
- [73] J. Adams, J. Berges, S. Bornholdt, F. Freire, N. Tetradis, and C. Wetterich, Mod. Phys. Lett. **A10**, 2367 (1995).
- [74] K. Kamikado, N. Strodthoff, L. von Smekal, and J. Wambach, Phys. Lett. **B718**, 1044 (2013).
- [75] J. Borchardt, and B. Knorr, Phys. Rev. **D94**, 025027 (2016).
- [76] S. Resch, and B.-J. Schaefer, work in progress.
- [77] W. Press, *Numerical recipes 3rd edition: the art of scientific computing* (Cambridge University Press, 2007).
- [78] J. Kapusta, and C. Gale, *Finite-temperature field theory: principles and applications*, Cambridge Monographs on Mathematical Physics (Cambridge University Press, 2006).
- [79] B.-J. Schaefer, and J. Wambach, Phys. Rev. **D75** (2007).
- [80] R. Storn, and K. Price, English, Journal of Global Optimization **11**, 341 (1997).

Acknowledgements

First and foremost I want to thank my adviser PD Dr. Bernd-Jochen Schaefer for guiding me during the course of this thesis. He sparked my interest in this field and topic for which I am very grateful. All the time he spent answering my questions and generally sharing his passion for physics is greatly appreciated.

Furthermore, I want to thank the two talented physicists in my office—Fabian Rennecke and Konstantin Otto—for always providing an enjoyable work environment and being open for discussions in physical but also in non-physical matters. I am particularly grateful for all the RG knowledge that Fabian Rennecke shared during his time in Gießen.

I would like to offer special thanks to Konstantin Otto, Fabian Rennecke and Paul Wallbott for feedback on this thesis.

To Christin Weber and my family I want to express my gratitude for their constant support and encouragement.

Selbstständigkeitserklärung

Hiermit versichere ich, die vorgelegte Thesis selbstständig und ohne unerlaubte fremde Hilfe und nur mit den Hilfen angefertigt zu haben, die ich in der Thesis angegeben habe. Alle Textstellen, die wörtlich oder sinngemäß aus veröffentlichten Schriften entnommen sind, und alle Angaben die auf mündlichen Auskünften beruhen, sind als solche kenntlich gemacht. Bei den von mir durchgeführten und in der Thesis erwähnten Untersuchungen habe ich die Grundsätze guter wissenschaftlicher Praxis, wie sie in der *Satzung der JustusLiebig-Universität zur Sicherung guter wissenschaftlicher Praxis* niedergelegt sind, eingehalten. Gemäß § 25 Abs. 6 der Allgemeinen Bestimmungen für modularisierte Studiengänge dulde ich eine Überprüfung der Thesis mittels Anti-Plagiatssoftware.

Ort, Datum

Unterschrift